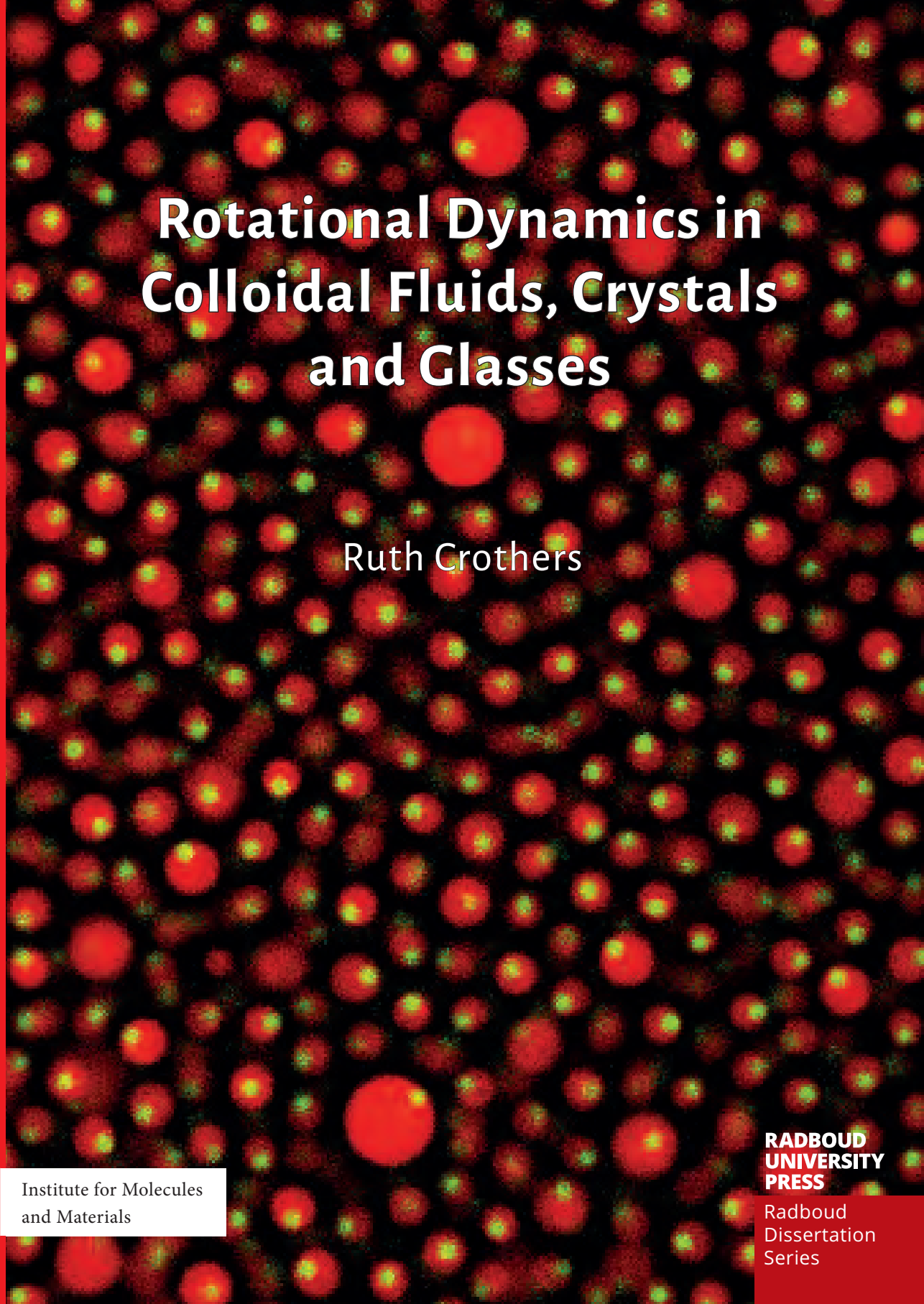

Rotational Dynamics in Colloidal Fluids, Crystals and Glasses

Ruth Crothers

Institute for Molecules and Materials

RADBOUD UNIVERSITY PRESS

Radboud Dissertation Series

Rotational Dynamics in Colloidal Fluids, Crystals and Glasses

Ruth Anne Crothers

Rotational Dynamics in Colloidal Fluids, Crystals and Glasses
Ruth Anne Crothers

Radboud Dissertation Series
ISSN: 2950-2772 (Online); 2950-2780 (Print)

Published by RADBOUD UNIVERSITY PRESS
Postbus 9100, 6500 HA Nijmegen, The Netherlands
www.radbouduniversitypress.nl

Design: Ruth Crothers
Cover: Ruth Crothers
Printing: DPN Rikken/Pumbo

ISBN: 9789465151540
DOI: 10.54195/9789465151540
Free download at: https://doi.org/10.54195/9789465151540

RADBOUD
UNIVERSITY
PRESS

Rotational Dynamics in Colloidal Fluids, Crystals and Glasses

Proefschrift ter verkrijging van de graad van doctor

aan de Radboud Universteit Nijmegen

op gezag van de rector magnificus prof. dr. J.M. Sanders,

volgens besluit van het college voor promoties

in het openbaar te verdedigen op

dinsdag 14 oktober 2025

om 12:30 uur precies

door

Ruth Anne Crothers

geboren op 26 juni 1998

te Dundonald, Northern Ireland

Promotor:	Prof. dr. R.P.A. Dullens
Copromotor:	Dr. B. van der Meer (Wageningen University & Research)
Manuscriptcommissie:	Prof. dr. W.T.S. Huck Prof. dr. A. van Blaaderen (Universiteit Utrecht) Prof. dr. A. Zumbusch (Universität Konstanz, Duitsland)

Contents

Chapter 1

Introduction

The subject of this thesis, rotational dynamics, and this author's homeland, Northern Ireland, have a striking similarity; they are both often overlooked but when considered become incredibly complex. In the case of rotational dynamics this can be simply attributed to the fact that they are harder to observe than translational dynamics. Even under a rudimentary microscope Robert Brown was able to observe the chaotic translational motion of pollen grains [1]. The explanation for his observation was provided by Einstein in 1905 who explained that this so called 'Brownian motion' was the result of the constant bombardment of a particle surface by the molecules of the solvent [2]. The hypothesis that atoms and molecules existed was, at the time, controversial and unconfirmed. However, Einstein's theories were later confirmed by the experiments of Jean Perrin who studied the translational motion and barometric height profile of resin microspheres, providing the first experimental verification that atoms and molecules existed [3, 4]. The subsequent study of translational thermal motion has had a major impact across many fields from granular materials to biological systems [5]. However, less well known is that a simultaneous observation was made by Brown, that in "a few instances the particle was seen to turn on its longer axis" [6]. In other words, the first observation of *translational* thermal motion coincided with the first observation of *rotational* thermal motion. Both Perrin and his son Francis tried to study the rotational dynamics of colloidal particles using both spherical and anisotropic particles, respectively [3, 7, 8]. However, finding isotropic colloidal particles where rotations of *every* particle can be observed is still an experimental challenge.

1.1 Colloidal Model Systems

Colloids have long provided an experimental system where translational thermal motion can be studied, as demonstrated by Perrin [3, 7, 8]. A colloid consists of a particle with at least one dimension between a few nanometers and a few micrometers dispersed in a solvent [1]. Colloids are commonly found in nature, in opals, milk and even our blood as well as in industry in creams, gels and paints, as demonstrated in Fig 1.1. Colloids of well defined shape and size can also be produced in a laboratory [9–11]. The surface of a colloidal particle is constantly bombarded by the molecules of the solvent resulting in the thermal motion Brown first observed. Colloidal particles are a useful model system for several key reasons. Firstly, by tuning their concentration they exhibit analogous phase behaviour to atoms and molecules. This was first predicted by theory and simulations in the 1940s and 50s [12–14], but in the late 1980s it was also experimentally demonstrated in a set of beautiful experiments by Pusey and Van Megen [15]. Using just ten vials of different concentrations of poly(methyl methacrylate) (PMMA) particles they were able to create the entire phase diagram for hard spheres, from the fluid to the crystal and into the glass.

Early studies of the structure and dynamics of colloidal suspensions utilised light scattering techniques such as Dynamic Light Scattering (DLS) or Static Light Scattering (SLS). These techniques were used to study both the structure [16] and nucleation and growth of colloidal crystals [17–19] and the dynamics in a colloidal glass [20–22]. However, light scattering techniques only give access to the ensemble averaged dynamics or structure. A second major advantage of colloidal model systems is that their typical length and timescales allow them to be studied by direct observation using an optical microscope [23]. The development of the confocal microscope, alongside advances in particle synthesis [24, 25], allowed for colloidal particles to be directly observed in 3D [26]. However, these microscopic techniques would not be nearly as powerful without the development of particle tracking routines, in 2D first and later 3D, which allowed the real-space coordinates to be recorded from a single image [27]. This has lead to the direct measurement of dynamics during melting [28, 29], direct observation of dynamic heterogeneities in the colloidal glass phase [30, 31] and the in-situ study of nucleation and growth of colloidal crystals [32–34].

Finally, the colloidal model system is made even more powerful due to the fact that the physical properties of particles such as size, shape and interaction potential can be easily tuned. Particle synthesis techniques have advanced to produce particles of

complex shape, from rods [35–37], to dumbells [38, 39] to particle of complementary shape [40], with tailored interactions, such as particles coated with complementary DNA strands to patchy colloids with anisotropic interactions [41–43], and from a range of building blocks [10, 24, 25]. In summary colloidal suspensions can be used as a highly tuneable and easily imaged particle system that can exhibit a wide variety of phase behaviour including crystals [17–19, 34] and glasses [20–22, 26, 30, 31], to the more exotic liquid crystal [44–47] and quasicrystal phases [48, 49].

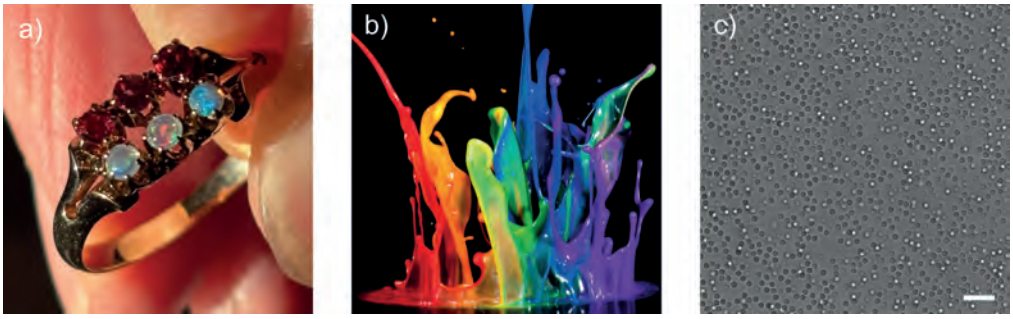

Figure 1.1: a) Photograph of ring inset with opals. Bragg diffraction from crystal lattice of silica nanoparticles is visible. b) Photograph of paint droplet which is a major industrial use of colloids. c) Brightfield microscope image of colloidal particles dispersed in water. Scale bar is equal to $10\mu m$

1.2 Rotational Motion of Colloidal Particles

For the most common colloidal system, typically spherical particles, particle tracking routines allow the extraction of each particle position in x, y and z as a function of time from optical microscopy [27]. This yields vital insight into both the translational dynamics and structure of colloidal suspensions [28–31]. Analysis of the rotational dynamics requires the extraction of the orientation of a particle which, counterintuitively for more complex colloidal systems such as rods, or dumbbells is relatively simple to define, but for a simpler system of spherical particles this proves much more complex.

Many techniques have evolved to overcome this barrier. DLS, where the scattering of an incident light source is tied to the ensemble averaged dynamics of a suspension, has been used to study the rotational dynamics of anisotropic particles [50] as well as the rotational dynamics of isotropic particles that are optically anisotropic [51]. A study of the rotational dynamics of microspheres with a partially crystalline internal structure, which allows the rotational dynamics to be resolved from DLS, shows a surprising

increase in the rotational mobility within the crystal compared to the dense fluid [51]. However, the limitation of light scattering techniques is that they yield only ensemble averaged dynamics, so whether this increase is due to a sub-population of rotationally fast particles or is replicated by every particle in the system is unknown.

Optical microscopy has also been used in the study of rotational dynamics to gather statistics at the *single-particle* level. However, extracting the particle orientations, and therefore rotational dynamics, at the single-particle level for spherical particles still proves a challenge. To overcome this, tracer particles were developed where a particle is altered in shape, size or optical properties that allows its rotational dynamics to be observable. Notable examples include Janus or MOON particles [52], a microsphere half coated in metal, spherical particles with two cores [53, 54] and clusters of spherical particles that form an anisotropic shape [55]. Therefore, most experimental studies focus on single-particle behaviour of a single tracer suspended in a sea of spherical host particles. Studies of isotropic tracer particles show little change in rotational dynamics with increasing packing fraction in either a crystalline [53] or glassy systems [52, 54]. Rotational dynamics of tracer particles are only restricted for tracer particles of anisotropic shape, [55]. Yet, even here the dynamics appear to be Gaussian at both dilute and concentrated packing fractions. In short, it appears rotational dynamics deviate little from diffusive behaviour in any phase except when the tracer particle is sterically entangled.

However, the full story of rotational dynamics in colloidal fluids, crystals and glasses has yet to be revealed. Key questions remain such as, do the dynamics of *all particles* remain diffusive in every phase or is there any coupling between the rotational and translational dynamics of *all particles* or in a polydisperse suspension are the dynamics of *all particles* the same or is there a correlation with size? To answer these questions the dynamics of all particles must be considered.

1.3 Scope of Thesis

In this thesis we address key questions about the rotational dynamics of colloidal particles at the single-particle level for *every* particle in the system. We achieve this by utilising the recently developed 'Off-Centre Under Laser Illumination' (OCULI) particle [56]. This particle consists of small microsphere, referred to as the 'eye', embedded off-centre within a larger microsphere, referred to as the 'body'. Simultaneous

imaging but independent tracking of the body and the eye yield both the particle position and the particle orientation for *every* particle in a population [56]. We use this to address key points of interest including the heterogeneity of rotational dynamics in dense suspensions, the coupling between rotational and translational dynamics in the colloidal fluid, crystal and glass phase as well as the particle-size dependent translational and rotational dynamics in polydisperse particle systems.

In **Chapter 2** we introduce the theoretical background and experimental methods used in the thesis. First we discuss the properties of colloidal particles which make them a model system for the phase behaviour of atoms and molecules. We then derive typical rotational and translational timescales and discuss the interaction potential between colloidal particles and phase behaviour of colloidal suspensions. Following this, we describe the experimental methods used in this work, namely the mechanism of particle synthesis and the microscopy set-up used. Finally, we discuss the image analysis and particle tracking routines used.

Chapter 3 demonstrates an optimised synthesis pathway for 3-trimethoxysilyl propyl methacrylate (TPM) colloidal suspensions to be used for three-dimensional confocal microscopy. We revisit a 'zero-flow' synthesis pathway where TPM microspheres are synthesised from pre-hydrolysed TPM oil. Additionally, we present a new dying method that results in uniform labelling of TPM droplets with a flourescent dye. Finally, we introduce a unique ternary solvent mixture of tetralin, trichloroethylene and tetrachloroethylene, which allows independent control of both the refractive index and density match between particle and solvent.

Rotational dynamics of dense, amorphous colloidal phases are examined in **Chapter 4**. We study a poorly density matched sedimentation-diffusion equilibrium, which results in a dense amorphous sediment, to observe both translational and rotational dynamics at high volume fractions. We uncover that both translational and rotational dynamics are heterogenous in dense suspensions but in opposite ways: while translational dynamics develop a fast subpopulation, rotational dynamics develop a slow subpopulation. We furthermore demonstrate that the rotationally slow particles exist in small 'string-like' clusters where the degree of rotational arrest can be correlated with a compression of the coordination shell in the direction of gravity.

Chapter 5 deals with the coupling between translational and rotational dynamics

in the colloidal fluid, crystal and glass phases. First we observe the decoupling of the ensemble averaged translational and rotational diffusion coefficients in dense liquid phases but reveal a correlation in the single-particle mean-squared displacement, MSD, and mean squared angular displacement, MSAD, at short τ. This correlation is lost once the ensemble averaged MSD becomes diffusive. We find this correlation between the single-particle MSDs and MSADs at short τ extends into the crystal phase and glass phase. However, in the glass phase we find that this correlation changes, becoming less linear, due to the impact of interparticle friction. We finally quantify these observations by examining the correlation coefficient in the fluid, liquid and glass phase.

In **Chapter 6** we demonstrate a simple yet powerful synthesis that allows the production of TPM particles of controlled polydispersity. This is achieved by fractional stirring during the growth phase, which can be used to systematically vary the polydispersity from 5% to 30% to within an error of 6%. We use this method to develop two particle systems from both of which we demonstrate how to extract individual particle size from a single confocal image. First, we create controllably polydisperse OCULI particles which allows the direct observation of both the translational and rotational dynamics of every particle within the system. Using this system we characterise the dynamics across the glass transition as a function of individual particle-size. Secondly, we develop a particle system of polydisperse fluorescent TPM particles with a non-fluorescent shell that allows for the observation of the translational dynamics, but at much larger polydispersities of up to 19%. Using this particle system we show how extreme polydispersity impacts the dynamics across the glass transition.

Finally, we provide a brief summary of the content of this work and outlook on future possibilities in **Chapter 7**.

1.4 Bibliography

[1] A. P. Philipse. *Brownian motion.* Undergraduate Lecture Notes in Physics. Springer International Publisher, Cham, 2018.

[2] A. Einstein. On the theory of the brownian movement. *Ann. Phys*, 19(4):371–381, 1906.

[3] J. Perrin. Mouvement brownien et réalité moléculaire. *Ann. Chim. Phys.*, 19(8):5–104, 1909.

[4] R. Newburgh, J. Peidle, and W. Rueckner. Einstein, perrin, and the reality of atoms: 1905 revisited. *Am. J. Phys*, 74(6):478–481, 2006.

[5] P. Hänggi and F. Marchesoni. Introduction: 100 years of brownian motion. *Chaos*, 15(2):026101, 2005.

[6] G. H. Koenderink. *Rotational and translational diffusion in colloidal mixtures.* PhD thesis, University of Utretcht, 2003.

[7] F. Perrin. Brownian motion of an ellipsoid. i. dielectric dispersion for ellipsoidal molecules. *J. Phys. Radium*, 5(10):497–511, 1934.

[8] F. Perrin. Mouvement brownien d'un ellipsoide (ii). rotation libre et dépolarisation des fluorescences. translation et diffusion de molécules ellipsoidales. *J. Phys. Radium*, 7(1):1–11, 1936.

[9] S. Sacanna and D. J. Pine. Shape-anisotropic colloids: Building blocks for complex assemblies. *Curr. Opin. Colloid Interface Sci.*, 16(2):96–105, 2011.

[10] M. Kamp, S. Sacanna, and R. P. A. Dullens. Spearheading a new era in complex colloid synthesis with tpm and other silanes. *Nat. Rev. Chem.*, 8(6):433–453, 2024.

[11] T. Hueckel, G. M. Hocky, and S. Sacanna. Total synthesis of colloidal matter. *Nat. Rev. Mater.*, 6(11):1053–1069, 2021.

[12] J. G. Kirkwood and E. Monroe. Statistical mechanics of fusion. *J. Chem. Phys.*, 9(7):514–526, 1941.

[13] B. J. Alder and T. E. Wainwright. Phase transition for a hard sphere system. *J. Chem. Phys.*, 27(5):1208, 1957.

[14] W. W. Wood and J. D. Jacobson. Preliminary results from a recalculation of the monte carlo equation of state of hard spheres. *J. Chem. Phys.*, 27(5):1207–1208, 1957.

[15] P. N. Pusey and W. van Megen. Phase behaviour of concentrated suspensions of nearly hard colloidal spheres. *Nature*, 320(6060):340–342, 1986.

[16] P. N. Pusey, W. van Megen, P. Bartlett, B. J. Ackerson, J. G. Rarity, and S. M. Underwood. Structure of crystals of hard colloidal spheres. *Phys. Rev. Lett.*, 63(25):2753, 1989.

[17] K. Schätzel and B. J. Ackerson. Observation of density fluctuations. *Phys. Rev. Lett.*, 68(3):337, 1992.

[18] K. Schätzel and B. J. Ackerson. Crystallization of hard sphere colloids. *Phys. Scr.*, 1993(T49A):70, 1993.

[19] J. L. Harland, S. I. Henderson, S. M. Underwood, and W. van Megen. Observation of accelerated nucleation in dense colloidal fluids of hard sphere particles. *Phys. Rev. Lett.*, 75:3572–3575, 1995.

[20] W. van Megen and S. M. Underwood. Dynamic-light-scattering study of glasses of hard colloidal spheres. *Phys. Rev. E*, 47:248–261, 1993.

[21] S. R. Williams and W. van Megen. Motions in binary mixtures of hard colloidal spheres: Melting of the glass. *Phys. Rev. E*, 64(4):041502, 2001.

[22] W. van Megen, T. C. Mortensen, S. R. Williams, and J. Müller. Measurement of the self-intermediate scattering function of suspensions of hard spherical particles near the glass transition. *Phys. Rev. E*, 58:6073–6085, 1998.

[23] W. C. K. Poon. Colloids as big atoms. *Science*, 304(5672):830–831, 2004.

[24] A. van Blaaderen and A. Vrij. Synthesis and characterization of colloidal

dispersions of fluorescent, monodisperse silica spheres. *Langmuir*, 8(12):2921–2931, 1992.

[25] R. P. A. Dullens, M. Claesson, D. Derks, A. van Blaaderen, and W. K. Kegel. Monodisperse core- shell poly (methyl methacrylate) latex colloids. *Langmuir*, 19(15):5963–5966, 2003.

[26] A. van Blaaderen and P. Wiltzius. Real-space structure of colloidal hard-sphere glasses. *Science*, 270(5239):1177–1179, 1995.

[27] J. C. Crocker and D. G. Grier. Methods of digital video microscopy for colloidal studies. *J. Colloid Interface Sci.*, 179(1):298–310, 1996.

[28] A. L. Thorneywork, J. L. Abbott, D. G. A. L. Aarts, and R. P. A. Dullens. Two-dimensional melting of colloidal hard spheres. *Phys. Rev. Lett.*, 118(15):158001, 2017.

[29] A. M. Alsayed, M. F. Islam, J. Zhang, P. J. Collings, and A. G. Yodh. Premelting at defects within bulk colloidal crystals. *Science*, 309(5738):1207–1210, 2005.

[30] E. R Weeks, J. C. Crocker, A. C. Levitt, A. Schofield, and D. A. Weitz. Three-dimensional direct imaging of structural relaxation near the colloidal glass transition. *Science*, 287(5453):627–631, 2000.

[31] W. K. Kegel and A. van Blaaderen. Direct observation of dynamical heterogeneities in colloidal hard-sphere suspensions. *Science*, 287(5451):290–293, 2000.

[32] N. Wood, J. Russo, F. Turci, and C. P. Royall. Coupling of sedimentation and liquid structure: Influence on hard sphere nucleation. *J. Chem. Phys.*, 149(20), 2018.

[33] F. Ziese, G. Maret, and U. Gasser. Heterogeneous nucleation and crystal growth on curved surfaces observed by real-space imaging. *J. Phys. Condens. Matter*, 25(37):375105, 2013.

[34] U. Gasser, E. R. Weeks, A. Schofield, P. N. Pusey, and D. A. Weitz. Real-space imaging of nucleation and growth in colloidal crystallization. *Science*,

292(5515):258–262, 2001.

[35] A. Kuijk, A. Van Blaaderen, and A. Imhof. Synthesis of monodisperse, rodlike silica colloids with tunable aspect ratio. *J. Am. Chem. Soc.*, 133(8):2346–2349, 2011.

[36] C. M. van Kats, P. M. Johnson, J. E. A. M. van den Meerakker, and A. van Blaaderen. Synthesis of monodisperse high-aspect-ratio colloidal silicon and silica rods. *Langmuir*, 20(25):11201–11207, 2004.

[37] C. Fernández-Rico, T. Yanagishima, A. Curran, D. G. A. L. Aarts, and R. P. A. Dullens. Synthesis of colloidal su-8 polymer rods using sonication. *Adv. Mater.*, 31(17):1807514, 2019.

[38] P. M. Johnson, C. M. van Kats, and A. van Blaaderen. Synthesis of colloidal silica dumbbells. *Langmuir*, 21(24):11510–11517, 2005.

[39] M. Kamp, B. de Nijs, J. J. Baumberg, and O. A. Scherman. Contact angle as a powerful tool in anisotropic colloid synthesis. *J. Colloid Interface Sci.*, 581:417–426, 2021.

[40] S. Sacanna, W. T. M. Irvine, P. M. Chaikin, and D. J. Pine. Lock and key colloids. *Nature*, 464(7288):575–578, 2010.

[41] N. Geerts and E. Eiser. Dna-functionalized colloids: Physical properties and applications. *Soft Matter*, 6(19):4647–4660, 2010.

[42] G. Yi, D. J. Pine, and S. Sacanna. Recent progress on patchy colloids and their self-assembly. *J. Phys. Condens. Matter*, 25(19):193101, 2013.

[43] E. Bianchi, R. Blaak, and C. N. Likos. Patchy colloids: state of the art and perspectives. *Phys. Chem. Chem. Phys.*, 13(14):6397–6410, 2011.

[44] M. P. B. van Bruggen, F. M. van der Kooij, and H. N. W. Lekkerkerker. Liquid crystal phase transitions in dispersions of rod-like colloidal particles. *J. Phys. Condens. Matter*, 8(47):9451, 1996.

[45] A. Kuijk, D. V. Byelov, A. V. Petukhov, A. van Blaaderen, and A. Imhof. Phase behavior of colloidal silica rods. *Faraday Discuss.*, 159(1):181–199, 2012.

[46] R. Kotni, A. Grau-Carbonell, M. Chiappini, M. Dijkstra, and A. van Blaaderen. Splay-bend nematic phases of bent colloidal silica rods induced by polydispersity. *Nat. Commun.*, 13(1):7264, 2022.

[47] C. Fernández-Rico, M. Chiappini, T. Yanagishima, H. de Sousa, D. G. A. L. Aarts, M. Dijkstra, and R. P. A. Dullens. Shaping colloidal bananas to reveal biaxial, splay-bend nematic, and smectic phases. *Science*, 369(6506):950–955, 2020.

[48] Y. Roichman and D. G. Grier. Holographic assembly of quasicrystalline photonic heterostructures. *Opt. Express*, 13(14):5434–5439, 2005.

[49] Y. Gao, B. Sprinkle, D. W. M. Marr, and N. Wu. Direct observation of colloidal quasicrystallization. *Nat. Phys.*, pages 1–8, 2025.

[50] H. Matsuoka, H. Morikawa, and H. Yamaoka. Rotational diffusion of ellipsoidal latex particles in dispersion as studied by depolarized dynamic light scattering. *Colloids Surf. A: Physicochem. Eng. Asp.*, 109:137–145, 1996.

[51] V. Degiorgio, R. Piazza, and R. B. Jones. Rotational diffusion in concentrated colloidal dispersions of hard spheres. *Phys. Rev. E*, 52:2707–2717, 1995.

[52] M. Kim, S. M. Anthony, S. C. Bae, and S. Granick. Colloidal rotation near the colloidal glass transition. *J. Chem. Phys.*, 135(5), 2011.

[53] S. Schütter, A. Roller, J. Kick, J-M. Meijer, and A. Zumbusch. Real-space imaging of translational and rotational dynamics of hard spheres from the fluid to the crystal. *Soft Matter*, 13(44):8240–8249, 2017.

[54] J. Geiger, N. Grimm, M. Fuchs, and A. Zumbusch. Decoupling of rotation and translation at the colloidal glass transition. *J. Chem. Phys.*, 161(1):014507, 2024.

[55] K. V. Edmond, M. T. Elsesser, G. L. Hunter, D. J. Pine, and E. R. Weeks. Decoupling of rotational and translational diffusion in supercooled colloidal fluids. *Proc. Natl. Acad. Sci. U.S.A*, 109(44):17891–17896, 2012.

[56] T. Yanagishima, Y. Liu, H. Tanaka, and R. P. A. Dullens. Particle-level visualization of hydrodynamic and frictional couplings in dense suspensions of spherical colloids. *Phys. Rev. X*, 11:021056, 2021.

Chapter 2

Background and Experimental Methods

In this chapter we describe the attributes of colloidal particles that make them a useful model system for the phase behaviour of atoms and molecules as well as the experimental methods used in this work. First, we describe the dynamics of colloidal particles and derive the time dependence and typical timescales of translational and rotational dynamics. We also discuss the phase behaviour and interaction potential of colloidal particles and how both of these can be controlled in an experimental system. Finally, we discuss the specifics of the experimental system used in this work, namely the mechanism of colloidal particle synthesis, imaging set-up and particle tracking procedures.

2.1 Colloidal Model Systems

For over a century colloids have been used to help us understand and engineer the world around us. A colloid is a suspension of particles, with at least one dimension between 10 nm and several micrometers, dispersed in a solvent [1]. Colloids occur naturally, for example, the characteristic Bragg diffraction observable in opals is caused by silica microspheres [2]. Perhaps more importantly, colloidal particles can be synthesised in a laboratory in a range of shapes and sizes [3–5]. As we will now discuss the typical length, (μm), and timescales, (s) of colloidal particles allow them to be used as a model system for the phase behaviour of atoms and molecules that can be directly observed using a simple optical microscope.

2.1.1 Translational Dynamics of Colloidal Particles

In June 1827, botanist Robert Brown was studying the pollen grains of *Clarkia Pulchella* through his rudimentary microscope [1]. Brown observed tiny organelles, that had escaped from these grains, exhibiting a chaotic, zig-zag motion through the water they were suspended in, despite no obvious mode of propulsion. Furthermore, this motion could be replicated by particles from an inorganic source if it was ground to small enough sizes, even from a sample of stone from the Sphinx [1]. This was the first observation of the predictably named Brownian motion, but the explanation for why it took place sparked much discussion from the scientific community. In 1905 Einstein was working to verify the, at the time controversial, hypothesis that atoms and molecules of definite size existed. He theorised that the laws derived from kinetic theory for atoms and molecules also applied to a much larger colloidal particle suspended in solution, albeit at different length and timescales [6]. In 1909, Jean Perrin verified Einsteins theories experimentally by measuring the barometric height profile of a colloidal suspension [7]. While initially derived for atoms, where the decay length is over several km, for a colloidal suspension the length scales are shortened to several μm, hence easily measurable using an optical microscope. This work earned a Nobel Prize for Perrin in 1926 and paved the way for the use of colloids as 'big atoms' based on the fact that colloids display the same phase behaviour as atoms and molecules but at length and timescales that are observable on an optical microscope [8]. We will now discuss this by deriving the characteristic translational timescales for a typical colloidal particle. The following derivation is largely reproduced from Ref [1].

For a colloidal particle suspended in a solvent, the surface is constantly bombarded

by solvent molecules undergoing thermal motion. Therefore, the colloidal particle experiences a constantly fluctuating force as a sum of these collisions, which results in is the same chaotic, zig-zag motion Brown first observed. Consider a colloidal particle undergoing Brownian motion in 1D, where the displacement, x, can either be $+ve$ or $-ve$. Over time, the mean of the individual displacements will become zero as either direction is equally probable. Therefore,

$$\langle x \rangle = \int_{-\infty}^{+\infty} P(x,t) x dx = 0, \tag{2.1}$$

where $P(x,t)$ is the probability density of finding a particle which has a displacement of x. Therefore, to evaluate the translational dynamics we examine the mean-squared displacement, (MSD) which is defined as,

$$\langle x^2 \rangle = \int_{-\infty}^{+\infty} P(x,t) x^2 dx > 0. \tag{2.2}$$

As we are aiming to derive how this quantity varies with time we differentiate to obtain,

$$\frac{d}{dt}\langle x^2 \rangle = \int_{-\infty}^{+\infty} \frac{\partial}{\partial t} P(x,t) x^2 dx. \tag{2.3}$$

We can simplify Eq 2.3 by first considering that the particle concentration, $\rho(r,t)$ is directly proportional to the probability of finding a particle at that location,

$$P(x,t) \propto \rho(x,t). \tag{2.4}$$

Furthermore for a species diffusing in the x direction the following diffusion equation holds,

$$\frac{\partial}{\partial t}\rho(x,t) = D\frac{\partial^2}{\partial x^2}\rho(x,t), \tag{2.5}$$

where D is the diffusion coefficient. Combining Eq 2.3, 2.4 and 2.5 gives,

$$\frac{\partial}{\partial t}P(x,t) = D\frac{\partial^2}{\partial x^2}P(r,t). \tag{2.6}$$

Substituting this into Eq 2.3 yields:

$$\frac{d}{dt}\langle x^2\rangle = \int_{-\infty}^{+\infty}\frac{\partial}{\partial t}P(x,t)x^2dx = D\int_{-\infty}^{+\infty}\left[\frac{\partial^2}{\partial x^2}P(x,t)\right]x^2dx. \tag{2.7}$$

We can evaluate the integral by integrating by parts to give,

$$D\int_{-\infty}^{+\infty}\left[\frac{\partial^2}{\partial x^2}P(x,t)\right]x^2dx = D\left[\frac{\partial}{\partial x}P(x,t)x^2\right]_{-\infty}^{+\infty} - D\int_{-\infty}^{+\infty}\frac{\partial}{\partial x}P(x,t)2xdx. \tag{2.8}$$

As $P(\pm\infty,t)$ is a probability distribution with a shape that can be described as a bell-shaped curve we can state that $P(\pm\infty,t)$, as well as the first and second derivative, vanish as $x \to \pm\infty$. Therefore, the first term on the right hand side is zero. The remaining integral on the right hand side can be evaluated by integrating by parts again to give,

$$D\int_{-\infty}^{+\infty}\frac{\partial}{\partial x}P(x,t)2xdx = D\left[P(x,t)2x\right]_{-\infty}^{+\infty} - 2D\int_{-\infty}^{+\infty}P(x,t)dx. \tag{2.9}$$

As $P(x,t)$ is symmetric the first term on the right hand side is again zero. The remaining integral simplifies to give,

$$\frac{d}{dt}\langle x^2\rangle = 2D. \tag{2.10}$$

The above derivation for x can also be carried out for, y and z so we can include the dimensionality, n,

$$\frac{d}{dt}\langle r^2\rangle = 2nD. \tag{2.11}$$

Integrating both sides of Eq 2.11 gives

$$\langle \Delta r^2(\tau)\rangle = 2nD_T\tau, \tag{2.12}$$

where D_T is the translational diffusion coefficient. Einstein showed the general relation for a particle of un-described shape that D_T is given by,

$$D_T = \frac{k_B T}{\xi}. \tag{2.13}$$

This can be simply thought of as the ratio of thermal energy, $k_B T$, and the friction coefficient, ξ. Combing Eq 2.13 with the Stokes friction coefficient for a spherical particle gives the Stokes-Einstein Debye Equation for D_T [6],

$$D_T = \frac{k_B T}{6\pi\eta R}. \tag{2.14}$$

Here, R is the radius of the particle and η is the viscosity of the surrounding medium. For translational dynamics we can define a characteristic time, τ_T, as the time taken for a particle to diffuse over a distance equal to its own diameter. If we define this timescale in 3D using Eqs 2.12 and 2.14 we reach the following expression,

$$\tau_T = \frac{6\pi\eta R^3}{k_B T}. \tag{2.15}$$

For a 1 μm particle in water τ_T is equal to 3s. So the typical timescale for a typical colloidal particle of μm-size is on the order of 1s which is easily captured on an optical microscope.

2.1.2 Rotational Dynamics of Colloidal Particles

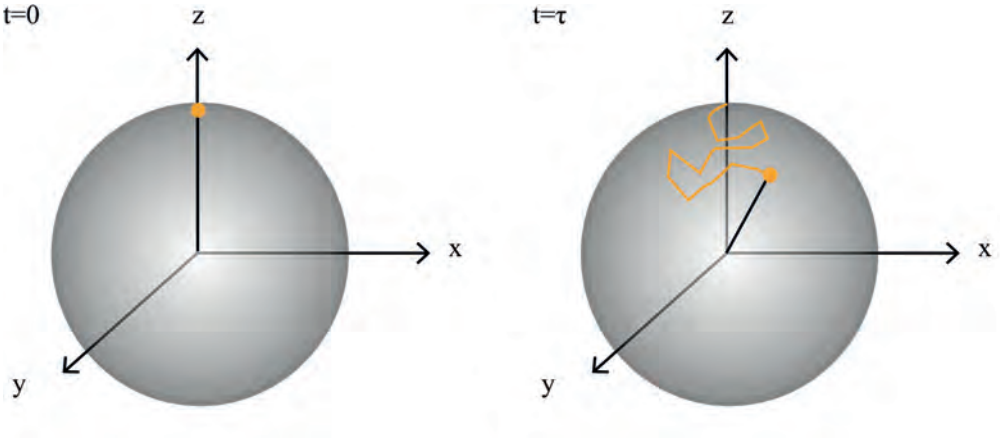

Figure 2.1: Diagram representing the rotational diffusion of a spherical particle as diffusion of a point over the surface of the unit sphere. Initial orientation at $t = 0$ lies along the z-axis. After a period of time, τ, the orientation has changed as represented by the path across the surface of the sphere.

For a colloidal particle suspended in a solvent the fluctuating force the particle experiences, due to collision with the solvent molecules, also leads to a Brownian rotational motion. We can derive the relation between rotational displacement and time by considering the relaxation of the initial orientation of a particle. The following derivation is largely reproduced from Ref [1, 9]. We consider a particle with a reference axis that runs along the direction of the initial orientation, the rotational diffusion can be considered as the diffusion of a point along the surface of the sphere [1]. This is illustrated in Fig 2.1. We can define a diffusion equation for this scenario as,

$$\frac{\partial}{\partial t}P(\theta,\phi,t) = D_R\nabla^2 P(\theta,\phi,t), \tag{2.16}$$

where $P(\theta,\phi,t)$ is the probability density that the point will be located at spherical coordinates θ,ϕ at time t. We can also define the orientation as the unit vector $\hat{u}$. The relaxation in the orientation is given by the decay in the auto-correlation function defined as,

$$\langle \hat{u}(t_0)\cdot\hat{u}(t_0+t)\rangle = \langle \cos\theta(t)\rangle. \tag{2.17}$$

As $u(t_0)$ lies along the z-axis $P(\theta, \phi, t)$ becomes independent of ϕ and can be simplified to $P(\theta, t)$. Therefore was can evaluate the expected value of the auto-correlation function as,

$$\langle \cos\theta(t) \rangle = \int P(\theta) \cos\theta \sin\theta d\theta d\phi, \tag{2.18}$$

which simplifies to,

$$\langle \cos\theta(t) \rangle = 2\pi \int_0^\pi P(\theta) \cos\theta \sin\theta d\theta. \tag{2.19}$$

As we are aiming to derive the relation between the rotational displacement and time, we take the time derivative and arrive at the following expression,

$$\frac{\partial}{\partial t} \langle \cos\theta(t) \rangle = 2\pi \int_0^\pi \frac{\partial}{\partial t} P(\theta) \cos\theta \sin\theta d\theta. \tag{2.20}$$

This allows us to re-write the diffusion equation given in Eq 2.16 as,

$$\frac{\partial}{\partial t} \langle \cos\theta(t) \rangle = 2\pi D_R \int_0^\pi (\nabla^2 P(\theta)) \cos\theta \sin\theta d\theta. \tag{2.21}$$

Expressing ∇^2 in spherical coordinates and applying two partial integrals gives the differential equation,

$$\frac{\partial}{\partial t} \langle \cos\theta(t) \rangle = -2D_R \int_0^\pi (P(\theta)) \cos\theta \sin\theta d\theta = -2D_R \langle \cos\theta(t) \rangle. \tag{2.22}$$

The solution to the above differential equation is given by,

$$\frac{\partial}{\partial t} \langle \cos\theta(t) \rangle = e^{-2D_R t}, \tag{2.23}$$

where D_R is given by the Stoke-Einstein-Debye Equation [10],

$$D_R = \frac{kT}{8\pi\eta R^3}. \tag{2.24}$$

The typical rotational relaxation time is defined as [1, 10],

$$\tau_R = \frac{1}{2D_R}. \tag{2.25}$$

By substituting Eq 2.24 we obtain the expression,

$$\tau_R = \frac{4\pi\eta R^3}{k_B T}. \tag{2.26}$$

For a colloidal particle of radius 1 μm in water τ_R is equal to 1.5s. Therefore the rotational dynamics of typical colloidal particles are also observable on a typical optical microscope.

2.1.3 Rotational Displacement

Evaluating the rotational dynamics in terms of the unit orientation has a major limitation. There is no rotational trajectory; the unit orientation after time τ has no memory of how the particle has rotated to reach that point. Therefore, orientations at long time lag will simply show no correlation. A new method of evaluating the rotational displacement was developed by Hunter *et al* [11]. To build up a rotational trajectory analogous to the translational trajectory we first define the rotational displacement between the unit orientation in frame t_1, $\hat{u}(t_1)$, and the orientation in the next frame t_2, $\hat{u}(t)$, as $\psi(t_2)$,

$$\psi(t_2) = \hat{\omega} \cdot \alpha, \tag{2.27}$$

where $\hat{\omega}$ is the axis of rotation between frames, $\hat{\omega} = \hat{u}(t_1) \times \hat{u}(t_2)$, and α is the angle of rotation, $(\alpha = \cos^{-1}(\hat{u}(t_1) \cdot \hat{u}(t_2)))$, as shown in Fig 2.2a) To build the individual

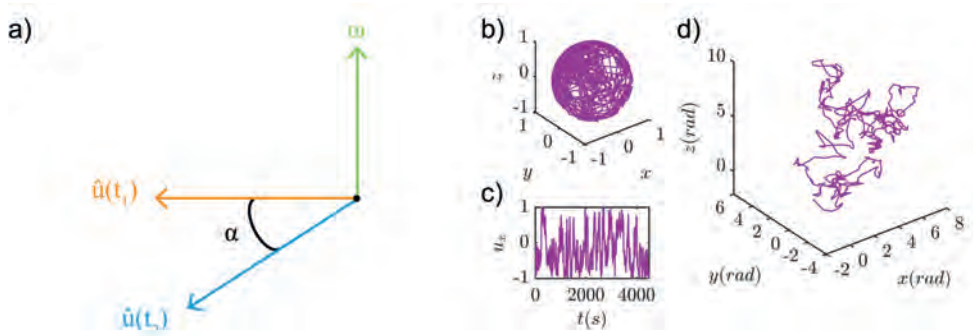

Figure 2.2: a) Schematic representation of unit orientations $\hat{u}(t_1)$ and $\hat{u}(t_2)$ and the axis of rotation between them, $\hat{\omega}$. b) Example rotational trajectory projected onto unit sphere. c) x component of unit trajectory plotted against time. d) Extracted rotational trajectory $\theta(t)$ for same particle.

displacements into a trajectory we evaluate the integral,

$$\theta(\tau) = \int_1^{t_2} \psi(t)dt. \tag{2.28}$$

This results in a rotational trajectory for each particle in cartesian coordinates as shown in Fig 2.2d). The rotational displacement θ can be treated in a similar way as a translational trajectory. We can therefore define a rotational analogue to the mean-squared displacement, the mean squared *angular* displacement as,

$$\langle \Delta\theta^2 \rangle = 4D_R\tau. \tag{2.29}$$

Here D_R is the rotational diffusion coefficient as defined in Eq 2.24. The advantage of the rotational trajectory is that it allows long time behaviour of rotational dynamics to be evaluated. However we note that defining the orientation as a single 3D vector allows a degeneracy where the particle can rotate around the axis or orientation.

In an experimental system the particle orientation may be lost for some frames of the total trajectory due to particle tracking errors. This can lead to a cumulative error in the calculation of the rotational trajectory (Eq 2.28). To account for this, we apply the following exclusion criterion: tracks are only retained if the particle orientation is

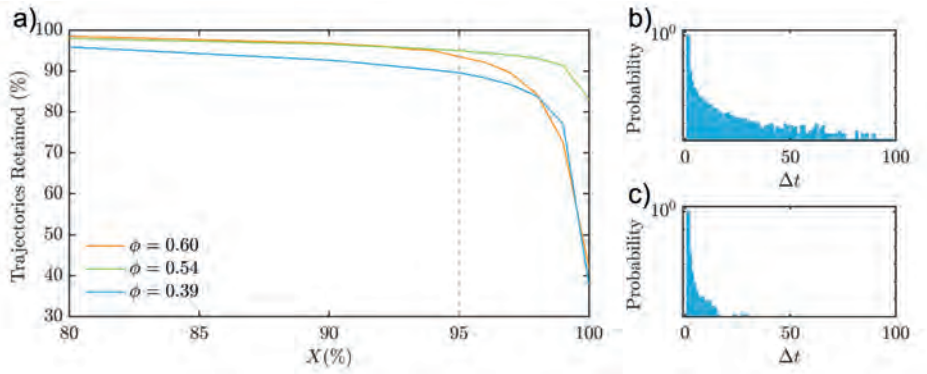

Figure 2.3: a) Percentage of particle tracks retrained for different values of X for $\phi = 0.60$, $\phi = 0.54$, and $\phi = 0.39$. b) Histogram of the time gaps between consecutive frames in the particle trajectories for $\phi = 0.39$ *before* the criterion ($X = 95\%$, see text) is applied. c) Histogram of the time gaps between consecutive frames in the particle trajectories for $\phi = 0.39$ *after* the criterion ($X = 95\%$, see text) is applied.

known for at least ($X =$)95% of the maximum length of the track. How this criterion affects the total fraction of retained particles is demonstrated in Fig 2.3a), where we plot the fraction of retained trajectories for various values of X for three different volume fractions: $\phi = 0.60$ (glass), $\phi = 0.54$ (crystal) and $\phi = 0.39$ (fluid). Clearly, as X increases, in total fewer but more accurate trajectories are retained. In this thesis, we apply a threshold of $X = 95\%$, which corresponds to retaining $> 90\%$ of all the particles. In Fig 2.3b) and c) we show the histogram for the gaps between consecutive frames in the trajectories, Δt, for $\phi = 0.39$ before and after the exclusion criterion ($X = 95\%$) has been applied. Clearly, the number of trajectories with large frame gaps is drastically reduced, which is crucial for obtaining more accurate rotational trajectories. In summary, by applying this criterion we ensure that we can build accurate rotational trajectories (according to Eq 2.28), whilst also retaining the majority ($> 90\%$) of all the particles in our system.

2.1.4 Interactions of Colloidal Particles

The interactions of colloidal particles dispersed in a solvent is an intricate balance between the attractive and repulsive interactions. This balance was famously described by Derjaguin–Landau–Verwey–Overbeek as the DLVO potential [12, 13]. The total interaction potential, $U(r)$ is considered as the sum of the individual contributions from the attractive and repulsive interactions,

$$U(r) = U_{att} + U_{rep}. \tag{2.30}$$

The attractive interactions between particles can be understood by considering that each particle is the sum of its molecules. Each molecule of each colloidal particle experiences a Van der Waals attraction to each molecule of a neighbouring particle. The van der Waals attraction between each pair of molecules scales as $\propto -1/r^6$, where r is the separation between the pair. The total Van der Waals attraction can be evaluated by assuming pairwise additivity, and the total interaction is then the sum of the interactions between each pair of molecules [13]. For two spherical particles interacting over a separation, D, smaller than particle radius, R, the total Van der Waals attraction, U_{VDW}, is given by;

$$U_{att} = U_{VDW} = -\frac{A_{12}R}{12D}. \tag{2.31}$$

For a pair of particles of the same material, material 1, interacting across a medium of material 2 the Hamaker constant can be approximated by [13].,

$$A = \frac{3}{4}k_BT\left(\frac{\varepsilon_2 - \varepsilon_1}{\varepsilon_2 + \varepsilon_1}\right) + \frac{3h\nu_e}{16\sqrt{2}}\left(\frac{(n_1^2 - n_2^2)}{(n_1^2 + n_2^2)^{\frac{3}{2}}}\right). \tag{2.32}$$

In a non-polar solvent the contribution from the dielectric term is negligible [14] and the expression simplifies to,

$$A \approx \frac{3h\nu_e}{16\sqrt{2}}\left(\frac{(n_1^2 - n_2^2)}{(n_1^2 + n_2^2)^{\frac{3}{2}}}\right) \tag{2.33}$$

The contribution of U_{VDW} to the overall interaction can thus be reduced by matching the refractive index of the particle to that of the solvent.

If both particles are made from the same material, A is always positive and therefore U_{VDW} is always attractive. So, if U_{VDW} were the sole interaction between colloidal particles of the same type, they would simply irreversibly aggregate once close enough. However, most of the common colloidal building blocks produce particles with a charged

surface [15–17]. In a dielectric solvent the ions in the solution act to screen this charge. Some ions are bound close to the particle surface in the Stern layer while some are held in a more diffuse atmosphere further from the surface, in the electric double-layer. The decay length of the screened electric field around the particle is characterised by the Debye length, κ^{-1},

$$\kappa^{-1} = \sqrt{\frac{\varepsilon\varepsilon_0 k_B T}{2e^2 n_0 z^2}}. \tag{2.34}$$

Here e is the elementary charge, n_0 is the salt concentration and z is the charge valency. The total screened electrostatic potential between two charged colloids, U_{DLR}, can be approximated by a Yukawa potential [18],

$$U_{rep} = U_{DLR} = Z^2 k_B T \lambda_B \left(\frac{\exp(\kappa R)}{1+\kappa R}\right)^2 \frac{\exp(-\kappa r)}{r}, \tag{2.35}$$

where Z is the effective surface charge of the particle and λ_B is the Bjerrum length, the separation at which the interaction potential between opposite elementary charges equals $k_B T$. At separations larger than R, U_{DLR} scales as $\frac{\exp(-\kappa r)}{r}$ which, allows this interaction potential to be tuned by altering κ^{-1}. From Eq 2.34, it is inferred that increasing the salt concentration or screening agent in solution shortens the Debye length which causes a subsequent decrease in U_{DLR}. Therefore, similarly to U_{VDW}, U_{DLR} is also controllable in an experimental colloidal system.

The total interaction potential, and the two separate contributions, are shown in Fig 2.4a). U_{DLR} provides a barrier to aggregation at short separations but due to the longer

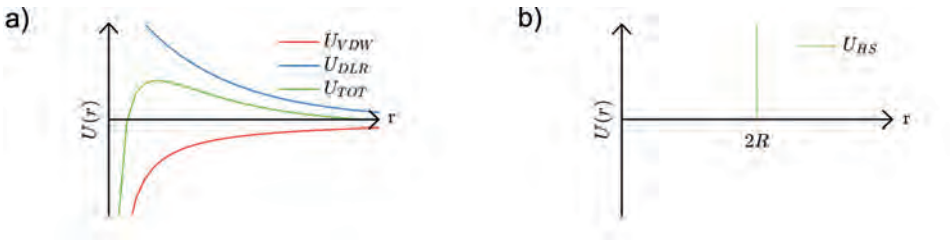

Figure 2.4: a) DLVO Potential shown as the individual contributions from U_{VDW} and U_{DLR} and well as U_{TOT}. b) Hard-Sphere Interaction Potential, where $2R$ is the hard sphere diameter.

decay length of U_{VDW} an attraction at longer distance appears. However, as previously stated a major advantage of the colloidal model system is that the, interaction potential can be controlled by choice of solvent and addition of salt or a screening agent. Therefore the *total interaction potential* can be controlled. In this thesis the particles are all of the same material and possess a negative surface charge. U_{VDW} is minimised by refractive index matching the particle and solvent and the range of U_{DLR} is minimised by adding a screening agent. Therefore the particles have a steeply repulsive interaction potential, which is almost like a hard sphere [9], which is shown in Fig 2.4b).

2.1.5 Phase Behaviour of Colloidal Systems

The phase behaviour of colloidal systems is directly analogous to that of molecular or atomic systems [19]. Instead of being controlled by temperature phase behaviour in colloidal systems is controlled by volume fraction, $\phi = \frac{n_p \cdot v_p}{v}$. Here, n_p is the number of particles, v_p is the particle volume and v is the total volume. At low ϕ, a spherical colloidal particle system exists in a dilute fluid phase. As ϕ increases the fluid phase becomes increasing dense until a phase transition from the disordered fluid to the highly ordered colloidal crystal takes place [19]. The driving force behind this transition can be rationalised by considering the suspension acts to minimise its Helmholtz free energy, A,

$$A = U - TS \tag{2.36}$$

The minimisation of A is, perhaps somewhat counterintuitevly, achieved by maximising entropy, S as for a hard sphere system the internal energy only has a contribution from the kinetic energy.

Despite the increase in order in the crystal phase the particles have more free volume than in the disordered fluid phase. This increase in entropy associated with the increase in free volume compensates for the decrease in entropy due to the decrease in order. Therefore a hard-sphere colloidal suspension in equilibrium above $\phi > 0.54$ will form a crystal phase as opposed to the disordered fluid phase. To achieve the glass phase the system must be forced out of equilibrium by quickly increasing the volume fraction $\phi > 0.58$ to frustrate the system typically by centrifugation or rapid sedimentation of particles [20]. More commonly, to prevent crystallisation polydisperse or binary

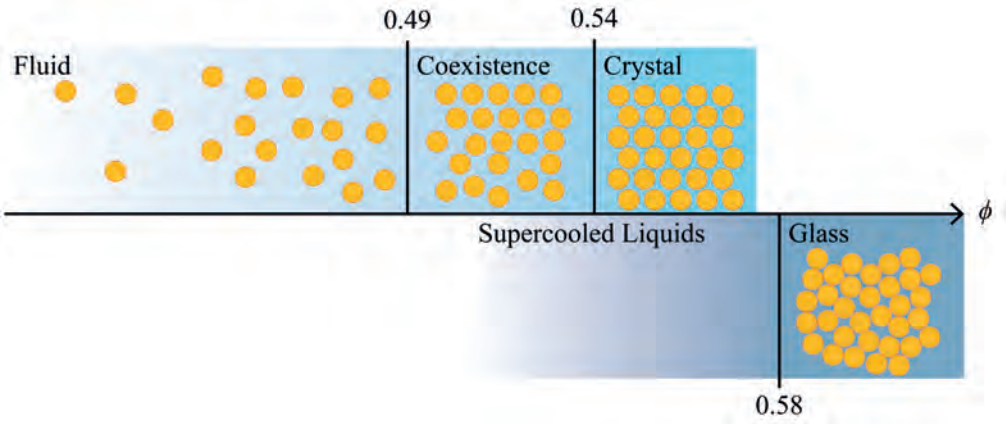

Figure 2.5: Phase diagram for colloidal particles with a hard sphere interaction potential.

mixtures are used to investigate the glass phase [21–25].

2.1.6 Gravitational Length

When a dilute colloidal suspension is left to equilibrate under gravity it will exhibit a decay in density, in the direction of gravity, described as [7],

$$n(z) = n(0) \exp\left(-\frac{z}{\xi_g}\right). \tag{2.37}$$

The decay length of this distribution, ξ_g, is known as the gravitational length of the suspension and is described by,

$$\xi_g = \frac{k_B T}{\Delta m g}. \tag{2.38}$$

Here Δm is the buoyant mass of a particle in the suspension defined as $\Delta m = v_p(\rho_p - \rho_s) = \frac{4\pi R^3 \Delta\rho}{3}$ where $\Delta\rho = \rho_p - \rho_s$, is the mass density difference between the particle and the solvent. Therefore the gravitational length can be thought as the height a particle is able to reach due to the thermal energy. The gravitational length can therefore be tuned by altering Δm. In practice this is done by either altering the size of a particle, smaller particles have a smaller Δm and therefore longer ξ_g or by increasing

the density matching between particle and solvent, again reducing Δm and therefore lengthening ξ_g. Colloidal suspensions of a certain volume fraction can be prepared in a density matched solution ($\Delta m \approx 0$) where $\xi_g \to \infty$ so a homogeneous density, and therefore phase, can be observed throughout the sample. In this thesis we prepare samples where $\Delta m > 0$ and the particles form a sedimentation-diffusion equilibrium in the direction of gravity. This allows the study of multiple different packing fractions, and therefore multiple phases, throughout a single sample.

2.2 Experimental Methods

In this section we will discuss the main aspects of the experimental methods used in this thesis including the main particle synthesis pathways and the mechanism behind it, as well as the microscopy and particle tracking techniques used.

2.2.1 Particle Synthesis

Over the last century various particle systems have been developed to produce particles of a cavalcade of sizes, shapes and properties [3–5]. Colloids can also be synthesised from a range of materials [4, 26–29]. This work focuses on the dynamics of colloidal microspheres. Typically the synthesis of colloidal microspheres occurs via either dispersion, breaking a material down into smaller subspecies or condensation, building smaller nuclei into larger species. The second category can be further divided into two subcategories emulsion polymerisation, in an aqueous phase, or dispersion polymerisation, in an organic phase. The particles used in this work are formed via an emulsion polymerisation mechanism using the monomer 3-(trimethoxysilyl)propyl methacrylate.

The reaction mechanism to form a suspension of monodisperse droplets of TPM microspheres is shown in Fig 2.6. First, TPM is first pre-hydrolysed in acid before a condensation reaction is triggered by addition of an aqueous base. As the monomer reacts the polymer concentration increases, which is shown schematically in Fig 2.7. Eventually the polymer reaches a critical molecular mass which triggers rapid nucleation. This nucleation is driven by the decrease in solubility in water with increasing polymer size [30]. Above this concentration new nuclei continue to be precipitated out while existing nuclei grow by continued addition of polymer into the nuclei or direct reaction of the nuclei with the monomer. This nucleation window is

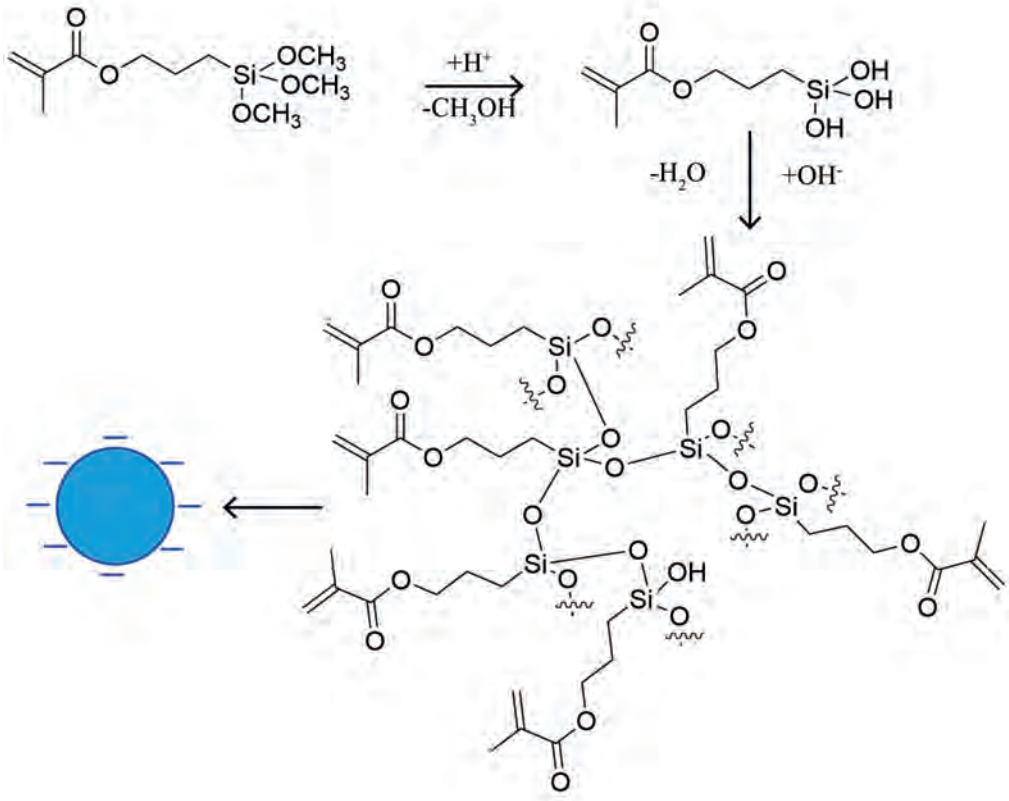

Figure 2.6: Reaction mechanism for the synthesis of TPM microspheres.

indicated by the shaded region in Fig 2.7. Eventually the polymer concentration in solution begins to drop below the critical concentration and no new nuclei are created and only growth occurs. The resulting droplets are stabilised by electrostatics and can be cross-linked to form solid colloidal microspheres.

The bulk of this thesis utilises the wetting properties of TPM to produce a unique colloidal particle that features a small TPM microsphere, the eye, embedded off centre in a larger TPM microsphere, the body. If the two components are

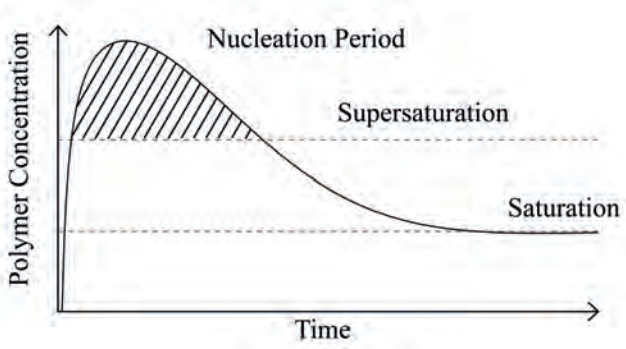

Figure 2.7: La Mer diagram for the nucleation and growth model of particle synthesis.

labelled with different fluorescent dyes they can both be simultaneously imaged and independently tracked to allow direct observation of the rotational and translational dynamics of spherical particles [9]. Therefore, this particle is referred to as an 'Off-Centre-Under-Laser-Illumination' (OCULI) particle. A schematic for the synthesis of the OCULI particle is shown in Fig 2.8. First pre-hydrolysed TPM is dripped onto the surface of a TPM microsphere. The microsphere is eventually engulfed inside a droplet but due to interfacial pinning it is held off-centre within the droplet where it remains after the liquid layer is cross-linked to form a solid microsphere [31].

Imaging entirely fluorescent particle under confocal or fluorescence microscopy often causes errors during particle tracking at high volume fraction due to the overlap in the fluorescence signal of neighbouring particles. Creating a non-fluorescent shell around the particle increases the accuracy of particle location even in dense packings [26, 27]. This can be achieved by making a core-shell OCULI particle entirely from TPM through a two step process, illustrated in Fig 2.8, which exploits the wetting behaviour of liquid TPM on solid TPM [17]. During the OCULI synthesis, before the body is crosslinked, a surfactant, F108, is added to the suspension which adsorbs to the surface of the droplet. Once the particle is crosslinked the surfactant remains at the particle surface. When hydrolysed TPM wets onto the surface but instead of engulfing the particle distinct lobes are formed on the surface as illustrated in Fig 2.8. Once these lobes are crosslinked subsequent addition of TPM wets in between these lobes allowing the particle to regain a spherical shape. If both the lobes and the TPM between them is left undyed this results in a non-fluorescent shell with the fluorescent OCULI particle at the centre.

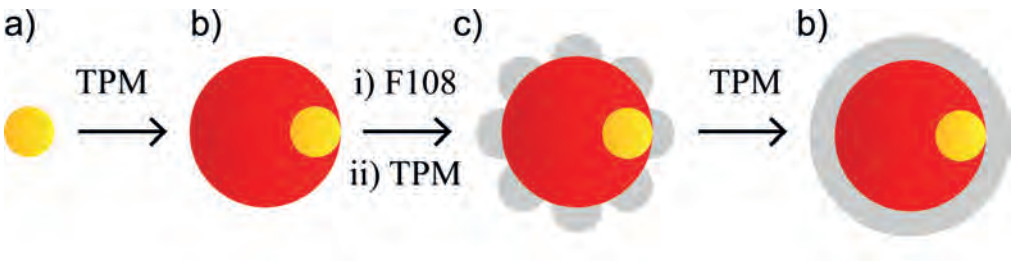

Figure 2.8: Schematic representation of particle synthesis.a) TPM microsphere. b) TPM Microsphere with smaller TPM microsphere embedded off-centre within it. c) TPM microsphere with TPM lobes. d) Core-Shell TPM microsphere.

2.2.2 Confocal Microscopy

In the first half of the 20th century biologists struggled to capture images with flourescently labelled samples due to poor resolution caused by out of plane fluorescence. In 1955 Marvin Minsky built the first rudimentary confocal microscope to overcome this barrier. Key to his approach was the inclusion of two 'pinholes' which removed out of plane light and thus increased the resolution of the image [32, 33]. It was not until several decades later when the technology, and thus image quality, improved that confocal microscopy was first used to directly visualise particle dynamics in 3D [34]. The most commonly used variation of this, and the type used in this thesis, is confocal laser scanning microscope (CLSM). Here we discuss the basic principles of confocal microscopy.

A schematic of the confocal microscope used in this thesis is shown in Fig 2.9. Light of wavelength λ_{EX} is emitted from a laser source and passes through a dichroic filter. The scanning mirrors deflect the light off-axis such that the objective focuses the excitation light in the focal plane but laterally shifted. The lateral shift in x is controlled by a resonance mirror, which operates at 12kHz. The field of view is scanned in x before the excitation light is laterally shifted in y by a galvanometer mirror which operates at lower frequencies. The fluorescence is recorded as light of wavelength λ_{EM}. The emitted light is de-scanned by the scanning mirror and passed back to the dichroic filter. As λ_{EX} and λ_{EM} are well spectrally separated, only λ_{EM} is reflected by the dichroic mirror. The excited light passes through a pinhole which restricts any out of focus light and the fluorescence at each point is detected by the photo-multiplier-tube (PMT). Once this has been recorded for each pixel in a 2D slice the process is repeated for the 2D slice directly above. This is carried out by mounting the objective on a

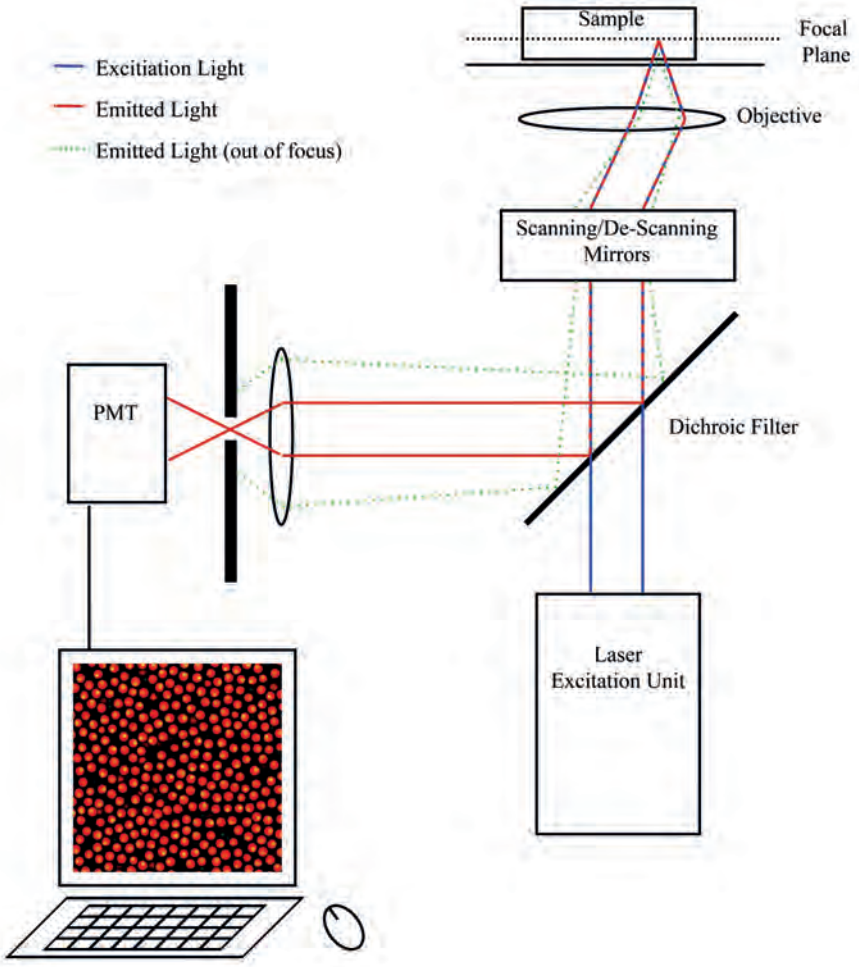

Figure 2.9: Schematic of the operating principles of Confocal Microscopy.

piezoelectric z-stage, which moves the objective in z, the optical axis, to the position of the next slice. A 3D image can then be constructed from the individual 2D images at different heights.

In this thesis λ_{EX} of 488 and/or 532nm is provided by a ThorLabs Multi Channel Fibre Coupled Laser Source, and two-channel images of the fluorescence from the eye and the body of the OCULI particle are recorded simultaneously. The sample is imaged using a 60× Olympus PlanApo objective (Numerical Aperture, (NA)=1.42) oil immersion objective mounted on a piezoelectric z-stage (Physik Instrumente). Scanning was carried out by a 12kHz ThorLabs scan head where typically a $102.4\times102.4\times50.2\mu m^3$ volume was recorded for two-channels in 5.9s.

The spatial resolution in x and y of a microscope can be quantified by the Abbe diffraction limit [35],

$$d = \frac{\lambda}{2\mathrm{NA}} = \frac{\lambda_{EM}}{2n\sin\alpha}, \tag{2.39}$$

where n is the refractive index of the medium and α is the angle of the cone of illumination of the sample. In this thesis $d \approx 200nm$ in a typical experiment. For a confocal system d also provides the limiting values for the size of the pinhole to provide the ideal imaging conditions. In a confocal microscope the resolution along the optical axis, z, is poorer, at best $500nm$ due to the elongation of the point-spread function in z [36]. Of the wide variety of colloidal particle systems commonly available today the ones more suitable for confocal microscopy allow for refractive index matching between the particle and the solvent. If the refractive index of the solvent does not match the refractive index of the colloidal particle scattered light greatly increases the noise in the image and limits how deep in the sample it is possible to image clearly in z. We demonstrate in Chapter 3 that TPM is well suited to CLSM as it can be easily, and homogeneously, flourescently labelled and has a refractive index that is easily matched with common organic solvents.

2.2.3 Particle Localisation and Image Analysis

Particle tracking methods developed by Crocker and Grier were a major step forward in the study of colloidal systems as they allowed particle to be located to sub-pixel

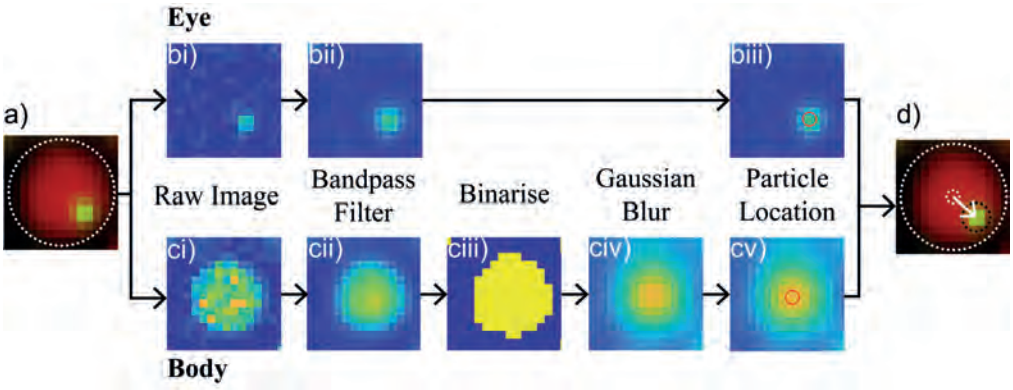

Figure 2.10: Schematic of image analysis procedure. a) Two channel confocal image OCULI particle. bi) Raw image from eye channel. bii) Eye channel after 3D bandpass filter. biii) Eye channel after 3D bandpass filter where marker shows result of particle tracking. ci) Raw image from body channel. cii) Body channel after 3D bandpass filter. ciii) Body channel after binarisation. civ) Re-smoothed body channel. cv) Resmoothed body channel where marker shows result of particle tracking. d) Output of particle tracking showing how location of body and eye coordinates yields particle orientation.

accuracy from a microscope image [37]. Initially developed for 2D bright field images the same process has since been extended to 3D confocal images. To extract both the translational and rotational dynamics from each OCULI particle both the body and eye must be independently tracked as demonstrated in Fig 2.10. The eye of the OCULI is tracked using standard particle tracking procedures. First the 3D image is passed through a 3D bandpass filter to remove both noise and the background. Then local maxima are found in the image in 3D based on their intensity. To locate the centre to sub-pixel accuracy the intensity around each maxima is fit with a Gaussian function in x, y and z. To remove any bias in the fluorescence profile due to the presence of the eye the body channel is binarised after bandpass filtering and resmoothed using a Gaussian blur. The position is then found to sub-pixel accuracy by fitting the fluorescence profile in x, y and z with a quadratic function. Once the 3D coordinates of the body and eye are extracted they are linked together so we can obtain the orientation of every particle, as illustrated in Fig 2.10. Therefore we can track the translational dynamics and rotational dynamics for every particle in the population.

2.3 Bibliography

[1] A. P. Philipse. *Brownian motion.* Undergraduate Lecture Notes in Physics. Springer International Publisher, Cham, 2018.

[2] A. van Blaaderen. Opals in a new light. *Science*, 282(5390):887–888, 1998.

[3] T. Hueckel, G. M. Hocky, and S. Sacanna. Total synthesis of colloidal matter. *Nat. Rev. Mater.*, 6(11):1053–1069, 2021.

[4] M. Kamp, S. Sacanna, and R. P. A. Dullens. Spearheading a new era in complex colloid synthesis with tpm and other silanes. *Nat. Rev. Chem.*, 8(6):433–453, 2024.

[5] S. Sacanna and D. J. Pine. Shape-anisotropic colloids: Building blocks for complex assemblies. *Curr. Opin. Colloid Interface Sci.*, 16(2):96–105, 2011.

[6] A. Einstein. *Investigations on the Theory of the Brownian Movement.* Courier Corporation, 1956.

[7] J. Perrin. Mouvement brownien et réalité moléculaire. *Ann. Chim. Phys.*, 19(8):5–104, 1909.

[8] W. C. K. Poon. Colloids as big atoms. *Science*, 304(5672):830–831, 2004.

[9] T. Yanagishima, Y. Liu, H. Tanaka, and R. P. A. Dullens. Particle-level visualization of hydrodynamic and frictional couplings in dense suspensions of spherical colloids. *Phys. Rev. X*, 11:021056, 2021.

[10] P. J. W. Debye. *Polar Molecules.* Dover Publications, 1929.

[11] Gary L. H., K. V. Edmond, M.T. Elsesser, and E. R. Weeks. Tracking rotational diffusion of colloidal clusters. *Opt. Express*, 19(18):17189–17202, 2011.

[12] D F. Evans and H. Wennerström. *The Colloidal Domain: where Physics, Chemistry, Biology, and Technology meet.* Wiley-Vch New York, 1999.

[13] J. N. Israelachvili. *Intermolecular and surface forces.* Academic press, 2011.

[14] P. S. Yadav, D. Dupre, R. Tadmor, J. S. P., and D. Katoshevski. Effective refractive index and intermolecular forces associated with a phase of functional groups. *Surf. Sci.*, 601(19):4582–4585, 2007.

[15] A. Yethiraj and A. van Blaaderen. A colloidal model system with an interaction tunable from hard sphere to soft and dipolar. *Nature*, 421(6922):513–517, 2003.

[16] S. H. Behrens and D. G. Grier. Pair interaction of charged colloidal spheres near a charged wall. *Phys. Rev. E*, 64:050401, 2001.

[17] Y. Liu, T. Yanagishima, A. Curran, K. V. Edmond, S. Sacanna, and R. P. A. Dullens. Colloidal organosilica spheres for three-dimensional confocal microscopy. *Langmuir*, 35(24):7962–7969, 2019.

[18] J. A. Weiss, A. E. Larsen, and D. G. Grier. Interactions, dynamics, and elasticity in charge-stabilized colloidal crystals. *J. Chem. Phys.*, 109(19):8659–8666, 1998.

[19] P. N. Pusey and W. van Megen. Phase behaviour of concentrated suspensions of nearly hard colloidal spheres. *Nature*, 320(6060):340–342, 1986.

[20] W. K. Kegel. Crystallization in glassy suspensions of colloidal hard spheres. *Langmuir*, 16(3):939–941, 2000.

[21] T. Narumi, S. V. Franklin, K. W. Desmond, M. Tokuyama, and E. R. Weeks. Spatial and temporal dynamical heterogeneities approaching the binary colloidal glass transition. *Soft Matter*, 7(4):1472–1482, 2011.

[22] T. Sentjabrskaja, E. Babaliari, J. Hendricks, M. Laurati, G. Petekidis, and S. U. Egelhaaf. Yielding of binary colloidal glasses. *Soft Matter*, 9(17):4524–4533, 2013.

[23] S. R. Williams and W. van Megen. Motions in binary mixtures of hard colloidal spheres: Melting of the glass. *Phys. Rev. E*, 64(4):041502, 2001.

[24] R. Kurita and E. R. Weeks. Glass transition of two-dimensional binary soft-disk mixtures with large size ratios. *Phys. Rev. E*, 82:041402, Oct 2010.

[25] D. Heckendorf, K. J. Mutch, S. U. Egelhaaf, and M. Laurati. Size-dependent

localization in polydisperse colloidal glasses. *Phys. Rev. Lett.*, 119(4):048003, 2017.

[26] R. P. A. Dullens, M. Claesson, D. Derks, A. van Blaaderen, and W. K. Kegel. Monodisperse core- shell poly (methyl methacrylate) latex colloids. *Langmuir*, 19(15):5963–5966, 2003.

[27] A. van Blaaderen and A. Vrij. Synthesis and characterization of colloidal dispersions of fluorescent, monodisperse silica spheres. *Langmuir*, 8(12):2921–2931, 1992.

[28] C. Fernández-Rico, T. Yanagishima, A. Curran, D. G. A. L. Aarts, and R. P. A. Dullens. Synthesis of colloidal su-8 polymer rods using sonication. *Adv. Mater.*, 31(17):1807514, 2019.

[29] B.R. Saunders and B. Vincent. Microgel particles as model colloids: theory, properties and applications. *Adv. Colloid Interface Sci.*, 80(1):1–25, 1999.

[30] C. van der Wel, R. K. Bhan, R. W. Verweij, H. C. Frijters, Z. Gong, A. D. Hollingsworth, S. Sacanna, and D. J. Kraft. Preparation of colloidal organosilica spheres through spontaneous emulsification. *Langmuir*, 33(33):8174–8180, 2017.

[31] V. N. Manoharan. Pinned down. *Nat. Mater.*, 14(9):869–870, 2015.

[32] S. W. Paddock, T. J. Fellers, and M. W. Davidson. *Confocal Microscopy*. Springer, 2014.

[33] S. W. Paddock. Principles and practices of laser scanning confocal microscopy. *Mol. Biotechnol.*, 16:127–149, 2000.

[34] A. van Blaaderen and P. Wiltzius. Real-space structure of colloidal hard-sphere glasses. *Science*, 270(5239):1177–1179, 1995.

[35] A. Lipson, S. G. Lipson, and H. Lipson. *Optical Physics*. Cambridge University Press, 2010.

[36] V. Prasad, D. Semwogerere, and E. R Weeks. Confocal microscopy of colloids. *J. Phys. Condens. Matter*, 19(11):113102, 2007.

[37] J. C. Crocker and D. G. Grier. Methods of digital video microscopy for colloidal studies. *J. Colloid Interface Sci.*, 179(1):298–310, 1996.

Chapter 3

Characterisation and Optimization of Fluorescent Organosilica Colloids for 3D Confocal Microscopy Prepared Under 'Zero-Flow'

We optimise and characterise the preparation of 3-trimethoxysilyl propylmethacrylate (TPM) colloidal suspensions for three-dimensional confocal microscopy. We revisit a simple synthesis of TPM microspheres by nucleation of droplets from pre-hydrolysed TPM oil in a 'zero-flow' regime, and demonstrate how precise and reproducible control of particle size may be achieved via single-step nucleation with a focus on how the reagents are mixed. We also revamp the conventional dyeing method for TPM particles to achieve uniform transfer of a fluorophore to the organosilica droplets, improving particle identification. Finally, we illustrate how a ternary mixture of tetralin, trichloroethylene and tetrachloroethylene may be used as a suspension medium which matches the refractive index of these particles while allowing independent control of the density mismatch between particle and solvent.

3.1 Introduction

Colloidal particles have been widely used as a model system to study condensed matter phenomena, including crystallization [1–3], gelation [4–7] and glass formation [8–11]. The development of confocal microscopy has allowed direct observation of fluorescently labeled colloidal systems in three dimensions; with the right choice of particle density and a solvent with a matching refractive index, the positions of all particles in an observation window may be tracked over time with single-particle resolution [12, 13], offering the prospect of 'complete' knowledge of the structural state of the system.

However, the most common colloidal systems e.g. poly-methyl methacrylate (PMMA) [14], silica [15], poly(n-isopropylacrylamide) (PNIPAM) [16], polystyrene [17, 18] have distinct hurdles to their use in three-dimensional studies. These range from inherent softness in refractive index matching solvents (e.g.PNIPAM), to the expertise required to make the particles from scratch (e.g. PMMA), and difficulty in matching refractive index and/or density with a solvent (e.g. silica, polystyrene). As a more accessible solution, Sacanna *et al.* [19, 20], and later by an alternative pathway Van der Wel *et al.* [21] proposed the condensation of 3-(trimethoxysilyl)propyl methacrylate (TPM) in a base to produce monodisperse colloidal spheres at the micron-scale. Further work by Liu *et al.* demonstrated that common organic solvents and a solvent transfer procedure could be used to suspend these TPM particles and create a refractive index matched suspension suitable for confocal microscopy [22, 23]. TPM as a colloidal material has been repeatedly shown to be versatile in the creation of different particle shapes [19], tuneable interactions [24] and fluorescence profiles [23, 25], making it an ideal system for 3D microscopy.

Yet, there are issues that remain to be addressed. In brief, synthesis of TPM particles involves the formation of charge-stabilized oil-in-water emulsion via hydrolysis and condensation of TPM; these droplets are then subsequently crosslinked into particles [20]. Monodisperse TPM emulsion droplets were first made by Sacanna *et al.* as precursors to dimpled particle formation [19]. In their procedure, they describe the hydrolysis of TPM in water before adding ammonia to nucleate; hydrolysed TPM is then added for further growth. Van der Wel *et al.* [21] described the particle formation in a fuller manner, only now adding TPM oil to a stirring solution of base for simultaneous hydrolysis and condensation: this is now considered the 'conventional' TPM synthesis. However, certain aspects remain difficult to control [21, 26], particularly in producing particles of an exact target size. Middleton *et al.* [26] have demonstrated that stirring

speed directly impacts final particle size, but in a non-monotonic fashion. The effect of stirring was also noted by Neibloom *et al.* [27], who noted that increased particle collisions may cause particle aggregation. Clearly, the flow field has a strong impact on target diameter and size distribution. But an identical flow profile is difficult to replicate between batches, as it is dictated by not only the speed of rotation of the stirrer but its shape and position, as well as vessel geometry. This is why very similar reaction conditions in different works lead to variations in particle sizes up to a factor of 2 (or a factor of 8 in volume), as reviewed in the Results section. Therefore, it is desirable to revisit Sacanna's method [19], but data showing the relationship between particle size and pre-hydrolysed TPM concentration, and how reproducibly specific particle sizes may be obtained in the absence of homogenisation, remains unavailable.

There are also issues to be resolved with the fluorescent labelling of particles. Established methods of dyeing TPM particles with a fluorophore dissolved in DMSO [23] lead to an uneven distribution of dye throughout the batch. This results in a small population of overly bright particles which can saturate the signal in confocal microscopy images, leading to inaccuracy in particle identification.

A further limitation of existing model systems is achieving simultaneous refractive index and density matching. TPM can be refractive index matched with tetralin and trichloroethylene, however the composition that achieves an exact refractive index match between the particle and solvent is not the same as the density matching point. To achieve density matching, the refractive index match must be compromised. This leads to difficulties when studying the dynamics of dense particle suspensions as a function of gravitational length. There are many examples of such studies [28–31]; this issue is particularly acute for studies such as that by Wood *et al.* [32] which require control over density mismatch while retaining a high level of tracking accuracy deep within dense samples.

In this work, we modify and optimise these aspects of TPM particle preparation for 3D confocal microscopy, guiding potential users all the way from TPM monomer to fluorescently labeled, index-matched particles. We revisit the protocol of Sacanna *e*t al. [19] with some modifications, finding that single-step nucleation of droplets in a 'zero-flow' regime gives precise control over target particle sizes within a certain concentration window, provided reagent mixing is swift and that nucleation occurs under quiescent conditions. We also show how exchange of DMSO for a less viscous

solvent improves the distribution of fluorophore throughout a batch of TPM particles. Finally, we introduce a ternary organic solvent mixture for suspending TPM particles which allows a close refractive index match to TPM particles with independent control of density mismatch between particle and solvent.

3.2 Experimental Methods

3.2.1 TPM Droplet Formation

We pre-hydrolyse TPM oil by adding 2 ml TPM to 20 ml 0.5mM HCl. The emulsion was left to stir vigorously for 1 hour after which the solution goes transparent, and we considered all TPM monomers to be fully hydrolysed. We note that hydrolysis in these mildly acidic conditions significantly accelerates the hydrolysis, as widely noted for other silanes [33], while avoiding any significant effect on subsequent steps at higher pH. For reference, existing methods refer to TPM pre-hydrolysis under neutral conditions for 24 hours [20]. The resulting hydrolysed TPM solution (hTPM) was further diluted with 0.5mM HCl in a 150 ml round bottom flask to a target concentration and stirred at 600 rpm for 10 min. Exact quantities of reactants are shown in Table 3.1. Stirring was then stopped and the flask left to settle until contents were stationary. To form TPM droplets, a volume of 0.028% NH_4OH was added swiftly, as one volume, to the flask using a 25 ml plastic pipette (Starlab) and filler. Upon addition of the base, the flask was left to stand for 45 minutes to allow droplet formation to take place. A schematic is shown in Fig 3.1.

In order to reach larger particle diameters, we also briefly document the further addition of hTPM to pre-formed droplets, as performed in previous work [20, 21]. Specifically, we focus on how reproducible the growth path is when a syringe pump is used to add the mildly acidic pre-hydrolysed TPM solution described above at a set rate. The suspension of pre-formed droplets was stirred at 200 rpm under the assumption that further nucleation of particles in the main part of the particle size

0.028% NH_4OH/ ml	25	25	25	25	25	25	25	25
0.5mM HCl/ ml	24	22	22	21	20	19	18	17
hTPM/ ml	1	2	3	4	5	6	7	8
[TPM]/ x10^{-5}M	0.77	1.53	2.30	3.06	3.83	4.59	5.36	6.12

Table 3.1: Quantities of reactants used for initial TPM droplet formation.

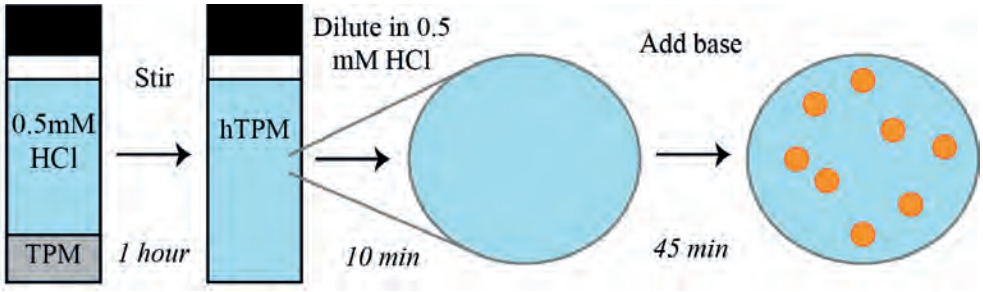

Figure 3.1: Schematic of droplet synthesis using pre-hydrolysed TPM in the absence of flow. Note the sample is only stirred to pre-hydrolyse the TPM; particle formation takes place in quiescent conditions.

population does not occur. The drip rate was kept at 160 μl/min from a 10 ml syringe mounted on syringe pump (PHD 2000 Harvard Apparatus). This rate was low enough to suppress secondary nucleation. The syringe was connected to a PTFE tube inserted into the reaction vessel through a stopper to minimise evaporation of the base.

In both single-step droplet formation and growth experiments, the droplets were crosslinked with AIBN, adding approximately 1 mg per 5 ml emulsion and stirring for 30 min. It should be emphasized that particle formation has finished at this point i.e. all stirring operations in this protocol are applied *after* particle formation has ceased. The suspension was then transferred to an 80 °C oven for 3 hours, tumbling every 30 min to prevent coalescence of droplets. The crosslinked batches were washed by repeated centrifugation and decanting of the supernatant.

3.2.2 Dye Procedure

The procedure for dyeing TPM particles was modified from previous work [23]; the solvent for dye molecules was changed from DMSO to acetone. The mixture was prepared by combining 2 ml of acetone with 2 mg dye (Cyanine3 NHS Ester or RITC) and 2 μl APS before stirring in the dark in a closed 14 ml glass vessel for 24 hours. When the droplets are dyed, 2 ml of 5 wt% F108 was added as described previously to stabilise the droplets [22], letting the solution stir for 45 min. We then added 400 μl of dye solution and the resulting suspension was left to stir for 1 hour before crosslinking.

We also note that uneven dyeing can return if the dye solution was prepared more than a month before use. The linking agent used, APS, reacts with itself over time [21]

causing aggregation of the dye. This can lead to uneven dyeing and brightness when these aggregates are incorporated into particles.

3.2.3 Tuning Density Mismatch of Refractive Index Matched Solution

In previous work, a 60:40 w/w combination of TCE and TTL was used to approximately refractive index and density match crosslinked TPM. PERC has a refractive index, n_f, close to that of crosslinked TPM but a much higher density (see Table 3.2). Thus, addition of PERC to a refractive index matched solution of TPM particles allows tuning of the density mismatch between particle and solution without sacrificing the refractive index match. Note that all organic solvents used in the density and refractive index matching of TPM contain 5wt% OLOA 11000. OLOA 11000 is a charge control agent and stabiliser which has been shown to keep TPM particles stable in non-polar solvents and provide electrostatic screening. A concentration of 5wt% has been shown to keep the particles hard-sphere-like in their interactions in organic solvents [25].

	ρ/g ml^{-1}	n_f
TTL[a]	0.973	1.541
TCE[a]	1.463	1.476
PERC[a]	1.623	1.506
TPM[b]	1.314	1.512

Table 3.2: Refractive index and density of organic solvents used in comparison with crosslinked TPM. [a] Data taken from manufacturer website. [b] Data taken from [21].

To demonstrate the use of this solvent mixture to study density-mismatch dependent behaviour in dense colloidal systems, we prepared fluorescent TPM particles and added a non-fluorescent TPM surface layer using a method outlined in previous work [22]. In brief, fluorescent particles are prepared as described above, the only difference being that they are exposed to a 5%wt Pluronic F108 solution before cross-linking. When additional hTPM is added to these particles, the surfactant induces the formation of well-defined lobes on the surface. On cross-linking these lobes, the particles form fluorescent core-shell 'raspberry' particles. Subsequent additions of hTPM fill in the space between the lobes. A final cross-linking step results in a spherical core-shell particle with a non-fluorescent shell. This increases the separation between fluorescence profiles of adjacent particles in dense suspensions imaged using 3D confocal microscopy [34, 35]. TPM droplets were dyed with a 1 mg/ml Cyanine 3 NHS Ester solution in acetone prepared using the same method described for RITC. Particles were transferred

into solutions of refractive index matching 58:42 w/w TCE:TTL using the solvent transfer method described previously [23]. The resulting suspension was centrifuged to form a pellet and a small volume of supernatant was removed and replaced with PERC. In this way, solutions of varying solvent density but identical TPM volume fraction could be prepared. Suspensions were sealed in a capillary and left to sediment overnight before imaging, focusing on the different diffusion-sedimentation equilibria created for different PERC volume fractions.

Note that all organic solvents contained 5%wt OLOA 11000, a charge control agent and stabilizer which has been shown to keep TPM particles stable and hard-sphere-like in their interactions [25].

3.3 Results and Discussion

3.3.1 TPM Droplet Synthesis

As this synthesis takes place in 'zero-flow' conditions, only two variables affect particle size: pH and concentration of TPM [21, 26]. Given a constant pH, we show that particle diameter can be precisely tuned by varying the concentration of TPM. Fig 3.2a-c) show SEM images of TPM particles nucleated with increasing initial concentrations of TPM; there is a clear increase in particle size. No particles were nucleated below the concentrations shown. Importantly, even though no stirring is carried out, the polydispersity remains low in all cases, below 6% for all batches; size distributions are given in Fig 3.2d).

The average particle diameter as a function of hTPM concentration is given in Fig 3.2e). Firstly, there is a broad consistency with the size of 0.5μm indicated in previous work [20]. For low hTPM concentrations, there is a proportional increase in particle size with concentration. Note that the error bars indicate the standard deviation of mean diameters over three independently produced batches: this suggests that one can aim for a particle size of up to approximately 1.5 μm within a range of $\pm$ 0.1 μm. A small amount of flow is indeed introduced by addition of the base, but by using a pipette and pipette filler we found flow was negligible. This resulted in the same conditions for nucleation between batches and consequently an accurate synthesis of particles of a specific target size within an error of 100 nm. We do note that the last point deviates from this trend with significantly larger error bars. Many factors may contribute to this;

for example, the flask becomes turbid significantly faster than at lower concentrations, increasing the likelihood that the minimal flow created by adding the base affects the nucleation.

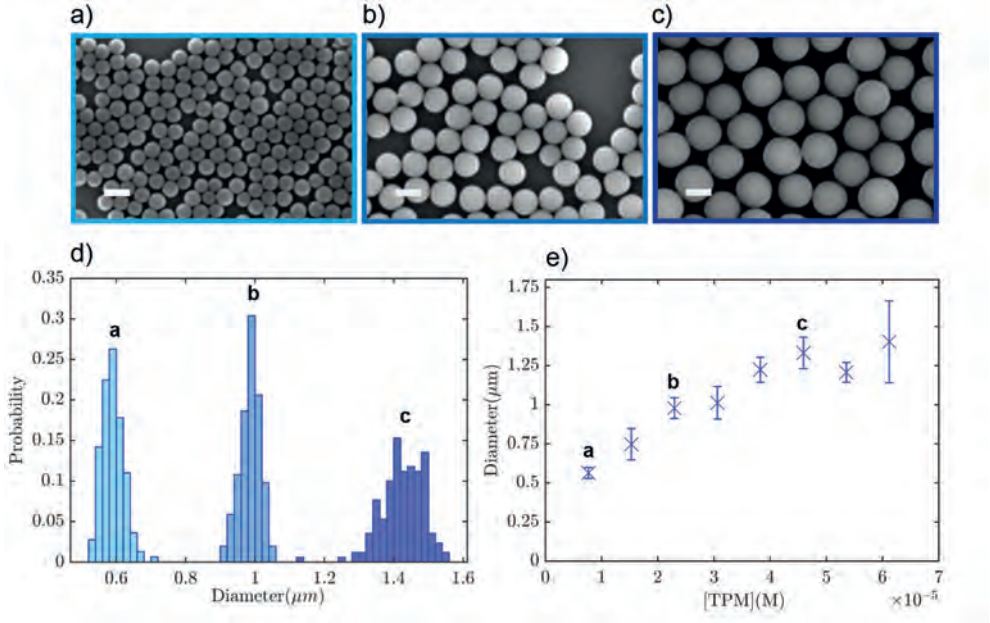

Figure 3.2: SEM images of TPM particles synthesised from different initial concentrations of TPM: 0.77x10^{-5}M a), 2.3 x10^{-5}M b) and 3.83x10^{-5}M (c). Scale bars are 1 μm. (d) shows a histogram of particles sizes for a, b and c. (e) shows a plot of final diameter against concentration of TPM. Mean diameters shown are an average over at least four syntheses; error bars show the standard deviation of the means.

The benefits become more apparent when we compare this to what happens using protocols with stirring. For example, Liu *et al.* and Van Der Wel *et al.* both synthesise particles at a monomer fraction of 20 mM in pH 10.7 conditions, but the resulting particle diameters are 1.3 μm and 0.6 μm respectively. In fact, Middleton *et al.* explicitly demonstrates that stirring rate has a non-monotonic impact on the final particle size. By increasing stirring speed from 500 to 900 min^{-1} resulting particle diameter increases from 1.45 μm to 1.92 μm. However a higher stirring speed of 1100 min^{-1} decreased particle size to 1.75 μm. Even with identical stirring equipment, identical flow fields are difficult to replicate between batches, and thus lead to discrepancies at the same concentration and pH. We propose that by eliminating the need for stirring by using pre-hydrolysed TPM, which is already evenly dispersed throughout the reaction vessel, this method is more reproducible across reaction vessels.

Since reactions can be done in anything from 0.5ml microtubes to large flasks, dozens of syntheses are trivially parallelised.

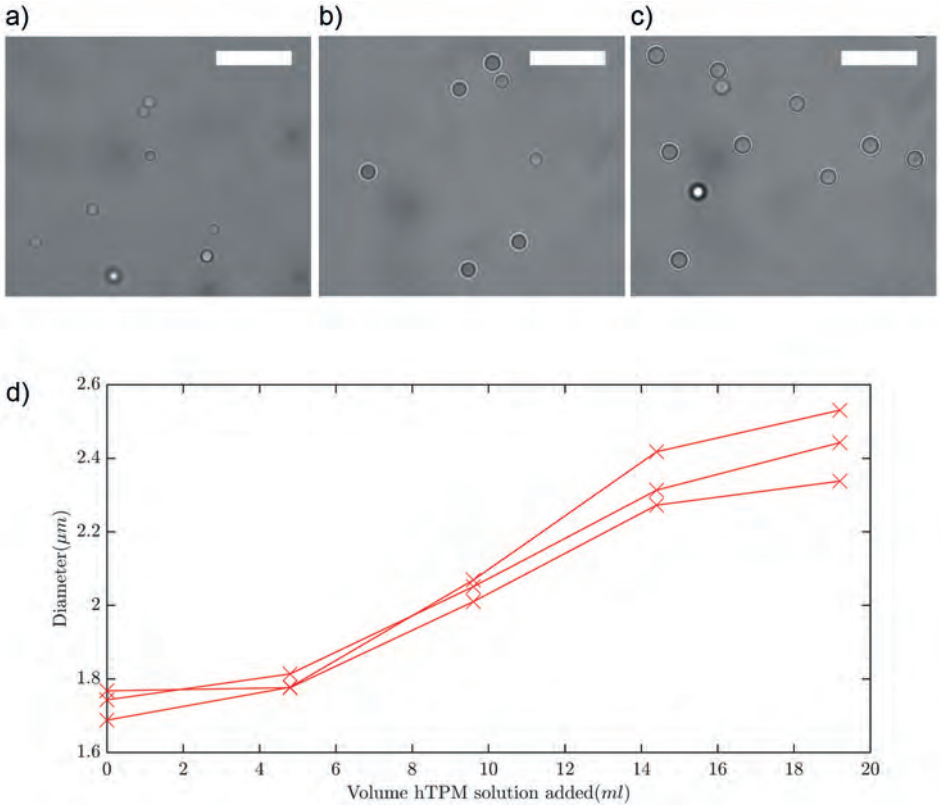

Figure 3.3: (A)-(C) show optical microscope images taken during a droplet growth procedure. Scale bar for all images is 10 μm (D) shows a plot of particle diameter against volume of hTPM added for droplet growth experiments.

Droplet nucleation using pre-hydrolyzed TPM is also drastically faster than in stirred, one-pot syntheses: solutions turn turbid within 1 minute. This is likely a product of the formation mechanism. Though a variety of mechanisms have been proposed for particle formation in similar systems [36], there is a broad consensus that the rate limiting step in this process is the slow hydrolysis of the TPM under basic condition. Sacanna's method bypasses this step by using a pre-hydrolysed TPM, leading to a rapidly developing turbidity [20]. Importantly, to maximise control over nucleated droplet diameter, our data suggests that the best results are obtained when particle nucleation occurs after the residual flows from the mixing process have settled. In the parameter space explored in this work, this corresponds to low TPM

concentrations, when the nucleation is comparatively slower. We also note that the ammonia concentration we use is significantly lower than previous work, again slowing down nucleation enough to see any residual flows dissipate. Though the elucidation of the exact mechanism is beyond the scope of this work, the ease with which particles may be formed in the absence of flow suggest applications to in-situ particle formation in confined geometries given an arbitrary pH modification mechanism.

To produce particles larger than 1.5 μm, a droplet growth procedure was required, as in previous works [20, 21]. Here, we document particle size growth with a set drip rate, with a focus on the reproducibility of the growth trajectory. Using a syringe pump to drip in pre-hydrolysed TPM as described in the Methods, Fig 3.3a-c) show optical microscopy images of droplets during the growth procedure. Note that there is no secondary nucleation or an increase in polydispersity. This is also shown in Fig 3.3d), showing particle diameter as a function of volume of hTPM added. An increase in particle diameter is seen, but polydispersity stays low, below 6%. Slow addition of pre-hydrolysed hTPM ensures the concentration of TPM is even throughout the flask, for even growth of all droplets, but too low for secondary nucleation. Importantly, the polydispersity of the resulting particles remains below the crystallisation threshold [37], making them suitable for studies of colloidal crystallisation. Again, due to the faster incorporation of hTPM compared to TPM oil hydrolysing in-situ, growing particles up to 2.5 μm in diameter only takes 2 hours after initial nucleation. Looking at multiple growth trajectories, we find that independent growths lead to precise, quantitative control over diameter growth using this protocol: the three separate lines indicate independent droplet growths which follow the same path to within ± 0.1 μm. We note that this droplet growth procedure can be performed on any of the initial droplet sizes nucleated under the conditions shown in Fig 3.3. Note that we have chosen a growth rate that suppresses secondary nucleation. If one was aiming for larger droplets in the same amount of time, it is also possible to raise the drip rate. This will induce secondary particle formation: however, this is not a problem, provided that the growth is stopped before the secondaries grow too much and cause issues for separation of the primary particles by centrifugation.

3.3.2 Uniform Dyeing

Most previous protocols to fluorescently dye TPM particles use a pre-labeled fluorophore dissolved in DMSO. Even with stirring, when the dye solution is added to TPM droplets, locally high concentrations of dye result where the dye solution is dripped into the

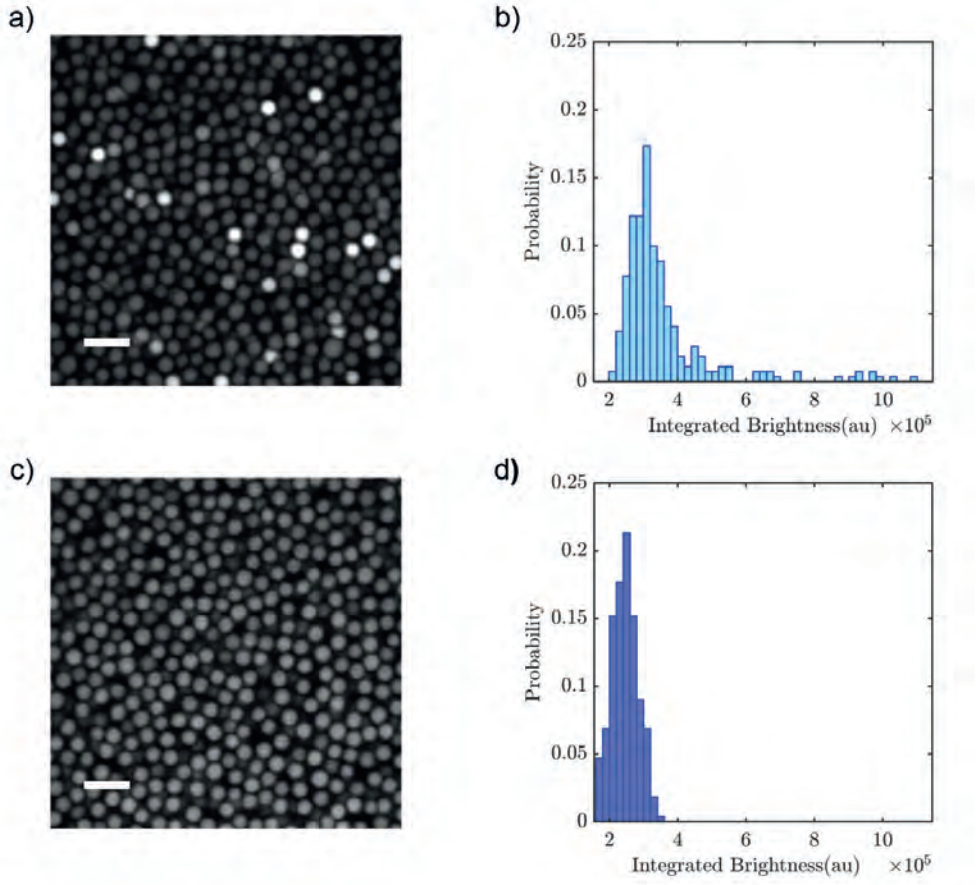

Figure 3.4: 2D fluorescent microscopy images of particles dyed with RITC using a DMSO (A) and acetone (C) dye solution. Scale bar is equal to 5 μm. (B) and (D) shows histograms of integrated brightness for particles dyed with DMSO and acetone dyes respectively.

reaction vessel, producing a small number of very bright particles which can interfere with the fluorescence profile of neighbouring particles. We demonstrate this using a solution of RITC in DMSO, pre-conjugated with APS. Note the noticeably bright particles in Fig 3.4a) and the elongated tail in the distribution of integrated particle brightness in Fig 3.4b). This can be avoided by changing the dye solvent from DMSO to acetone. Fig 3.4c) is visibly more uniform; the distribution of integrated particle brightness in Fig 3.4d) is also clearly mono-modal, with no long tail.

To achieve more uniform transfer of a fluorophore, the organic solvent must disperse quickly and evenly throughout the aqueous reaction media. This ensures there are no points of high concentration of the organic solvent, and therefore the fluorophore. This would generate a local population of overly bright particles as some particles are exposed to a higher concentration of dye during the transfer than others. Similarly to how we use an organic solvent to disperse a fluorophore into an aqueous media, analogous work [38] uses organic solvents to disperse a polymer during nanoprecipitation experiments. By dissolving polymer in solvents of similar miscibility but a higher diffusion coefficient, Beck-Broichsitter *et al* saw a more even dispersion of polymer in the aqueous phase. By selecting acetone, which has a higher diffusion coefficient than DMSO, we can exploit the same effect. Acetone disperses the dye more evenly prior to transfer to TPM droplets resulting in the entire batch of droplets being more evenly dyed.

3.3.3 Tuning of Refractive Index and Density Matching

Finally, we introduce a unique ternary solvent combination for preparing index matched suspensions with varying solvent densities. Previous work [23, 25] describes how TPM microspheres may be approximately refractive index and density matched in a solution of TCE and TTL. Such suspensions may be imaged using confocal microscopy to yield the full internal 3D structure. However, the study of phenomena such as gelation and sedimentation often requires independent adjustment of the density; in a binary solvent mixture, this would be at the sacrifice of index matching. As previously stated, PERC has the same refractive index but a much higher density than both TCE and TTL, and the crosslinked TPM microspheres. Therefore, addition of PERC to a refractive index matched suspension of TPM in TTL and TCE maintains the refractive index match while tuning the density mismatch.

Fig 3.5a) shows 3D confocal microscopy images of a suspension of dyed TPM particles with an additional non-fluorescent shell [22] suspended in 42:58 w/w TTL:TCE, at a particle volume fraction of 30%, left to sediment overnight in a capillary. The particles are 2.4 μm in diameter (see below) and are monodisperse. Two samples of this particle suspension in 42:58 w/w TTL:TCE are then taken; both are taken close to density matching by i) addition of TCE and ii) addition of PERC. We do not fully density match to ensure the formation of a relatively dense suspension at the base, to gauge imaging performance in dense suspensions. Fig 3.5b) shows the particles suspended in a solvent consisting of 85:15 w/w TCE:TTL. Note the decay in signal per particle as we go deeper into the suspension. This is also apparent in the

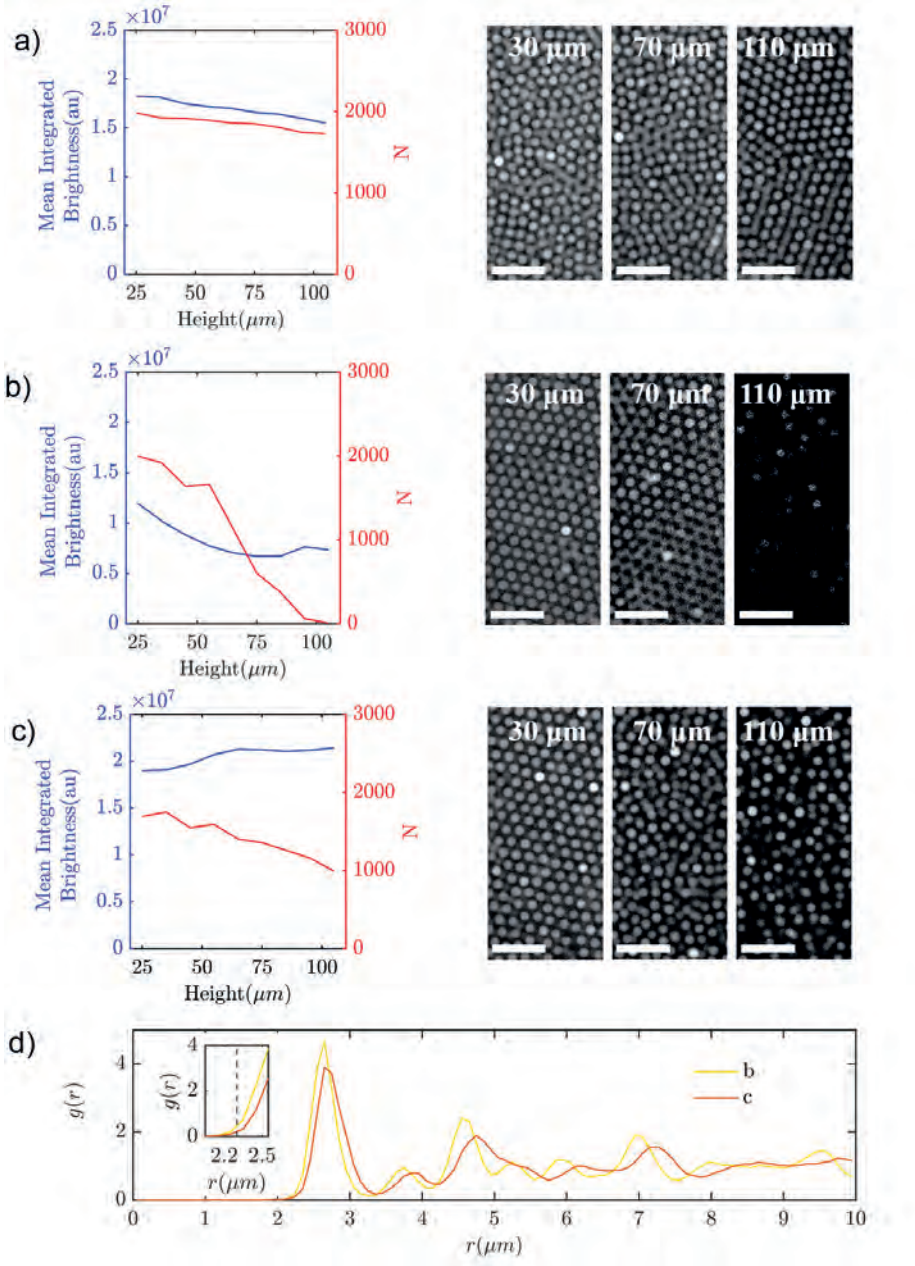

Figure 3.5: Number of particles and mean integrated brightness per particle at different heights within a confocal z-stack through a partially crystalline sediment of TPM spheres in refractive index matching 42:58 TTL:TCE a), in (nearly) density matching 85:15 w/w TCE:TTL b) and (nearly) density matching 45:23:32 w/w PERC:TCE:TTL c). Inserts show xz profile at different heights. Scale bar in all cases is 10 μm. d) is a 3D g(r) of samples b and c, inset shows the g(r) at small r. Dotted line shows the Diameter measure from SEM.

image quality as scan depth increases. This emphatically shows that density matching cannot be achieved in a TCE:TTL binary system without sacrificing the refractive index matching. Fig 3.5c), however, shows the results for the *same* particle suspension with the same solvent density, only now using PERC with an overall composition 45:32:23 w/w PERC:TCE:TTL. The snapshots taken throughout the suspension show minimal apparent decay in brightness. The mean integrated brightness per particle as a function of height corroborate this. Note in particular the change in the number of particles detected, particularly at deep positions: this highlights the possibility that a significant number of particles may have been missed in Fig 3.5b) due to a poor signal-to-noise ratio.

Thus, we can independently tune the density mismatch relative to the particles while maintaining the refractive index matching, something not feasible for a binary system as demonstrated in Fig 3.5b). We emphasise the ease with which one can tune the density mismatch: the suspension can simply be centrifuged to form a pellet and a volume of refractive index matching solvent removed and replaced with PERC. In this way a range of samples of the same refractive index matching but varying density mismatch may be prepared. We also note that no significant change in swelling is observed. Figure 3.5d) shows the g(r) for the close-to-density matched suspensions b and c. We see no clear shift in where the first peak rises (see inset) nor the position of the first peak, indicating minimal change in physical size.

The use of PERC makes it simple to realise a series of solutions with varying density mismatch. For a sedimentation-diffusion equilibria of colloidal spheres, this mismatch is characterised by the characteristic length scale of the decay in number density profile $\rho(h)$, also known as the gravitational length ξ_g. $\rho(h)$ in the dilute limit is described by the barometric formula, $\rho_h = \rho_0 \exp(-\frac{h}{\xi_g})$. Fig 3.6 shows this profile for varying concentrations of PERC on a semilog plot, accompanied by fits to a simple exponential decay. The correspondence is very clear. Note that ξ_g is expressed as

$$\xi_g = \frac{k_{\mathrm{B}}T}{(\Delta\rho)\left(\frac{1}{6}\pi d^3\right)g}, \tag{3.1}$$

where k_BT is the thermal energy, $\Delta\rho$ is the density difference between the particle and the solvent, d is the particle diameter and g is acceleration due to gravity. Thus, a reduced density mismatch leads to a longer ξ_g; this is also reflected in the data. In fact, with an easily prepared series of densities and barometric profiles, we may plot ξ_g

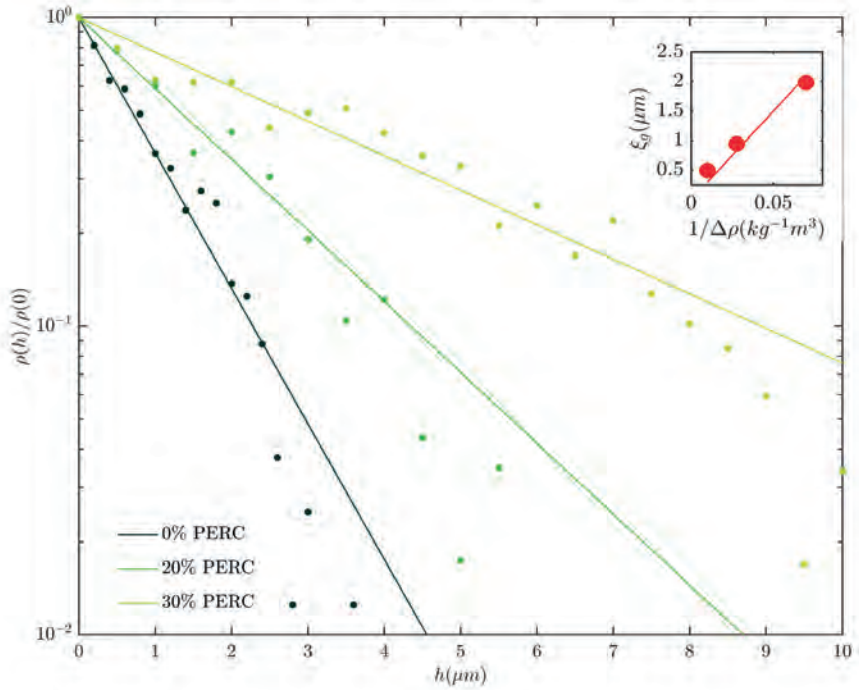

Figure 3.6: Number density $\rho(h)$ against height for particles suspended in a ternary mixture of TCE:TTL:PERC with varying volume fractions of PERC. The solid line is an exponential fit. (inset) Gravitational length vs. inverse of the density difference between the particle and the solvent. The gradient may be used to extract a particle size.

against $1/\Delta\rho$ to estimate the swelled particle size, assuming no drastic changes due to the addition of PERC (inset of Fig 3.6). We find this gives a diameter of 2.4 μm of the particles in solution. This is consistent with the value measured from SEM, 2.3 μm; compared to dried particles in a vacuum, particles are expected to be swelled [23].

The series of solvents used above span Péclet numbers ranging from approximately 0.6 to 2.4. They can be made as arbitrarily low by adding more PERC, or higher by preparing larger particles. Importantly, for particles of a few micrometers, it is evidently simple to probe the regime where the Péclet number is approximately 1, where thermal and advective effects may compete. This illustrates how a ternary system of TCE, TTL and PERC is ideal for studying colloidal suspensions with a controlled Péclet number using confocal microscopy without any compromise in the refractive index matching.

3.4 Conclusion

We have characterised and optimised a simple and reproducible 'zero-flow' protocol for TPM synthesis [19, 20], demonstrating that single-step nucleation can realise precise control over particle size. The method is free of dependencies around reactant flow, and highly reproducible between independent attempts. Droplets may be grown further by adding more pre-hydrolysed TPM at a constant rate, which is consistent with other works [20]. We also present improvements to existing methods of dyeing TPM which improve the distribution of dye over the entire batch of particles. Finally, we introduce a ternary organic solvent mixture which allows independent control of density mismatch within a refractive index matched sample, demonstrated by direct examination of sedimentation-diffusion equilibria. The ease of synthesis, imaging using confocal microscopy and tuning of sedimentation length make this an excellent model system for investigating a wide range of condensed phase behaviour, particularly when particle size distribution [37, 39, 40] or gravity have a significant role to play.

3.5 Supplementary information

3.5.1 Materials

3-(trimethoxysilyl)propyl methacrylate (TPM, ≥97%, Sigma Aldrich), ammonium hydroxide solution (28% vol. NH_3 in H_2O, Alfa Aesar), azobisisobutyronitrile (AIBN, BDH, UK), Cyanine3 NHS Ester (Lumiprobe), Rhodamine B isothiocyanate (RITC, Sigma Aldrich), 3-aminopropyl trimethoxysilane (APS, Sigma Aldrich),acetone (Sigma Aldrich), Pluronic® F-108 (F-108, Sigma Aldrich), trichloroethylene (TCE, ≥99.5%, Sigma Aldrich), 1,2,3,4-tetrahydronaphthalene (TTL, anhydrous, 99%, Sigma Aldrich) and tetrachloroethylene (PERC, 99%, Alfa Aesar) were used as received. A polyisobutylene succinic anhydride stabilizer, OLOA 11000, was provided by Eric Dufresne and Azelis. Double-distilled water was sourced from a Millipore Direct-Q 3 ultrapure water unit.

3.5.2 Imaging Methods

All particles were sized by Scanning Electron Microscopy (SEM). Particles were dried on a silicon chip then sputter coated with platinum using a SC7620 sputter coated (Quorum Technologies, UK) before imaging with a JSM-G1010LV SEM (JEOL, Japan) using an acceleration voltage of 20kV. Images were analyzed using a circle finding algorithm within Matlab. At least 100 particles were imaged to obtain the mean diameter and polydispersity.

Confocal imaging was carried out on an Olympic 1X73 microscope equipped with a Thorlabs confocal 12kHz resonant point scanner, a 532nm laser, and standard FITC/Rhodamine filter cube. All measurements used a 60x Olympus Plan Achromatic oil immersion objective. Integrated particle brightness was calculated using a widely used particle identification algorithm [41].

3.5.3 Acknowledgments

R. A. Crothers and N. H. P. carried out the experimental work in this chapter. We thank B. van der Meer and T. Yanagishima for useful discussions.

3.6 Bibliography

[1] V. W. A. De Villeneuve, R. P. A Dullens, D. G. A. L. Aarts, E. Groeneveld, J. H. Scherff, W. K. Kegel, and H. N.W. Lekkerkerker. Colloidal hard-sphere crystal growth frustrated by large spherical impurities. *Science*, 309:1231–1233, 2005.

[2] T Palberg. Crystallization kinetics of colloidal model suspensions: recent achievements and new perspectives. *J. Phys. Condens. Matter*, 26(33):333101, 2014.

[3] Y. Chen, Z. Yao, S. Tang, H. Tong, T. Yanagishima, H. Tanaka, and P. Tan. Morphology selection kinetics of crystallization in a sphere. *Nat. Phys.*, 17(1):121–127, 2021.

[4] V. Trappe and P. Sandkühler. Colloidal gels - low-density disordered solid-like states. *Curr. Opin. Colloid Interface Sci.*, 8:494–500, 2004.

[5] S. Buzzaccaro, R. Rusconi, and R. Piazza. "sticky" hard spheres: Equation of state, phase diagram, and metastable gels. *Phys. Rev. E*, 99:098301, 2007.

[6] P J Lu, E Zaccarelli, F Ciulla, A. B. Schofield, F Sciortino, and D. A. Weitz. Gelation of particles with short-range attraction. *Nature*, 453(7194):499–503, 2008.

[7] H. Tsurusawa, M. Leocmach, J. Russo, and H. Tanaka. Direct link between mechanical stability in gels and percolation of isostatic particles. *Sci. Adv.*, 5(5):eaav609, 2019.

[8] P. N. Pusey, W. van Megen, S. M. Underwood, P. Bartlett, and R. H. Ottewill. Colloidal fluids, crystals and glasses. *Physica A*, 176(1):16–27, 1991.

[9] N. Simeonova, R. P. A. Dullens, D. G .A. L. Aarts, V. de Villeneuve, H. Lekkerkerker, and W. K. Kegel. Devitrification of colloidal glasses in real space. *Phys. Rev. E*, 73(4):041401, 2006.

[10] G. L. Hunter and E. R. Weeks. The physics of the colloidal glass transition. *Rep. Prog. Phys*, 75:066501, 2012.

[11] J. E. Hallett, F. Turci, and C. P. Royall. Local structure in deeply supercooled liquids exhibits growing lengthscales and dynamical correlations. *Nat. Commun.*, 9(1):3272, 2018.

[12] W. K. Kegel. Direct observation of dynamical heterogeneities in colloidal hard-sphere suspensions. *Science*, 287:290–293, 2000.

[13] V. Prasad, D. Semwogerere, and E. R Weeks. Confocal microscopy of colloids. *J. Phys. Condens. Matter*, 19(11):113102, 2007.

[14] G. Bosma, C. Pathmamanoharan, E. H. A. De Hoog, W. K. Kegel, A. van Blaaderen, and H. N.W. Lekkerkerker. Preparation of monodisperse, fluorescent pmma-latex colloids by dispersion polymerization. *J. Colloid Interface Sci.*, 245:292–300, 2002.

[15] A. van Blaaderen and P. Wiltzius. Real-space structure of colloidal hard-sphere glasses. *Science*, 270:1177–1179, 1995.

[16] P. J. Yunker, K. Chen, M. D. Gratale, M. A. Lohr, T. Still, and A. G. Yodh. Physics in ordered and disordered colloidal matter composed of poly(N-isopropylacrylamide) microgel particles. *Rep. Prog. Phys*, 77(5):056601, 2014.

[17] M. A. Rutgers, J. H. Dunsmuir, J-Z. Xue, W. B. Russel, and P. M. Chaikin. Measurement of the hard-sphere equation of state using screened charged polystyrene colloids. *Phys. Rev. B*, 53(9):5043–5046, 1996.

[18] P. J. Lu and D. A. Weitz. Colloidal Particles: Crystals, Glasses, and Gels. *Annu. Rev. Condens. Matt. Phys.*, 4(1):217–233, 2013.

[19] S. Sacanna, W. T.M. Irvine, P. M. Chaikin, and D. J. Pine. Lock and key colloids. *Nature*, 464:575–578, 2010.

[20] S. Sacanna, W. T. M. Irvine, L. Rossi, and D. J. Pine. Lock and key colloids through polymerization-induced buckling of monodisperse silicon oil droplets. *Soft Matter*, 7(5):1631–1634, 2011.

[21] C. van Der Wel, R. K. Bhan, R. W. Verweij, H. C. Frijters, Z. Gong, A. D. Hollingsworth, S. Sacanna, and D. J. Kraft. Preparation of colloidal organosilica spheres through spontaneous emulsification. *Langmuir*, 33:8174—-8180, 2017.

[22] Y. Liu, K. V. Edmond, A. Curran, C. Bryant, B. Peng, D. G.A.L. Aarts, S. Sacanna, and R. P A Dullens. Core–shell particles for simultaneous 3d imaging and optical tweezing in dense colloidal materials. *Adv. Mater.*, 28:8001–8006, 2016.

[23] Yanyan L., T. Yanagishima, A. Curran, K. V. Edmond, S. Sacanna, and R. P. A. Dullens. Colloidal organosilica spheres for three-dimensional confocal microscopy. *Langmuir*, 35:7962–7969, 2019.

[24] J. Opdam, R. Tuinier, T. Hueckel, T. J. Snoeren, and S. Sacanna. Selective colloidal bonds via polymer-mediated interactions. *Soft Matter*, 16:7438–7446, 2020.

[25] T. Yanagishima, Y. Liu, H. Tanaka, and R. P. A. Dullens. Particle-level visualization of hydrodynamic and frictional couplings in dense suspensions of spherical colloids. *Phys. Rev. X*, 11:021056, 2021.

[26] C. Middleton, M. D. Hannel, A. D. Hollingsworth, D. J. Pine, and D. G. Grier. Optimizing the synthesis of monodisperse colloidal spheres using holographic particle characterization. *Langmuir*, 35:6602—-6609, 2019.

[27] D. Neibloom, M. A. Bevan, and J. Frechette. Surfactant-stabilized spontaneous 3-(trimethoxysilyl) propyl methacrylate nanoemulsions. *Langmuir*, 36:284–292, 2020.

[28] Z. Cheng, J. Zhu, W. B. Russel, W. V. Meyer, and P. M. Chaikin. Colloidal hard-sphere crystallization kinetics in microgravity and normal gravity. *Appl. Opt.*, 40(24):4146–4151, 2001.

[29] Ni. Simeonova and W. K. Kegel. Gravity-Induced Aging in Glasses of Colloidal Hard Spheres. *Phys. Rev. Lett.*, 93(3):035701, 2004.

[30] J. M. Kim, J. Fang, A. P. R. Eberle, R. Castañeda-Priego, and N. J. Wagner. Gel transition in adhesive hard-sphere colloidal dispersions: The role of gravitational effects. *Phys. Rev. Lett.*, 110(20):208302, 2013.

[31] R. Harich, T. W. Blythe, M. Hermes, E. Zaccarelli, A. J. Sederman, L. F. Gladden, and W. C.K. Poon. Gravitational collapse of depletion-induced colloidal gels. *Soft Matter*, 12(19):4300–4308, 2016.

[32] Nicholas W., John R., Francesco T., and C. P. Royall. Coupling of sedimentation and liquid structure: Influence on hard sphere nucleation. *J. Chem. Phys.*, 149, 2018.

[33] G. T. Hermanson. *Bioconjugate Techniques*. Elsevier, 2nd edition, 2013.

[34] A. van Blaaderen, A. Imhof, A. Vrij, and W. Hage. Three-Dimensional Imaging of Submicrometer Colloidal Particles in Concentrated Suspensions Using Confocal Scanning Laser Microscopy. *Langmuir*, 8(6):1514–1517, 1992.

[35] R. P. A. Dullens, M. Claesson, D. Derks, A. van Blaaderen, and W. K. Kegel. Monodisperse core-shell poly (methyl methacrylate) latex colloids. *Langmuir*, 19(15):5963–5966, 2003.

[36] C. B. Whitehead, S. Özkar, and R. G. Finke. LaMer's 1950 model of particle formation: A review and critical analysis of its classical nucleation and fluctuation theory basis, of competing models and mechanisms for phase-changes and particle formation, and then of its application to silver halide, semiconductor, metal, and metal-oxide nanoparticles. *Mater. Adv.*, 2(1):186–235, 2021.

[37] P. N. Pusey. Effect of polydispersity on the crystallization of hard spherical colloids. *J. Phys. France*, 48:709–712, 1987.

[38] M. Beck-Broichsitter, E. Rytting, T. Lebhardt, X. Wang, and T. Kissel. Preparation of nanoparticles by solvent displacement for drug delivery: A shift in the " ouzo region" upon drug loading. *Eur. J. Pharm. Sci.*, 41:244–253, 2010.

[39] H. J. Schöpe, G. Bryant, and W. van Megen. Effect of polydispersity on the crystallization kinetics of suspensions of colloidal hard spheres when approaching the glass transition. *J. Chem. Phys.*, 127(8):084505, 2007.

[40] C. P. Royall, W. C.K. Poon, and E. R. Weeks. In search of colloidal hard spheres. *Soft Matter*, 9:17–27, 2013.

[41] J. C. Crocker and D. G. Grier. Methods of Digital Video Microscopy for Colloidal Studies. *J. Colloid Interface Sci.*, 179(1):298–310, 1996.

Chapter 4

Direct Observation of Heterogeneous Rotational Dynamics in Dense Colloidal Suspensions

The onset of heterogenous translational dynamics is a hallmark of glassy dynamics in dense colloidal suspensions. Whether the same is true for rotational dynamics has not been fully explored. To fully investigate whether rotational dynamics become heterogeneous in dense suspensions the dynamics of all particles must be observable. In this study we utilise the recently developed 'OCULI' particle, which allows for measurement of translational *and* rotational dynamics of all particles within a sample, to investigate the nature of the rotational dynamics of colloidal particles within a dense, amorphous suspension. We reveal that both translational and rotational dynamics are heterogeneous in such a system, but in opposite ways. At high packing fractions, translational dynamics develop a fast subpopulation while rotational dynamics develop a slow subpopulation. Furthermore, we find this rotationally slow subpopulation forms small but 'string-like' clusters. Finally, we correlate the degree of rotational arrest with the properties of the local environment at the single-particle level.

4.1 Introduction

The complexities of glass forming materials have fascinated the condensed matter community for decades [1–3]. One aspect of interest is in the emergence of heterogeneous dynamics as the glass transition is approached [4–10]. A dense glass forming material has a disordered structure leading to a large variety in the local environments experienced by each particle. Some particles are more confined, or caged, by neighbouring particles while others experience less caging and are more mobile, able to break out of a cage and enter a new one. Therefore the dynamics of the system are heterogenous as the particles can be divided into a slow bulk population, particles unable to undergo cage breaking, and a fast subpopulation, particles able to cage break. Over time each particle undergoes enough cage-breaking steps that the dynamics of the system become diffusive at long times, however the timeframe for this increases rapidly as the glass transition is approached [11]. The onset of dynamic heterogeneity is a hallmark of dense systems such as polymer melts [4–6], molecular glasses [7, 8] and granular suspensions [12, 13].

Colloidal systems give a unique insight into particle behaviour in dense suspensions as they exhibit the same phase behaviour as atoms and molecules albeit at length and timescales that can be observed on an optical microscope [14, 15]. Dynamic heterogeneity was first investigated in 2D colloidal systems where caged and cage breaking motions could be directly observed and correlated to a non-Gaussian distribution of their displacements for a given time interval [16, 17]. Later work extended this to 3D and again correlated the heterogenous dynamics to a subpopulation of fast particles undergoing cage-breaking behaviour [9, 10]. However, in previous studies only half the story of dynamic heterogeneity is visible as only the *translational* dynamics could be observed. Few experimental systems exist that allow a similar direct observation of *rotational* dynamics, in particular for isotropic particles [18–22]. This is simply due to the non-trivial problem of capturing the rotational dynamics of spherical particles.

Studies that examine the rotational dynamics in dense, crystalline or glassy, suspensions utilise tracer particles which have been altered in either shape [21, 22], or optical properties [18–20] to allow for the observation of the rotational dynamics. Some studies use isotropic tracer particles; spherical Janus particles seeded in a supercooled host system of silica microspheres [19] or spherical PMMA tracers with two cores in a crystalline [18] or glassy [20] system. In these studies, as the volume fraction, ϕ,

increases, translational dynamics are slowed down to a greater extent than the rotational dynamics, which remain diffusive at all ϕ examined. Furthermore in the crystalline system, the dynamics at short and long timescales, at both dilute and concentrated ϕ, are demonstrated to be Gaussian. Studies with anisotropic tracer particles [21, 22] see a more dramatic slow down of rotational dynamics than translational dynamics. Yet, still the rotational dynamics are shown again to be Gaussian at $\phi = 0.39$ and $\phi = 0.54$, at both short and long time intervals [21]. The consistent argument that emerges across these studies is that as ϕ increases rotational dynamics are slowed, much more so for an anisotropic particle, but the dynamics of this slowdown are Gaussian regardless of tracer particle shape. However, all previous approaches have not observed the rotational dynamics of *the whole population*. To truly investigate whether the slowdown of rotational dynamics in dense colloidal suspensions display a similar heterogeneity to translational dynamics the rotational dynamics of *all* the particles must be studied.

The recently developed 'Off-Centre-Under-Laser-Illumination' (OCULI) particle allows simultaneous recording of the translational and rotational dynamics of *every particle* within the system [23]. Here we utilise this particle system to directly observe the translational and rotational dynamics of OCULI particles in a dense, amorphous sedimentation-diffusion equilibrium. For the first time we can probe the nature of the translational and rotational dynamics in dense suspensions for all particles in the system.

4.2 Experimental System

OCULI particles of diameter 3.10μm are synthesised by following the synthesis protocol developed in ref [23], a full description is provided in Supplementary Information, SI, (4.6.2). The particles are refractive index matched in a binary mixture of tetralin and trichloroethylene (42:58 w/w) at an initial overall $\phi = 0.3$ [24]. The particle suspension was sealed inside a capillary and left to sediment overnight. The resulting sedimentation-diffusion equilibrium is illustrated by Fig 4.1. The density profile as a function of height is shown in Fig 4.1a) which shows very small variation in ϕ over the majority of the sample followed by a steep decay at the top. We characterise this steep decay by calculating the gravitational length, $\xi_g = \frac{3k_BT}{4\pi R^3 g\Delta\rho}$, where $\Delta\rho$ is density difference between the particle and the solvent. We measure a solvent density of $1.16gcm^{-3}$ which for TPM particles of density $1.31gcm^{-3}$ results in a ξ_g of 0.18μm. The relatively large density mismatch between particle and solvent causes

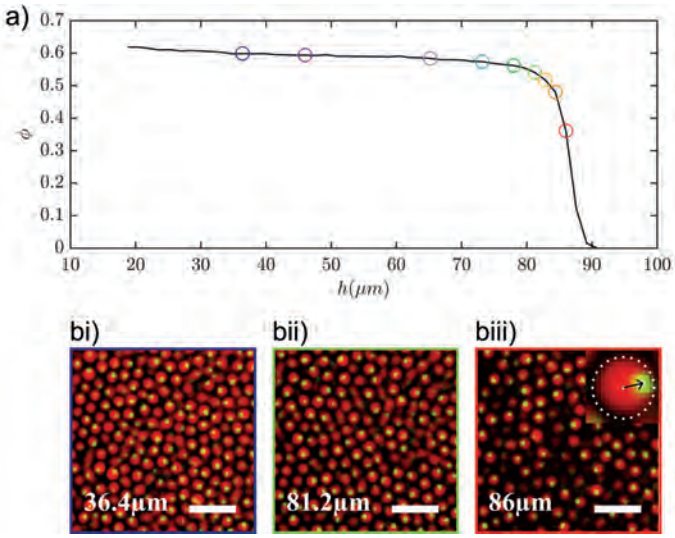

Figure 4.1: a) Density profile throughout sediment of OCULI particles in 42:58 w/w Tetralin:trichloroethylene. bi-iii) Confocal images at various heights within sample. Scale bar in each case is equal to 10μm. Inset shows how independent tracking of the body and eye allows the observation of the orientation of each particle.

rapid sedimentation which traps the sediment in a amorphous structure. This can be directly observed in the confocal images at various heights within the sample as seen in Fig 4.1b). No long range order is observable at the bottom of the sample and we see ϕ decay rapidly at the top of the sample to the fluid phase. Therefore, by imaging at different heights within the sample we can observe the translational and rotational dynamics of *every* particle in a dense, amorphous suspension.

4.3 Ensemble Averaged Translational and Rotational Dynamics

First, we examine the ensemble averaged translational and rotational dynamics at different ϕ by evaluating the mean squared displacement (MSD) and mean squared angular displacement (MSAD). Both the MSD and MSAD are calculated directly from particle coordinates using Eq 4.1 where ν is the translational displacement, r, or rotational displacement, θ, respectively

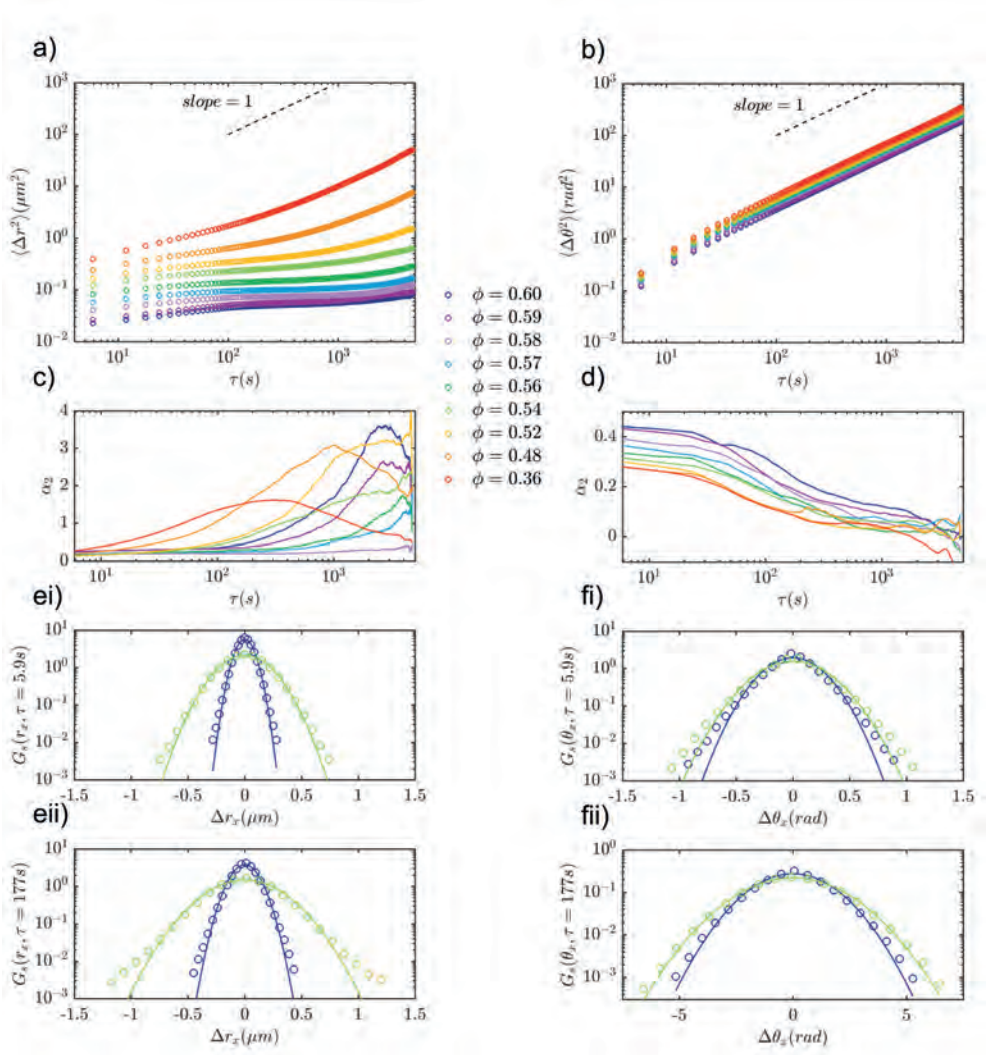

Figure 4.2: a) MSD for different ϕ recorded at different heights within the sample. b) MSAD for different ϕ, rotational displacement has been calculated following the method established in [25]. c) α_2 calculated from translational displacement in x. d) α_2 calculated from rotational displacement in x. e) G_s calculated from translational displacement in x at i) $\tau = 5.9s$ and ii) $\tau = 177s$ for $\phi = 0.54$ and $\phi = 0.60$. G_s calculated directly from Eq 4.2 is plotted as points while the predication from the Gaussian approximation, Eq 4.3, is shown as a solid line. f) G_s calculated from rotational displacement in x at i) $\tau = 5.9s$ and ii) $\tau = 177s$ for $\phi = 0.54$ and $\phi = 0.60$. G_s calculated directly from Eq 4.2 is plotted as points while the predication from the Gaussian approximation, Eq 4.3, is shown as a solid line.

$$\langle \Delta\nu^2(\tau)\rangle = \frac{1}{N}\sum_{i=1}^{N}\langle[\nu_i(\tau)^2 - \nu_i(0)^2]\rangle \qquad \nu = r \text{ or } \theta. \tag{4.1}$$

Extraction of the rotational dynamics uses the method established in Ref. [25], a more detailed description is included in the SI 4.6.7.

Fig 4.2 shows an overview of the dynamics of particles throughout the sediment. Fig 4.2a) shows the ensemble averaged MSD for different ϕ recorded at different heights within the sediment. As ϕ increases a transient plateau is observable in the MSD due to the onset of caging, which occurs at earlier τ for higher ϕ. For low ϕ we see an increase in the MSD at long τ as more particles begin to undergo cage breaking and diffusive behaviour begins to return. At high ϕ we see the plateau remains for the duration of the experimental timeframe as the particles are mainly localised in position and the timeframe for cage breaking exceeds the experimental window.

Strikingly, the MSAD, shown in Fig 4.2 b), shows a direct contrast to the MSD. No visible plateau is observable at any ϕ and all sampled ϕ appear to display diffusive rotational dynamics at all times. Only a small slowdown is observable in the MSAD with increasing ϕ, as has been observed in previous studies with tracer particles [18, 19, 21]. Therefore, at the ensemble averaged level, although both translational and rotational dynamics exhibit some degree of slow down, the translational dynamics are significantly more impacted by caging.

Next, we characterise the heterogeneity of both the translational and rotational dynamics using the non-Gaussian parameter, α_2 which is defined as,

$$\alpha_2(\tau) = \frac{\langle \Delta\nu_x^4(\tau)\rangle}{3\langle \Delta\nu_x^2(\tau)\rangle^2} - 1 \qquad \nu = r_x \text{ or } \theta_x. \tag{4.2}$$

For a system where the dynamics are Gaussian, α_2 is 0, deviations from this quantify the degree of heterogeneity. The nature of the heterogeneous dynamics, whether a fast subpopulation is present, can be observed in the self-part of the van Hove function, G_s, defined as,

$$G_s(\nu_x, \tau) = \left\langle \frac{1}{N} \sum_{i=1}^{N} \delta[\nu_x - \nu_{x,i}(\tau) + \nu_{x,i}(0)] \right\rangle \qquad \nu = r_x \text{ or } \theta_x. \tag{4.3}$$

This is the normalised probability density function for the particle displacements evaluated at the time interval τ. Heterogeneous dynamics can be observed as deviation between G_s calculated directly from particle coordinates, (Eq 4.3), and from what is predicated by the Gaussian approximation [11, 26, 27],

$$G_s(\nu_x \tau) = \left(\frac{1}{2\pi \langle \Delta\nu_x^2(\tau) \rangle} \right)^{\frac{1}{2}} \exp\left(-\frac{\nu_x^2}{2\langle \Delta\nu_x^2(\tau) \rangle} \right) \qquad \nu = r_x \text{ or } \theta_x. \tag{4.4}$$

Again by substituting r_x or θ_x for ν_x we can define G_s, from both Eq 4.3 and Eq 4.4, in terms of both translational and rotational dynamics.

Fig 4.2c) shows α_2 calculated for translational dynamics. For all ϕ, α_2 begins close to zero and increases slowly to a maximum as particles begin to undergo caging and the dynamics of the system become more heterogeneous. At low ϕ we see α_2 return to 0 as all particles undergo enough cage-breaking events for the dynamics to become Gaussian at long τ. For higher ϕ we see the peak in α_2 appear at longer τ as the timeframe for cage-breaking increases. At higher ϕ, α_2 is still non-zero at the end of the experimental timeframe, indicative of persistent heterogeneous dynamics. The G_s for translational dynamics is shown in Fig 4.2e) for a τ of i) 5.9s ($\tau < \tau_T$) and ii) 177s ($\tau >> \tau_T$), where τ_T is the Brownian time (see SI 4.6.5). At short τ only very small deviations between the G_s calculated from particle coordinates, shown as points, and the G_s predicted from the Gaussian approximation, shown as a solid line are observable for both $\phi = 0.54$ and $\phi = 0.60$. At a longer τ we see the non-Gaussian behaviour for $\phi = 0.54$ increase as more particles begin to cage-break and deviations from the Gaussian prediction are seen as tails either side of the solid line due to the fast subpopulation. At long τ, the G_s for $\phi = 0.60$ broadens slightly and again small deviations from non-Gaussian behaviour can be seen in the tails of the distribution due to a persistent dynamic heterogeneity.

Now we turn to α_2 for the rotational dynamics. Fig 4.2d) shows α_2 calculated for rotational dynamics which displays a remarkably different shape to Fig 4.2c). For rotational dynamics α_2 begins at a maximum value and shows a prolonged decay, despite the MSAD being diffusive at all times. Notably the maximum value of α_2 at the start

as well as the timescale over which α_2 decays increases with increasing ϕ. The reason for this decay can be found in the G_s, shown, for rotational dynamics, in Fig 4.2f) for $\phi = 0.54$ and $\phi = 0.60$. At short τ, in Fig 4.2fi) we see G_s for $\phi = 0.54$ and $\phi = 0.60$ are relatively indistinguishable as both display a distinctly non-Gaussian shape. We can see deviations in G_s from Gaussian behaviour in both the tails and, notably, in the centre. At longer τ, we see that for $\phi = 0.54$ G_s is well described by the Gaussian approximation, including in the tails and in the centre. Notably for $\phi = 0.60$ there are still deviations in G_s from the Gaussian approximation in both the tails and in the centre. Therefore, it is evident that rotational dynamics display some degree of heterogeneity that results in a long decay in α_2 and deviations in G_s from Gaussian behaviour, but is not observable from the MSAD.

4.4 Single-Particle Translational and Rotational Dynamics

The OCULI system gives us unique access to the translational and rotational dynamics at a single-particle level. In Fig 4.3, we therefore examine the *single-particle* MSDs and MSADs for $\phi = 0.54$, 0.57 and 0.60. First, in Fig 4.3a) we show the single-particle MSDs, $\langle \Delta r_i^2 \rangle$. On first inspection for all ϕ the ensemble average $\langle \Delta r^2 \rangle$ appears to be situated towards the centre of the distribution of $\langle \Delta r_i^2 \rangle$. However, if we examine the distribution of $\langle \Delta r_i^2 \rangle$ at $\tau = 100.3$s, shown is Fig 4.3bi) we see that for all ϕ the ensemble averaged mean sits to the right of the peak of the distribution. Furthermore, all the distributions exhibit a skew towards larger $\langle \Delta r_i^2 \rangle$ and therefore faster dynamics. Due to the different spread in the distribution we re-examine this data on a log scale as shown in Fig 4.3bii). Here the same features are evident; as ϕ increases the distribution becomes more skewed towards the right, towards faster dynamics, due to the development of a fast-subpopulation. For higher ϕ, the ensemble averaged mean, shown as a dash line, is also at a higher value than the peak of the distribution, creating an offset. This can be explained by considering that the fast subpopulation will have a large impact on the ensemble averaged $\langle \Delta r^2 \rangle$ as a handful of large numbers will skew a mean squared average towards a larger value.

Fig 4.3c) shows the single-particle MSADs, $\langle \Delta \theta_i^2 \rangle$, where a striking contrast to translational dynamics is seen. As ϕ increases, although there is little change in the ensemble averaged mean, a subpopulation of particles develops that is rotationally

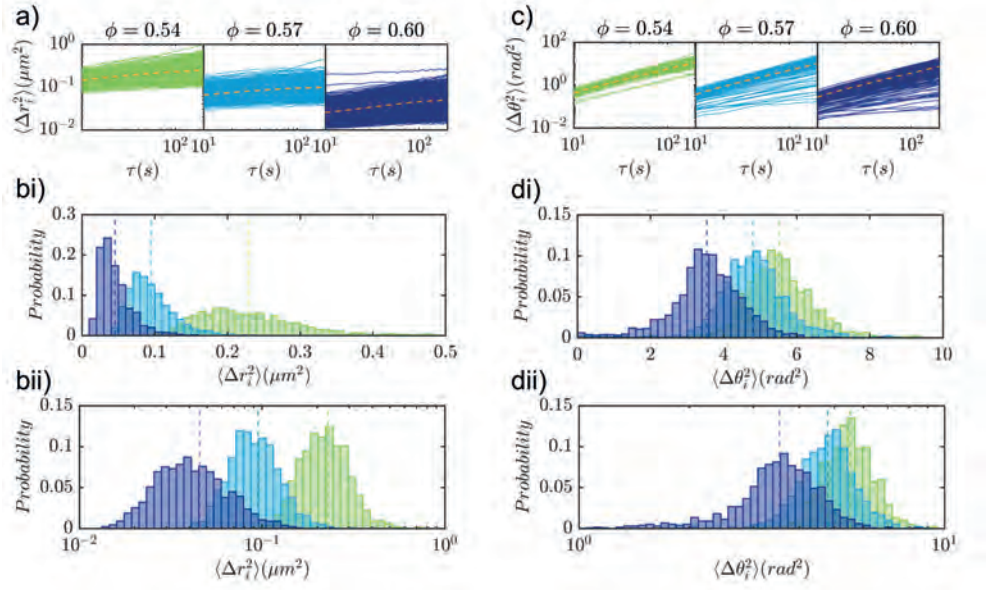

Figure 4.3: a) Single-particle MSDs $\langle \Delta r_i^2 \rangle$ for $\phi = 0.54$, 0.57 and 0.60. b) Distribution of $\langle \Delta r_i^2 \rangle$ calculated at $\tau = 100.3$s for $\phi = 0.54$, 0.57 and 0.60 on a i) linear and ii) log scale. The ensemble averaged $\langle \Delta r^2 \rangle$ for each ϕ is shown as a dashed line in panels i) and ii). a) Single-particle MSADs $\langle \Delta \theta_i^2 \rangle$ for $\phi = 0.54$, 0.57 and 0.60. b) Distribution of $\langle \Delta \theta_i^2 \rangle$ calculated at $\tau = 100.3$s for $\phi = 0.54$, 0.57 and 0.60 on a i) linear and ii) log scale. The ensemble averaged $\langle \Delta \theta^2 \rangle$ for each ϕ is shown as a dashed line in panels i) and ii).

slower than the bulk population. This is further illustrated in Fig 4.3di) which shows the distribution of $\langle \Delta \theta_i^2 \rangle$ at $\tau = 100.3s$. From $\phi = 0.57$ to $\phi = 0.60$ we observe that the distribution develops a distinct tail towards smaller $\langle \Delta \theta_i^2 \rangle$ and therefore slower dynamics. Changing to a log scale, as shown in Fig 4.3dii) this becomes more evident. Therefore as ϕ increases *both* translational and rotational dynamics become heterogeneous but in opposite ways. Translational dynamics develop a *slow* bulk population and *fast* subpopulation while rotational dynamics develop a *fast* bulk population and *slow* subpopulation. Again, a small offset between the peak of the distribution and the ensemble averaged mean is observable where the ensemble average, shown as a dashed line, is to the left of the peak of the distribution. Notably, this is in the opposite direction to the off-set seen for translational dynamics and smaller in magnitude. This can be rationalised by considering that a slow subpopulation will have a smaller impact on a mean squared displacement than fast dynamics as, a handful of small numbers will results in a smaller skew to an mean squared averaged. This also

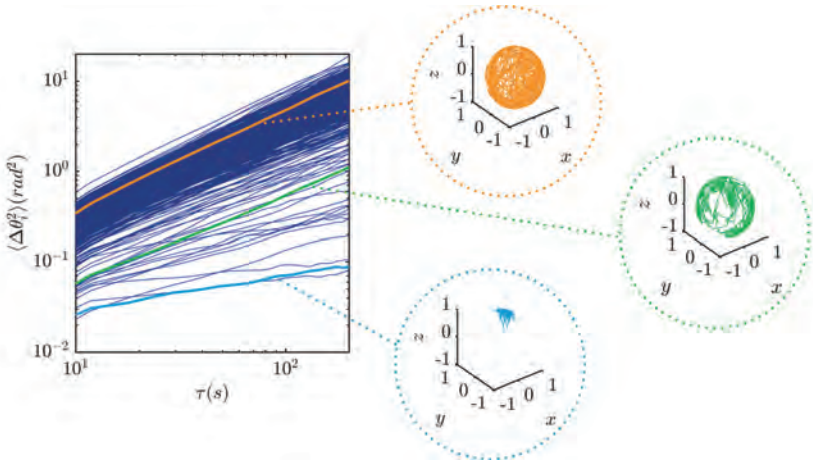

Figure 4.4: Single-particle MSADs for $\phi = 0.60$ with example rotational trajectories.

explains why little change is seen in the ensemble averaged MSAD.

Further insight into the heterogeneity of rotational dynamics can be obtained by extracting the rotational trajectories at the highest volume fraction examined, $\phi = 0.60$. Fig 4.4 shows the MSAD of single particles, with three distinct 'types' of rotational behaviours distinguishable varying from rotationally free, to partially arrested, to fully arrested. This type of behaviour has been observed in the OCULI system in both a partially crystalline sediment as well as within a gel [23, 28]. It has been rationalised that this type of rotational arrest arises from interparticle friction between neighbouring particles. If we follow this rational this suggests that rotationally slow particles should display a degree of clustering.

We therefore probe the spatial distribution of the rotationally slow subpopulation. To this end, we examine a section at the bottom of the sediment between 30 and 50μm, across which ϕ varies only very slowly with height: between these heights ϕ varies less then 1% from 0.60. We define the rotationally slow subpopulation as the rotationally slowest 10%, a full description of how this is defined is provided in SI 4.6.8. Fig 4.5a) shows a 3D reconstruction of the 10% rotationally slowest particles. The particles are coloured by their rotational mobility. We can observe a degree of clustering of particles of different rotational mobility. Notably, the most arrested particles, shown in red, seem to be more commonly found within clusters. We next examine the cluster size distribution of the 10% rotationally slowest particles, shown in

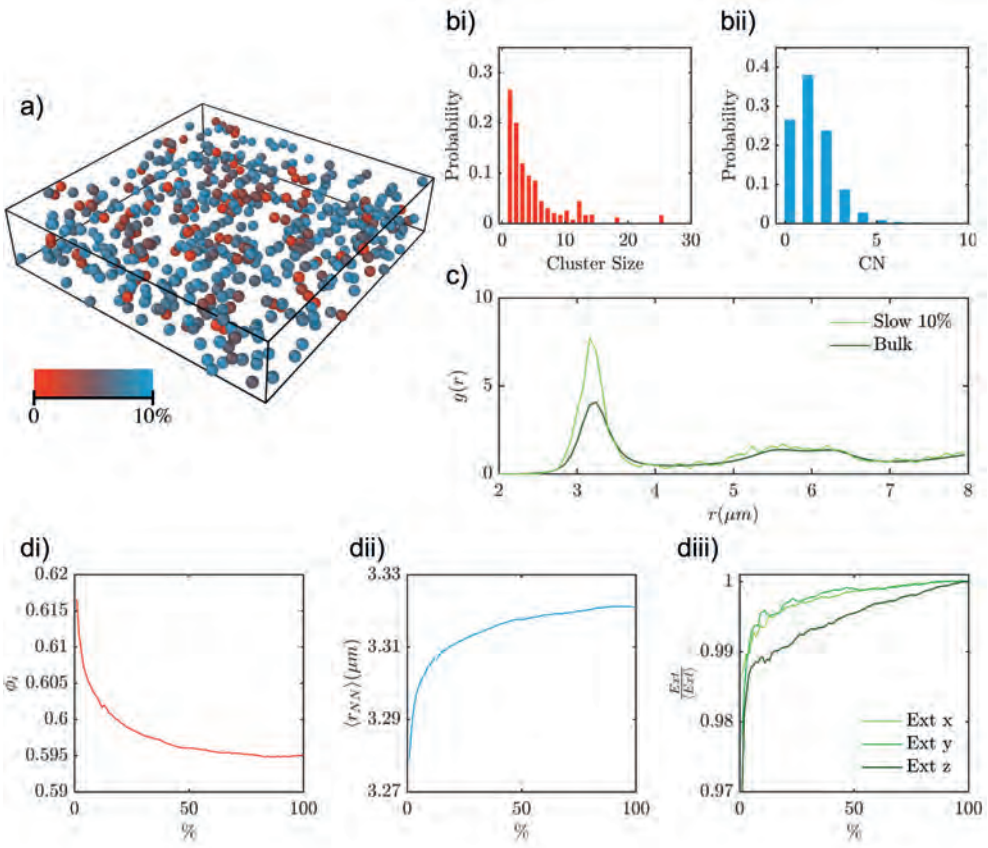

Figure 4.5: a) 3D reconstruction of the rotationally slow subpopulation which is defined as the slowest 10%, see SI 4.6.8. Particles are coloured by their rotational mobility. bi) Distribution of cluster sizes formed by rotationally slow subpopulation. bii) Coordination number (CN), of rotationally slow subpopulation. c) $g(r)$ of bulk population and $g(r)$ of rotationally slow subpopulation. di) Plot of local ϕ_i against cumulative average of the population ranked by increasing rotational mobility. dii) Plot of average nearest neighbour distance, $\langle r_{NN} \rangle$, against cumulative average of the population ranked by increasing rotational mobility. diii) Plot of extent of coordination shell in x, y and z ($Ext\,x$, $Ext\,y$ and $Ext\,z$) against the cumulative average of the population ranked by increasing rotational mobility.

Fig 4.5a). Only 26% of the population is isolated from other slow particles, in a cluster of size 1, while the other particles exist in small clusters of maximum size ~ 15, much smaller than clusters formed by the translational heterogeneities [10]. Fig 4.5b) shows a distribution of the coordination numbers of the slow subpopulation. Most of the rotationally slow particles have relatively low coordination numbers with the majority having only one slow neighbour. This suggests the rotationally slow particles do exhibit a degree of clustering but these clusters are made of single-particle contacts; particles in contact with one or two others forming 'string-like' extended clusters as opposed to more compacted clusters. This is further cemented in Fig 4.5ci) which compares the $g(r)$ of the bulk population to the $g(r)$ calculated over the slow subpopulation. The strongly increased peak height at the nearest neighbour distance suggests an increased probability of finding a neighbour in the rotationally slow population.

We further divide the slow subpopulation into the slowest $0-5\%$ and $5-10\%$ to examine whether the probability that the particle has a neighbour within the same subdivision changes with rotational mobility. We find that the probability that a particle in the $0-5\%$ rotationally slowest subpopulation has a neighbour in the same subdivision is 0.58 while the probability drops to 0.46 for particles in $5-10\%$. Therefore more rotationally arrested particles have a greater probability that at least one neighbour will also be more rotationally arrested. This further cements that rotational arrest in dense colloidal packings is governed by interparticle friction.

Finally, we probe the correlations between rotational mobility and the local environment, quantified by the local volume fraction, ϕ_i, the average nearest neighbour distance, $\langle r_{NN} \rangle$, and the extent of the coordination shell in x, y and z. In order to examine small changes across these quantities we first rank the whole population of particles by increasing rotational mobility. Each quantity is then examined as a cumulative average of the population ordered by increasing rotational mobility; the average value for 5% is calculated over the slowest 5% of the particles and the value for 95% is calculated over the 95% slowest particles in the population. Fig 4.5 di) shows the variation in ϕ against this metric. As the percentage of the population decreases, and we approach the rotationally slowest particles, ϕ_i increases by roughly 1%. This small increase suggests that the more rotationally arrested particles experience a higher local volume fraction. This is corroborated in Fig 4.5 dii) which shows a plot of $\langle r_{NN} \rangle$. Similarly to ϕ we see a small decrease in the mean nearest neighbour distance at lower percentages, and therefore slower dynamics. We can further probe the source of this

decrease by examining the extent of the coordination shell in x, y and z, which is shown in Fig 4.5 diii). As the percentage of the population decreases, and therefore sampling is over particles with slower rotational dynamics, we see the extent of the coordination shell in all directions decrease, but there is a much larger decrease in z than for x and y. Therefore, rotationally slow particles experience a more compressed coordination shell in z. In short, the rotationally slow particles have, on average, a higher local volume mainly due to a decrease in the extent of the coordination shell in z, the direction of gravity.

4.5 Conclusion

We have described and characterised heterogeneous rotational dynamics in dense disordered phases of colloidal particles. In contrast to translational dynamics as ϕ increases a subpopulation of rotationally slow particles develops. The slow dynamical nature of this heterogeneity makes it difficult to observe in the ensemble averaged dynamics that are insensitive to slow particles. Additionally, we have established that the rotationally slow particles form small but extended clusters. Finally, we correlated the rotationally slow particles with a higher local volume fraction resulting from a compression in z of the coordination shell. This work sheds new light into the rotational dynamics of dense colloidal suspensions and the importance of examining the statistics at the single-particle level.

4.6 Supplementary Information

4.6.1 Materials

3-(trimethoxysilyl)propyl methacrylate (TPM, ≥97%, Sigma Aldrich), ammonium hydroxide solution (28% vol. NH_3 in H_2O, Alfa Aesar), azobisisobutyronitrile (AIBN, BDH, UK), Cyanine3 NHS Ester (Lumiprobe), BDP NHS Ester (Lumiprobe), Chloroform ($CHCl_3$, Fischer Scientific), 3-aminopropyl trimethoxysilane (APS, Sigma Aldrich), 4-aminostryene (4-AS, Sigma Aldrich), acetone (Sigma Aldrich), Sodium Hydroxide (NaOH, Sigma Aldrich), Hydrochloric Acid (HCl, Sigma Aldrich), Pluronic® F-108 (F-108, Sigma Aldrich), trichloroethylene (TCE, ≥99.5%, Sigma Aldrich), 1,2,3,4-tetrahydronaphthalene (tetralin, anhydrous, 99%, Sigma Aldrich) and tetrachloroethylene (PERC, 99%, Alfa Aesar) were used as received. A polyisobutylene succinic anhydride stabilizer, OLOA 11000, was provided by Eric Dufresne and Azelis. Double-distilled water was sourced from an PURELABS Chorus 1 ultrapure water unit.

4.6.2 Synthesis of OCULI Particles

We synthesise OCULI particles by following the protocol developed Ref. [23]. 3-trimethoxysilylpropyl methacrylate (TPM) oil is hydrolysed under acidic conditions by diluting 2ml TPM in 20ml 0.05mM HCl and stirring for 1 hour. 4ml of hydrolysed TPM (hTPM) was diluted in 21ml 0.5mM HCl before 25ml 0.028% NH_4OH is added which triggers rapid condensation followed by nucleation and growth of monodisperse droplets. These droplets can were labelled with BDP-FL NHS ester (1mg/ml $CHCl_3$ functionalised with APS, [23]) and crosslinked to form hardened TPM microspheres, referred to as the 'eye' of the particles. During cross-linking a spatulaful of AIBN was added to the suspension of droplets before heating to $80°C$ for 3 hours. The particles were washed by repeated centrifugation at 1000g for 10 min before being resuspended to 10ml ($\approx \phi = 6\%$). 2ml of the eye particles were added to a vial of 5ml 0.028% NH_4OH and $150\mu l$ hTPM and tumbled for 30 min. This created a thin layer of liquid TPM on each particle to favour subsequent growth of this layer as opposed to secondary nucleation. The eye solution was then diluted in 20ml 0.028% NH_4OH and stirred while hTPM was dripped into the flask at a rate of $100\mu l/min$. The hydrolysed TPM wets onto the surface of these particles, eventually engulfing the eye inside a droplet. However, due to interface pinning the eye is held at the interface inside the droplet. 5ml of 5% wt F108 was added to the suspension before the droplets were labelled with Cyanine 3 NHS ester (1mg/ml in acetone functionalised with 4-AS [24]). The

particles were then crosslinked using the same procedure described previously. This outer shell is referred to as the 'body' of the OCULI. A non-florescent shell is then grown around the particle to aid particle location at high ϕ. This is done via a two step process [29]. First small TPM 'lobes' are added to the particle, these are created by adding hydrolysed TPM to a TPM surface that has been functionalised with F108. This was done by suspending the OCULI particles in 500ml 1mM NaOH which has been preheated to $80°C$ and adding 20ml hTPM. Once these lobes are crosslinked the particles are resuspended in 0.028% NH_4OH and alloquots of hTPM are added to wet in between the lobes and allow the particle to regain a spherical shape.

4.6.3 Sample Preparation

Particles are suspended in a 42:58 w/w tetralin:trichloroethylene solution using a procedure for transferring from polar to non-polar solvents developed by Liu *et al* [29]. All organic solvents contain 5% wt weight OLOA 11000. This concentration of OLOA ensures that there is a hard-sphere like interaction potential [23].

4.6.4 Confocal Microscopy

The system was imaged with two-channel 3D confocal laser scanning microscope; Olympus IX73 inverted microscope, 60× Olympus Plan Apochromat oil immersion objective (NA = 1.42). High speed imaging was achieved by Thorlabs confocal 12kHz resonant scanner and an objective-mounted piezoelectric Z-stage (Physik Instrumente). A total image volume of $102.4\times102.4\times50.2\mu m^3$ was recorded in 5.9s (800 frames over 80 minutes). Simultaneous illumination of the sample with laser of wavelength 488nm and 532nm allows near simultaneous imaging of both components of the OCULI particle. To capture the whole density profile, 3D stacks were taken at two different heights: between 10 to 60 μm and between 50 to 100 μm. The data is averaged over 3 independent datasets.

4.6.5 Particle Sizing

The particles are sized from SEM microscopy to give a radius of 1.43 μm and polydispersity of 2.30%. To size particles in solution an ultra dilute suspension of $\phi \approx 0.01$ is prepared in a density matching suspension of tetralin:trichloroethylene:tetrachloroethylene [24]. The translational dynamics are recorded as the MSD given by Eq 4.1 and the translational diffusion coefficient is

extracted by fitting this data with $\langle \Delta r^2 \rangle = 6 D_T \tau$ (Fig 5.11a)) where,

$$D_T = \frac{k_B T}{6 \pi \eta R} \tag{4.5}$$

Using this we extract $D_T = 0.0554 \times 10^{-14} m^2 s^{-1}$ which results in a Brownian time of $\tau_T = 28.9s$. The rotational dynamics are recorded as the MSAD and the autocorrelation function, $C(\tau) = \langle u_t \cdot u_{t+\tau} \rangle$. From both D_R can be extracted from both measures by fitting $\langle \Delta \theta^2 \rangle = 4 D_R \tau$ and $C(\tau) = \exp(\frac{\tau}{2 D_R})$ respectively (Fig 5.11b) and c)). In both cases D_R is given by,

$$D_R = \frac{k_B T}{8 \pi \eta R^3}, \tag{4.6}$$

and the particle size can be extracted using the ratio,

$$R = \sqrt{\frac{3 D_T}{4 D_R}}. \tag{4.7}$$

We note a small difference in the D_R extracted in from the $C(\tau)$ and MSAD which give values of $0.0172 s^{-1}$ and $0.0161 rad^2 s^{-1}$. This results in a value for R of $1.55 \mu m$ using the D_R extracted from $C(\tau)$ and of $1.61 \mu m$ using the D_R extracted from the MSAD. Both of these values are larger than the radius recorded from SEM due to the shrinkage of particles in the vacuum in the SEM. A radius of $1.55 \mu m$ is used for the calculation of ϕ. We also extract the rotational relaxation time defined as $\tau_R = \frac{1}{2 D_R}$ which gives $\tau_R = 29.1s$ and $\tau_R = 31.1s$ from the $C(\tau)$ and MSAD respectively.

4.6.6 Particle Tracking

Localisation of the particle positions and extraction of the orientation is described in [23]. Only particles trajectories where both the body and eye coordinates are followed for 95% of the particle trajectory are used for analysis. We note that there is a small subpopulation of particles tracked for less than 100 frames, as shown in Fig 4.7. We attribute these short trajectories to a single particle being missed for several frames and thus the trajectory being broken up into several smaller ones. To prevent counting

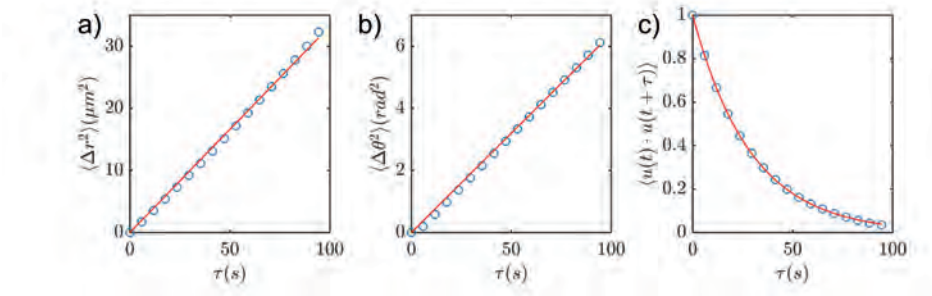

Figure 4.6: a) Plot of MSD against τ for sample of $\phi = 0.01$. b) MSAD against τ for sample of $\phi = 0.01$. c) $C(\tau)$ against τ for sample of $\phi = 0.01$.

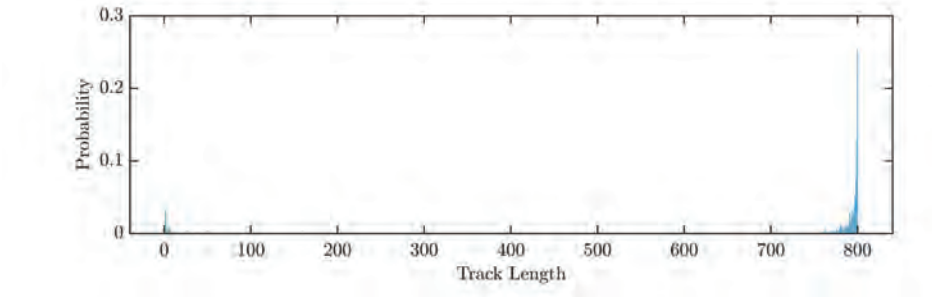

Figure 4.7: Histogram of track length of $\phi = 0.6$.

these broken-up trajectories multiple times in the single-particle dynamics (hence, not ensemble averaged), we exclude tracks of <100 frames from this analysis.

Finally we note that a very small number of particles ($< 1\%$) are rotationally arrested and have a nearest neighbour distance significantly smaller than the particle diameter of $3.1\mu m$, as shown in Fig 4.8. We attribute this to particles that have fused together during particle synthesis. These dimer particle are excluded from our analysis by excluding particles with a nearest neighbour distance smaller than $2.6\mu m$ (see Fig 4.8) [23].

4.6.7 Rotational Displacement

Rotational displacement was calculated in line with previous studies [30]. First we define the rotational trajectory between each frame as

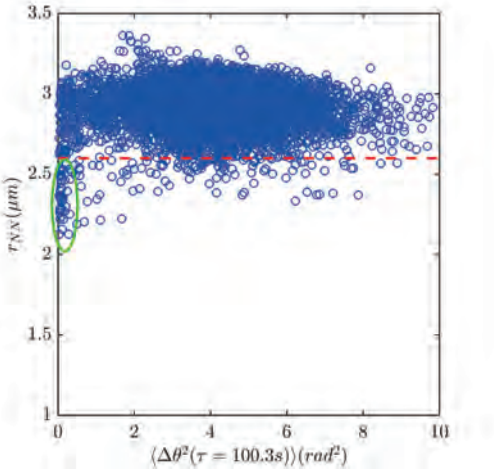

Figure 4.8: Distribution of $\langle \Delta\theta^2 \rangle$ at $\tau = 100.3s$ against nearest neighbour distance, r_{NN} from data used in Fig 4.5. Red line indicates cut off for exclusion of dimers. Green circle highlights dimers.

$$\psi(t_2) = \hat{\omega} \cdot \alpha, \tag{4.8}$$

where $\hat{\omega}$ is the axis of rotation between frames, ($\hat{\omega} = \hat{u}(t_1) \times \hat{u}(t_2)$), and α is the angle of rotation, ($\alpha = \cos^{-1}(\hat{u}(t_1) \cdot \hat{u}(t_2))$). The sum of these displacement between each frame is evaluated as the integral,

$$\theta(\tau) = \int_1^{t_2} \psi(t) dt. \tag{4.9}$$

The resulting the rotational trajectory, θ, can be used as a direct analogue to the translational trajectory.

4.6.8 Rotationally Slow Subpopulation

We define a cut off of 10% of the population as rotationally slow by plotting the MSAD(τ=100.3s) as a cumulative average of the population ranked by their rotational displacement; the value at 5% is averaged over the slowest 5% and the average at 95% is averaged over the slowest 95%. Plotting this on a log scale shows a distinct kink which

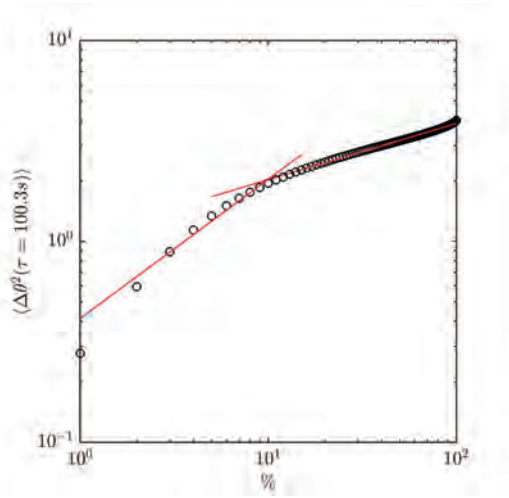

Figure 4.9: MSAD(τ=100.3s) as function of proportion of population from data used in Fig 4.5.

can be more clearly identified by fitting the data with two straight lines as shown in Fig 4.9. We take the point of intersect between the two lines, 10%, as the cut off to be rotationally slow.

4.6.9 Acknowledgements

All particle synthesis, imaging and analysis was carried out by R. A. Crothers. We thank B. van der Meer and T. Yanagishima for useful discussions.

4.7 Bibliography

[1] G. L Hunter and E. R Weeks. The physics of the colloidal glass transition. *Rep. Prog. Phys.*, 75(6):066501, 2012.

[2] H. Sillescu. Heterogeneity at the glass transition: a review. *J. Non-Cryst. Solids*, 243(2-3):81–108, 1999.

[3] L. Berthier, G. Biroli, J. Bouchaud, L. Cipelletti, and W. van Saarloos. *Dynamical heterogeneities in glasses, colloids, and granular media*, volume 150. OUP Oxford, 2011.

[4] L. Chu, K. Xu, R. Graf, Z-C. Yan, J. Li, and Y-F. Yao. Dynamic heterogeneity in homogeneous polymer melts. *Soft matter*, 17(25):6081–6087, 2021.

[5] J. Fan, H. Emamy, A. Chremos, J. F. Douglas, and F. W. Starr. Dynamic heterogeneity and collective motion in star polymer melts. *J. Chem. Phys.*, 152(5), 2020.

[6] W. Zhao, H. Huo, Z-Y. Sun, and Z-Y. Lu. Data-driven analysis of dynamical heterogeneity in polymer melts near surfaces. *Comput. Mater. Sci.*, 235:112811, 2024.

[7] M. G. Mazza, N. Giovambattista, H. E. Stanley, and F. W. Starr. Connection of translational and rotational dynamical heterogeneities with the breakdown of the stokes-einstein and stokes-einstein-debye relations in water. *Phys. Rev. E*, 76:031203, 2007.

[8] T. G. Lombardo, P. G. Debenedetti, and F. H. Stillinger. Computational probes of molecular motion in the Lewis-Wahnström model for ortho-terphenyl. *J. Chem.l Phys.*, 125(17):174507, 11 2006.

[9] W. K. Kegel and A. van Blaaderen. Direct observation of dynamical heterogeneities in colloidal hard-sphere suspensions. *Science*, 287(5451):290–293, 2000.

[10] E. R Weeks, J. C. Crocker, A. C. Levitt, A. Schofield, and D. A. Weitz. Three-dimensional direct imaging of structural relaxation near the colloidal glass

transition. *Science*, 287(5453):627–631, 2000.

[11] A. L. Thorneywork, D. G. A. L. Aarts, J. Horbach, and Roel P. A Dullens. On the gaussian approximation in colloidal hard sphere fluid. *Soft Matter*, 12:4129–4134, 2016.

[12] A. S Keys, A. R Abate, S. C Glotzer, and D. J. Durian. Measurement of growing dynamical length scales and prediction of the jamming transition in a granular material. *Nat. Phys.*, 3(4):260–264, 2007.

[13] O. Dauchot, G. Marty, and G. Biroli. Dynamical heterogeneity close to the jamming transition in a sheared granular material. *Phys. Rev. Lett.*, 95(26):265701, 2005.

[14] W. C. K. Poon. Colloids as big atoms. *Science*, 304(5672):830–831, 2004.

[15] P. N. Pusey and W. Van Megen. Phase behaviour of concentrated suspensions of nearly hard colloidal spheres. *Nature*, 320(6060):340–342, 1986.

[16] A. Kasper, E. Bartsch, and H. Sillescu. Self-diffusion in concentrated colloid suspensions studied by digital video microscopy of core- shell tracer particles. *Langmuir*, 14(18):5004–5010, 1998.

[17] A. H Marcus, J. Schofield, and S. A. Rice. Experimental observations of non-gaussian behavior and stringlike cooperative dynamics in concentrated quasi-two-dimensional colloidal liquids. *Phys. Rev. E.*, 60(5):5725, 1999.

[18] S. Schütter, A. Roller, J. Kick, J-M. Meijer, and A. Zumbusch. Real-space imaging of translational and rotational dynamics of hard spheres from the fluid to the crystal. *Soft matter*, 13(44):8240–8249, 2017.

[19] M. Kim, S. M. Anthony, S. C. Bae, and S. Granick. Colloidal rotation near the colloidal glass transition. *J. Chem. Phys.*, 135(5), 2011.

[20] J. Geiger, N. Grimm, M. Fuchs, and A. Zumbusch. Decoupling of rotation and translation at the colloidal glass transition. *J. Chem. Phys.*, 161(1):014507, 2024.

[21] K. V. Edmond, M. T. Elsesser, G. L. Hunter, D. J. Pine, and E. R. Weeks.

Decoupling of rotational and translational diffusion in supercooled colloidal fluids. *PNAS*, 109(44):17891–17896, 2012.

[22] S. Vivek and E. R. Weeks. Decoupling of translational and rotational diffusion in quasi-2d colloidal fluids. *J. of Chem. Phys.*, 147, 10 2017.

[23] T. Yanagishima, Y. Liu, H. Tanaka, and R. P. A. Dullens. Particle-level visualization of hydrodynamic and frictional couplings in dense suspensions of spherical colloids. *Phys. Rev. X*, 11:021056, 2021.

[24] R. A Crothers, N. H. P. Orr, B. van der Meer, R. P. A. Dullens, and T. Yanagishima. Characterization and optimization of fluorescent organosilica colloids for 3d confocal microscopy prepared under "zero-flow" conditions. *Langmuir*, 39(15):5306–5314, 2023.

[25] G. L. Hunter, K. V. Edmond, M. T. Elsesser, and E. R. Weeks. Tracking rotational diffusion of colloidal clusters. *Opt. Express*, 19(18):17189–17202, 2011.

[26] J. P. Boon and S. Yip. *Molecular hydrodynamics*. Courier Corporation, 1991.

[27] J. P. Hansen and I. R. McDonald. *Theory of simple liquids third edition*. Elvesier academic press, 2006.

[28] B. Van Der Meer, T. Yanagishima, and R. P. A. Dullens. Attraction-enhanced emergence of friction in colloidal matter. *Phys. Rev. Lett.*, 134(7):078202, 2025.

[29] Y. Liu, T. Yanagishima, A. Curran, K. V. Edmond, S. Sacanna, and R. P.A. Dullens. Colloidal organosilica spheres for three-dimensional confocal microscopy. *Langmuir*, 35, 2019.

[30] L. H. Gary, K. V Edmond, M.T Elsesser, and E. R. Weeks. Tracking rotational diffusion of colloidal clusters. *Opt. Express*, 19(18):17189–17202, 2011.

Chapter 5

On the Coupling of Translational and Rotational Dynamics in the Colloidal Fluid, Crystal and Glass

We use confocal microscopy to simultaneously observe translational and rotational dynamics of colloidal particles in the fluid, crystal and glass. First we evaluate the ensemble averaged translational and rotational dynamics in the dense fluid where we observe a decoupling of the ensemble averaged diffusion coefficients. We then examine the single-particle behaviour in terms of individual displacements between frames and single-particle mean squared displacement, MSD, and mean squared angular displacement, MSAD, to reveal a correlation in the magnitude of the dynamics at the single-particle level, at short lag times, which is lost once the ensemble averaged dynamics become Gaussian. The correlation between the magnitude of the MSD and MSAD at short lag time extends into the crystal and glass phase. However, the impact of interparticle friction in the glass complicates this correlation due to the development of a rotationally slow subpopulation, which we quantify at the single-particle level using the correlation coefficient, C.

5.1 Introduction

The coupling between translational and rotational dynamics as the glass transition is approached has long been a subject of interest to the condensed matter physics community [1–3]. A particle in a continuum will undergo translational and rotational diffusion with respective diffusion coefficients D_T and D_R. These are described, for a spherical particle, by the Stokes-Einstein (SE) equation [4],

$$D_T = \frac{k_B T}{6\pi\eta R}, \tag{5.1}$$

and the Stokes-Einstein-Debye (SED) equation [5]

$$D_R = \frac{k_B T}{8\pi\eta R^3}. \tag{5.2}$$

Both diffusion coefficients are coupled to the viscosity of the medium, η, and the particle radius, R and therefore through this, the translational and rotational dynamics are coupled in the dilute limit. However, as the glass transition is approached translational and rotational dynamics of particulate systems become more complex and the coupling between translational and rotational dynamics has been much discussed across many different fields [6–17].

Simulations of supercooled fluids and molecular glasses show in general a decoupling of D_T from η as T decreases towards the glass transition temperature, T_g, where D_T is enhanced beyond what is predicted from the SE equation [6–11]. This decoupling is often attributed to the onset of dynamic heterogeneity where a more mobile subpopulation develops that is able to undergo cage breaking as T approaches T_g [18–23]. The enhanced D_T is often attributed to the fast translational heterogeneities [7], although some alternate theories still persist [24]. The general consensus for rotational dynamics is that D_R remains coupled to η even at high T as no such heterogeneity is observable in rotational dynamics [11].

Colloidal particles have long been used as a model system for the phase behaviour of molecular and atomic systems as their length and timescales allows their dynamics to be directly observable by optical microscopy [25]. The study of the dynamics of colloidal

particles in the fluid, crystal and glass phase has therefore been the subject of much discussion from the dynamics at phase transitions [18, 19, 26], to crystal nucleation and growth [27–30] to the dynamics and properties of interfaces [27, 31, 32].

However, observing rotational dynamics of spherical particles has long been an experimental challenge. Consequently, studies of the translational and rotational dynamics of colloidal particles at high volume fraction, ϕ, rely on tracer particles in a host population. Here the tracer has been altered in some way, including shape [12–14] or optical properties [15–17], to allow direct observation of rotational dynamics. Studies of anisotropic tracers show, as might be expected, rotational dynamics are more restricted than translational dynamics when ϕ increases [12–14]. Furthermore, it was shown that for an anisotropic particle D_R remains coupled to η as the glass transition is approached, while the measured D_T is up to an order of magnitude higher than what is predicted at that ϕ by the SE equation [12]. Studies of isotropic tracer particles observe the opposite trend upon increasing ϕ as translational dynamics become increasingly restricted while rotational dynamics are relatively unimpeded and remains diffusive, in both a glassy [15, 17] and crystalline suspensions [16].

Intriguingly, a computational study of soft Janus particles sheds new light into the coupling of translational and rotational dynamics in a colloidal glass [33]. As T approaches T_g in this system rotational and transitional diffusion appears to decouple at the ensemble averaged level but a correlation emerges in the translational and rotational relaxation times, τ_T and τ_R respectively, at the *single-particle level*. Particularly, as T approaches T_g, particles with a faster than average τ_T become more likely to have a faster than average τ_R. This highlights the need to directly observe the dynamics of *all* particles at the single-particle level to truly understand the coupling between translational and rotational dynamics.

In this study, we aim to address the coupling between translational and rotational dynamics in the colloidal fluid, crystal and glass phases for *all particles*. To achieve this we exploit the newly developed 'Off-Centre Under Laser Illumination' (OCULI) particle where a 3-(trimethoxysilyl)propyl methacrylate, TPM, microsphere is embedded off-centre within a larger microsphere of the same material [34]. Crucially, the two components of the particle, referred to as the eye and body respectively, are labelled with different fluorescent dyes. Therefore, simultaneous imaging but independent tracking of the body and the eye of each particle allows for the direct observation

of the translational *and* rotational dynamics of every single particle in the system. We combine this particle system with a unique solvent mixture, which allows tuning of the density mismatch between particle and solvent while maintaining the refractive index match [35]. We use this to create both a crystal-fluid sedimentation-diffusion equilibrium and a dense amorphous sediment to directly observe the translational and rotational dynamics of every particle in the colloidal fluid, crystal and glassy phases. For the first time in an experimental system we can investigate the coupling between the translational and rotational dynamics at both the ensemble-averaged and the single-particle level.

5.2 Experimental System

OCULI particles of diameter 3.1 μm are synthesised following the protocol in ref [34], see Supplementary Information, SI 5.5.2. Each component of the OCULI particle is made from the same material, TPM, so both the body and the eye have the same mass density and refractive index. A non-flourescent shell is added around the particle to facilitate tracking at dense ϕ [36]. Our previous work has shown that TPM particles can be suspended in a ternary solvent mixture which allows tuning of the mass density mismatch between particle and solvent, and therefore the gravitational length, ξ_g, while maintaining the refractive index match between the two [35]. This ternary solvent system contains tetralin (TTL), trichloroethylene (TCE) and tetrachloroethylene (PERC) First, a binary solution of TTL and TCE 42:58 w/w is mixed which approximately refractive index matches the TPM microspheres. PERC closely matches the refractive index of TPM but has a much higher density [35]. Therefore, addition of PERC to the refractive index matching solution of TCE:TTL can be used to tune the gravitational length while maintaining the refractive index match.

We prepare two solvent mixtures by diluting the initial refractive index matching solution of TCE and TTL to 10% and 40% PERC v/v. We then suspend the OCULI particles, from the same batch, in each solvent at initial volume fraction $\phi = 0.3$. All organic solvents are prepared with 5% OLOA stabiliser which has been shown to result in a hard-sphere like interaction potential [34]. Each particle suspension is sealed in a capillary and allowed to sediment overnight to establish a sedimentation-diffusion equilibrium. Fig 5.1a) shows the two resulting density profiles for each sample. We characterise each sample by the gravitational length, $\xi_g = \frac{k_B T}{4\pi R^3 \Delta\rho g}$, where R is the

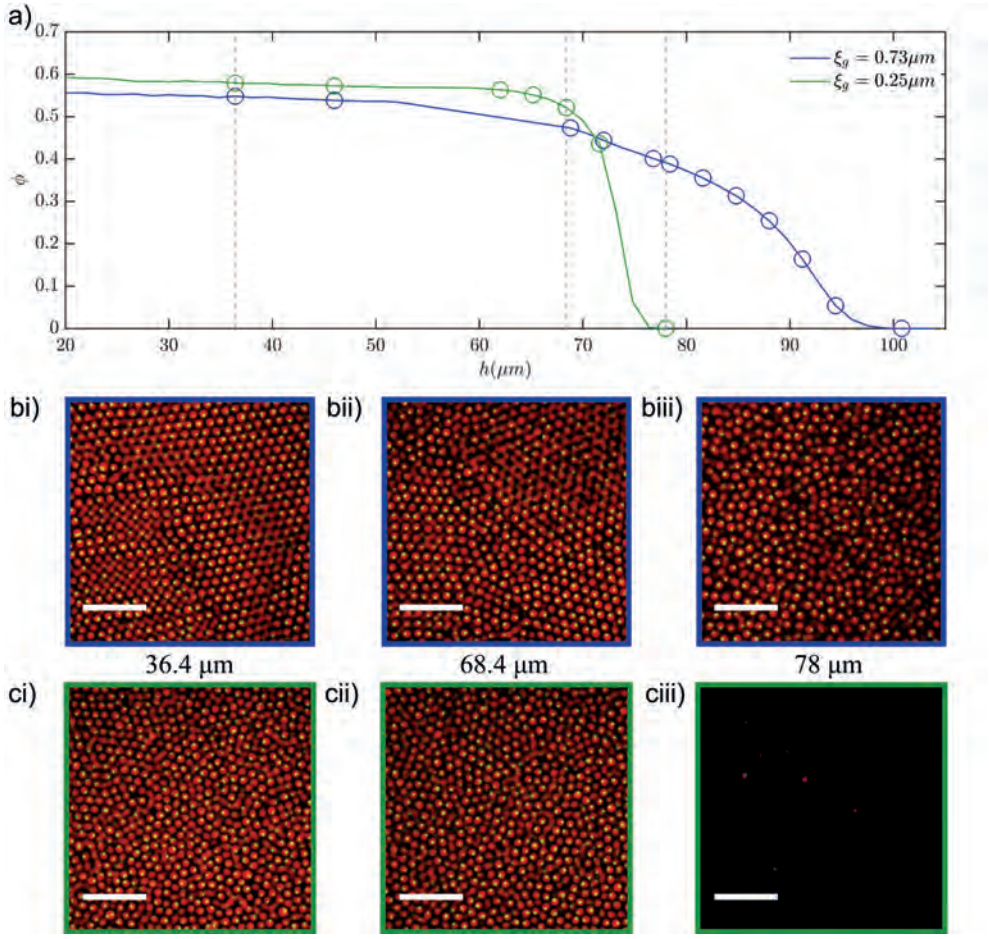

Figure 5.1: a) Density profiles of sedimentation-diffusion equilibria of OCULI particles in systems of different gravitational length. Symbols indicate where different volume fractions, ϕ, are sampled at different heights. bi-iii) Confocal images at different heights, indicated as dashed lines in a), within the system of $\xi_g = 0.25\mu m$. ci-iii) Confocal images at different heights, indicated as dashed lines in a) within system of $\xi_g = 0.73\mu m$ where the scale bar is $20\mu m$.

particle radius and $\Delta\rho$ is the density difference between the particle and the solvent. For the particles suspended in a solution of 40% PERC, $\Delta\rho = 0.037 g cm^{-3}$, $\xi_g = 0.73\mu m$. Fig 5.1b) shows confocal images taken at various heights within this sample where at the bottom a crystalline phase is observed which eventually melts to the fluid phase at the top of the sample. For the second sample prepared in a solution of 10% PERC, $\Delta\ \rho = 0.106 g cm^{-3}$, and $\xi_g = 0.25\mu$m which results in a dense, amorphous sediment

with a very steep decline of ϕ at the top. Fig 5.1 b) shows confocal images at different heights within the sample, where we can observe an amorphous structure at the bottom, while the liquid phase can be observed at the top. Therefore by imaging at different heights in both samples we can simultaneously study the translational and rotational dynamics in the colloidal fluid, crystal and glass phases.

5.3 Results and Discussion

5.3.1 Fluid

We first examine the coupling of D_T and D_R in the fluid phase. To this end, we characterise the dynamics in the crystal-fluid sedimentation-diffusion equilibrium (shown in Fig 5.1). Here, we expect both translational and rotational dynamics in the fluid phase to display diffusive behaviour within the experimental timeframe. To extract D_T and D_R we measure the ensemble averaged mean squared displacement (MSD) and mean squared angular displacement (MSAD), shown in Fig 5.2a) and b) respectively. The MSD is diffusive at low ϕ but as ϕ increases we see the onset of a transient plateau due to caging. Eventually once ϕ increases to 0.54 we see the MSD plateau for the whole experimental timeframe as the particles undergo freezing and become localised in the crystalline lattice. Notably, this is in direct contrast to the MSAD, shown in Fig 5.2b), which remains comparatively unaffected by the increase in ϕ, appearing diffusive at all times even beyond the freezing transition. This is consistent with previous studies of isotropic tracer particles in dense fluid and crystalline suspensions [15, 16].

The MSD for diffusive motion in 3D is described by,

$$\langle \Delta r^2 \rangle = 6 D_T \tau, \tag{5.3}$$

where τ is the lag time. We use Eq 5.3 to extract D_T for all ϕ that display long-time diffusive behaviour over the experimental timeframe. Notably, when ϕ is above 0.46 the MSD is plateaued over the course of the experiment, so extraction of D_T is not possible. Similarly D_R can be described by,

$$\langle \Delta \theta^2 \rangle = 4 D_R \tau. \tag{5.4}$$

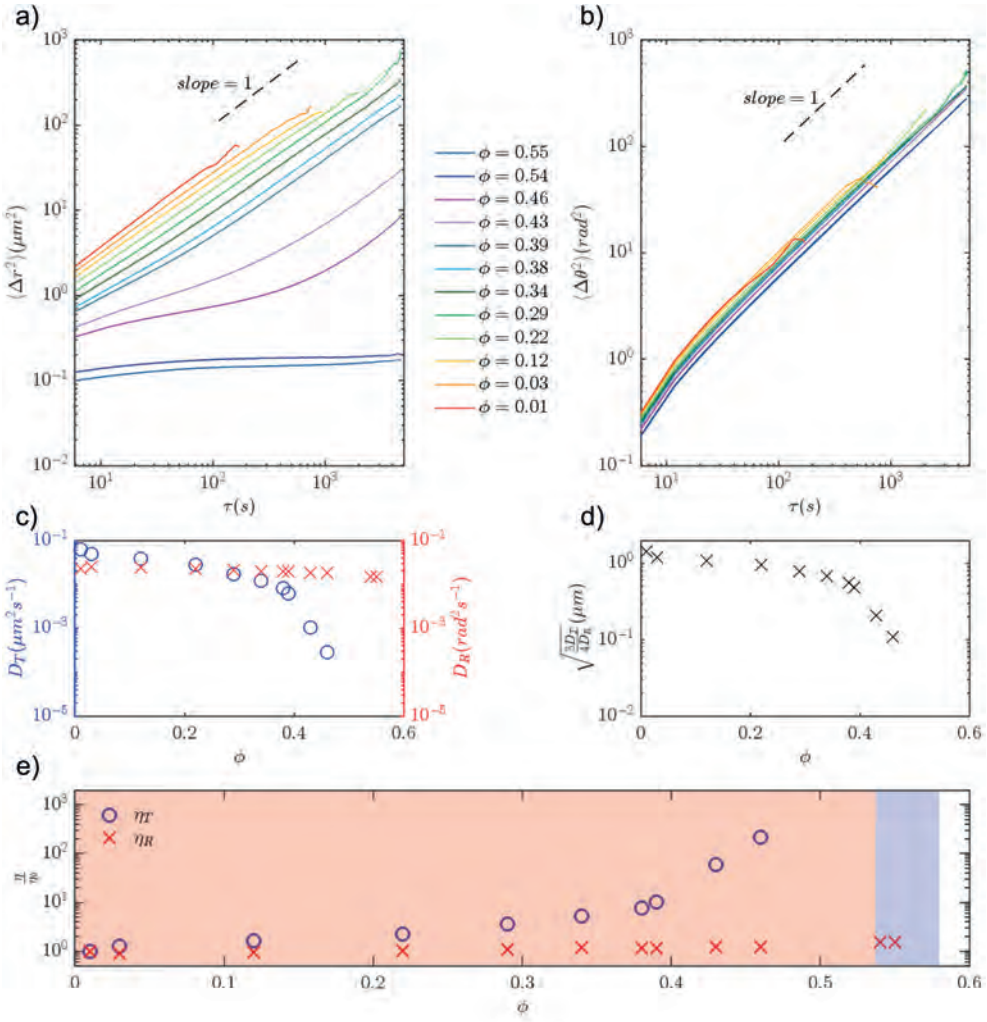

Figure 5.2: a) MSD for a range of ϕ recorded in the sample with $\xi_g = 0.73\mu m$, in the crystalline and fluid phases and b) corresponding MSAD for the same ϕ. c) D_T and D_R as a function of ϕ. d). Ratio of $\sqrt{3D_T/4D_R}$ as a function of ϕ. e) The viscosities, η_T and η_R, as a function of ϕ. Note extraction of D_T above 0.46 is not possible as diffusive behaviour is not reached over the course of the experiment. Shading denotes the phase: red is the fluid phase and blue the crystal phase.

In contrast to translational dynamics, the rotational dynamics are diffusive for all ϕ so it is possible to extract D_R for all ϕ investigated using Eq 5.4. Both diffusion coefficients as a function of ϕ are shown in Fig 5.2c) where a stark contrast can be observed; while D_T decreases by several order of magnitude upon increasing ϕ, D_R shows a much smaller decrease.

We can gain further insight into the decoupling of D_T and D_R by examining the ratio,

$$\sqrt{\frac{3D_T}{4D_R}}. \tag{5.5}$$

In the dilute limit translational and rotational dynamics are well described by the SE and SED equations (Eq 5.1 and Eq 5.2 respectively) and the ratio in Eq 5.5 reduces to the particle radius, R. In Fig 5.2d) we show Eq 5.5 for all ϕ where extraction of both D_T and D_R is possible. At low ϕ Eq 5.5 gives $R = 1.38\mu m$ which is slightly smaller than the particle size determined in a density matched sample at $\phi = 0.01$ in SI 5.5.4, which we attribute to fractionation occurring during the establishment of the sedimentation-diffusion equilibrium. However, a decline is then observable beginning at $\phi \approx 0.22$ and increasing in slope at $\phi \geq 0.38$. Therefore, it appears that D_T and D_R already decouple in the dense fluid phase and this decoupling increases with increasing ϕ. Hence, both D_T and D_R experience an increase in η, but D_T experiences a much greater increase in the apparent 'translational viscosity', η_T, than D_R does with the 'rotational viscosity', η_R. By fixing the particle radius as $R = 1.38\mu$m and using Eq 5.1 and Eq 5.2 we extract the ensemble averaged η_T and η_R from the measured D_T and D_R. Fig 5.2e) shows a plot of η_T and η_R against ϕ, where the separation with increasing ϕ is obvious. At low ϕ, η_T and η_R show relatively good agreement, however as ϕ increases, η_T increases rapidly while η_R shows only a small increase. At $\phi = 0.46$, η_T is more than two orders of magnitude larger than η_R indicating that as ϕ increases D_T and D_R decouple due to the difference in the viscosity experienced by the particle undergoing each type of motion.

The increasing separation between η_T and η_R can be rationalised by considering how a particle experiences the environment around it when it translates or rotates at different ϕ. A low ϕ, a particle experiences very little of the other particles in the system and neither translational or rotational dynamics are restricted. In this case, a particle

experiences only the solvent it is suspended in, and η_T and η_R are simply η of the solvent. However, as ϕ increases in order for a particle to move it must move through a sea of other particles. A subsequent increase in η_T is observed which is in line with rheological studies of colloidal suspensions of different ϕ [37–39] and simulations [40, 41]. However we observe a much smaller increase in η_R as the MSAD remains diffusive. This is indicative of a lack of interparticle friction which would restrict the rotational dynamics of the particles [42]. Therefore, unlike for translational dynamics, when a particle rotates in the dense fluid phase it experiences predominately the solvent around it, and η_R remains closely coupled to η of the solvent. Previous studies have shown that η_R only undergoes a similar increase for an anisotropic tracer particle [12], when particle rotation requires it to move through the rest of the population. In summary, in the dense fluid phase an isotropic particle experiences neighbouring particles only when it tries to move translationally and experiences mainly the solvent when it tries to rotate.

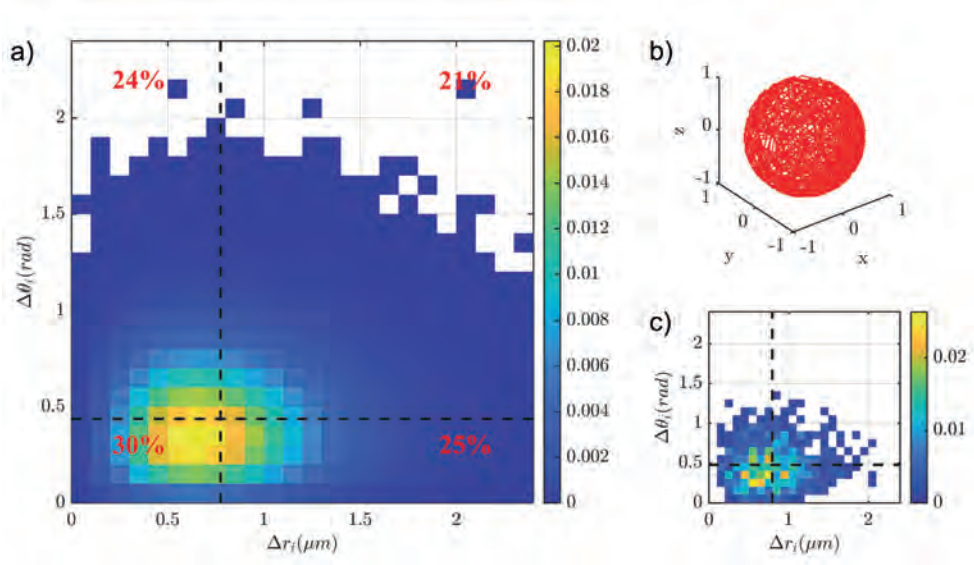

Figure 5.3: a) 2D histogram of single-particle translational displacement (Δr_i) and single-particle rotational displacement ($\Delta\theta_i$) between each frame for the fluid phase at $\phi = 0.38$. Dashed lines indicates the ensemble averages for both axes. Colour bar indicates the normalised probability. b) Typical rotational particle trajectory projected onto unit sphere. c) Translational displacement (Δr_i) and rotational displacement between each frame ($\Delta\theta_i$) for particle shown in b).

We next examine translational and rotational motion at the single-particle level for *all* particles using the OCULI particles. First, we examine the correlation between

individual particle displacements by calculating the translational, Δr_i, and rotational displacement, $\Delta\theta_i$, between each frame for the whole trajectory of each particle. Fig 5.3a) shows a 2D histogram of Δr_i and $\Delta\theta_i$ for $\phi = 0.38$ and we observe that the displacements are not evenly distributed around the respective ensemble averaged means. The probability to sit in each quadrant is shown as a percentage in Fig 5.3a). An abundance of the individual displacements, 30%, sit in the lower left hand quadrant, where both translational and rotational displacements are small. Intriguingly, a similar abundance is not found in the upper right hand corner, where both the translational and rotational displacements are large. Therefore, we observe that a particle in the dense fluid phase has a high probability to take small simultaneous translational and rotational steps but the same is not true for large translational and rotational steps. A typical rotational particle trajectory is shown in Fig 5.3b) and a similar plot of Δr_i and $\Delta\theta_i$ for the same individual particle is shown in Fig 5.3c). The plots in Fig 5.3a) and Fig 5.3c) share a striking resemblance, where a high density of displacements sit in the lower left hand quadrant, implying this trend is replicated in each individual particle trajectory.

A correlation between individual translational and rotational steps may, at first glance seem at odds with our previous observation that the ensemble averaged D_T and D_R are decoupled. However, previous studies have made a similar observation [12, 15] and they suggest that when the individual displacements are averaged over long τ the correlation drops. To address this we investigate whether the time averaged behaviour, as quantified by the single-particle MSD, $\langle\Delta r_i^2(\tau)\rangle$, and single-particle MSAD, $\langle\Delta\theta_i^2(\tau)\rangle$ at short and long τ, still shows a degree of correlation. Fig 5.4a) and b) show $\langle\Delta r_i^2(\tau)\rangle$ and $\langle\Delta\theta_i^2(\tau)\rangle$ for the sample at $\phi = 0.38$ which both appear to be diffusive for each particle. The calculated $\langle\Delta r_i^2(\tau)\rangle$ and $\langle\Delta\theta_i^2(\tau)\rangle$ for each particle at $\tau = 11.8s$ are shown as a 2D histogram in Fig 5.4c) to examine the correlation in the time-averaged behaviour at short τ. The distribution is clearly skewed with the majority of the points sitting in the lower left, translationally and rotationally slow, and upper right, translationally and rotationally, fast quadrants. We have previously observed in Fig 5.3 that small translational and rotational steps are correlated. If a particle undergoes more simultaneously small steps a correlation in the time-average behaviour, at short τ can be expected. A similar result has been found in a computational study of the single-particle translational and rotational relaxation times, where similarly to our study the statistics for the *all particles* are known [33].

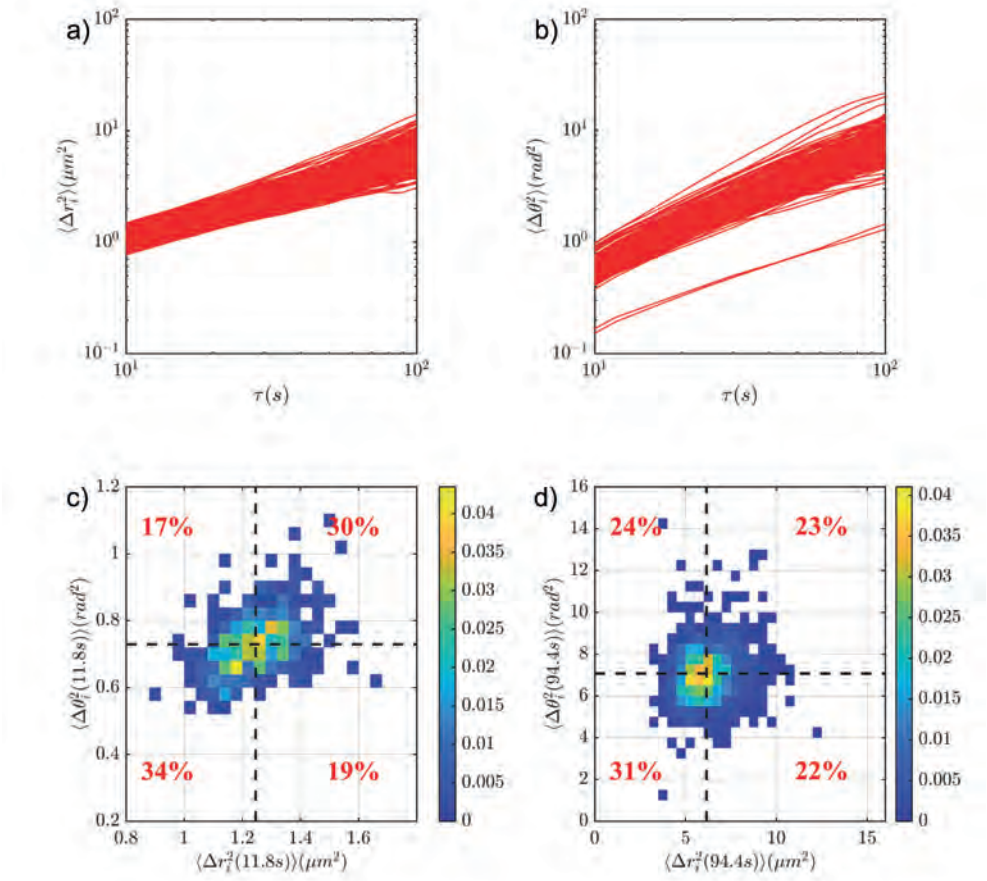

Figure 5.4: Single-particle MSDs for $\phi = 0.38$ b) Single-particle MSADs for $\phi = 0.38$ c) 2D histogram of $\langle \Delta r_i^2(\tau) \rangle$ and $\langle \Delta \theta_i^2(\tau) \rangle$ for $\tau = 11.8s$, ensemble averaged mean is shown in black for both. d) 2D histogram of $\langle \Delta r_i^2(\tau) \rangle$ and $\langle \Delta \theta_i^2(\tau) \rangle$ for $\tau = 94.4s$, ensemble averaged mean is shown in black for both.

If we examine the correlation at longer τ, shown in Fig 5.4d) the distribution looks significantly less skewed with more equal distribution in each quadrant. If compared with Fig 5.2a) we can see this coincidences with the τ where the ensemble averaged MSD has become diffusive. In a dense fluid a particle, at very short τ, interacts only hydrodynamically with the fluid around it in short time diffusive regime accessible only at low ϕ in our system. As τ increases the particle begins to interact directly

with the particles around it and the MSD shows a transient plateau, deviating from diffusive behaviour. At longer τ the particle has undergone enough of these direct interactions to experience the environment around it in as a continuum the MSD returns to diffusive behaviour and the particle displacements at this τ become Gaussian, this is known as the long-time diffusive regime. A correlation is only seen between MSD(τ) and MSAD(τ) before the translational dynamics become long-time diffusive. Once each particle environment can be approximated as the same the correlation is lost. We note that although at this time both translational and rotational dynamics become Gaussian the decoupling of η_T and η_R shows that the particle still experiences a different average environment for translational and rotational dynamics. Therefore we can directly observe what has been suggested in previous studies that in the dense fluid the accumulation of the individual translational and rotational displacements becomes more uncorrelated at longer τ [12].

5.3.2 Crystal

We next investigate the translational and rotational coupling in the crystal phase, found at the bottom of the fluid-crystal sample shown in Fig 5.1. As already seen in Fig 5.2, the MSD remains plateaued for the course of the experiment, so extraction of D_T is not possible and we therefore turn to the single-particle behaviour. Fig 5.5a) shows the 2D histogram of the individual translational, Δr_i, and rotational displacements, $\Delta\theta_i$, between each frame, which shows a striking resemblance to the histogram for a fluid, (Fig 5.3a). Again, a majority of displacements sit in the lower left quadrant of the distribution suggesting an abundance of small translational and rotational displacements that occur simultaneously. This is further reflected in the probability for a particle to be found in each quadrant above and below the respective ensemble averages. Therefore, we see that the same correlation found in the dense fluid, where only a correlation between small displacements can be observed, extends into the crystal. Fig 5.5b) shows a typical particle rotational trajectory projected onto a unit sphere, which is similar to that found in the fluid as the particle is rotating freely. The distribution of Δr_i and $\Delta\theta_i$ is shown for the same particle in 5.5c). Here we can identify a majority of displacements in the lower left hand quadrant, again implying this correlation between small steps can be replicated by each particle.

We next examine whether the slight correlation in small rotational and translation steps again leads to a coupling in the time-averaged behaviour. Fig 5.6a) and b) show the single-particle MSD and MSAD, $\langle \Delta r_i^2(\tau) \rangle$ and $\langle \Delta\theta_i^2(\tau) \rangle$, respectively. A striking

disparity is observable as for all particles $\langle \Delta r_i^2(\tau) \rangle$ is plateaued while $\langle \Delta \theta_i^2(\tau) \rangle$ remains diffusive. However, Fig 5.6c) shows a plot of $\langle \Delta r_i^2(\tau) \rangle$ and $\langle \Delta \theta_i^2(\tau) \rangle$ at $\tau = 11.8$ where a distinct skew is observable again showing, similarly to the fluid phase, the time averaged dynamics show a degree of correlation at short times. From the percentage of particles in each quadrant we find that 68% sit in the lower left, both translationally and rotationally slow, or upper right, both translationally and rotationally fast. This is again evident of a degree of correlation in the time averaged behaviour at short times.

Examining the distribution at longer time $\tau = 94.4s$, as shown in Fig 5.6d), we see the spread of the distribution increase for $\langle \Delta \theta_i^2(\tau) \rangle$ while the spread of $\langle \Delta r_i^2(\tau) \rangle$ is largely unchanged. Therefore, the particles are free to rotate while translationally confined on the crystalline lattice. At longer τ, the distribution is more evenly spread across the four quadrants although again the majority sit in the lower left hand quadrant. The distribution is less evenly spread than the similar plot in Fig 5.4d) for the dense fluid phase. This can be rationalised by considering our system is not a

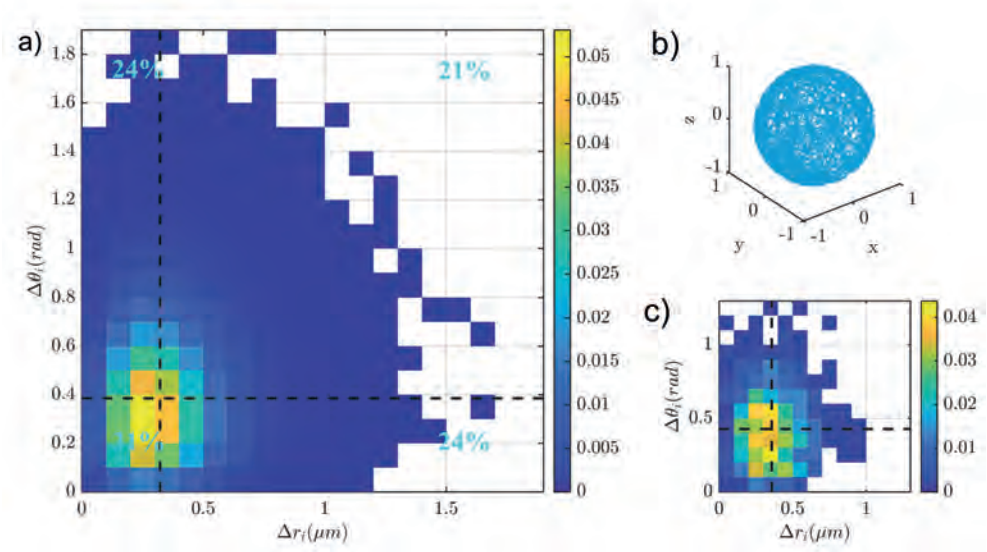

Figure 5.5: a) Single-particle translational displacement between each frame (Δr_i) and single-particle rotational displacement between each frame ($\Delta \theta_i$) for $\phi = 0.54$. Dashed line indicates the ensemble averages for both axes. Colour bar indicates the normalised probability. b) Typical rotational particle trajectory as unit orientation projected onto unit sphere. c) Individual translational displacement between each frame (Δr_i) and rotational displacement between each frame ($\Delta \theta_i$) for particle shown in b).

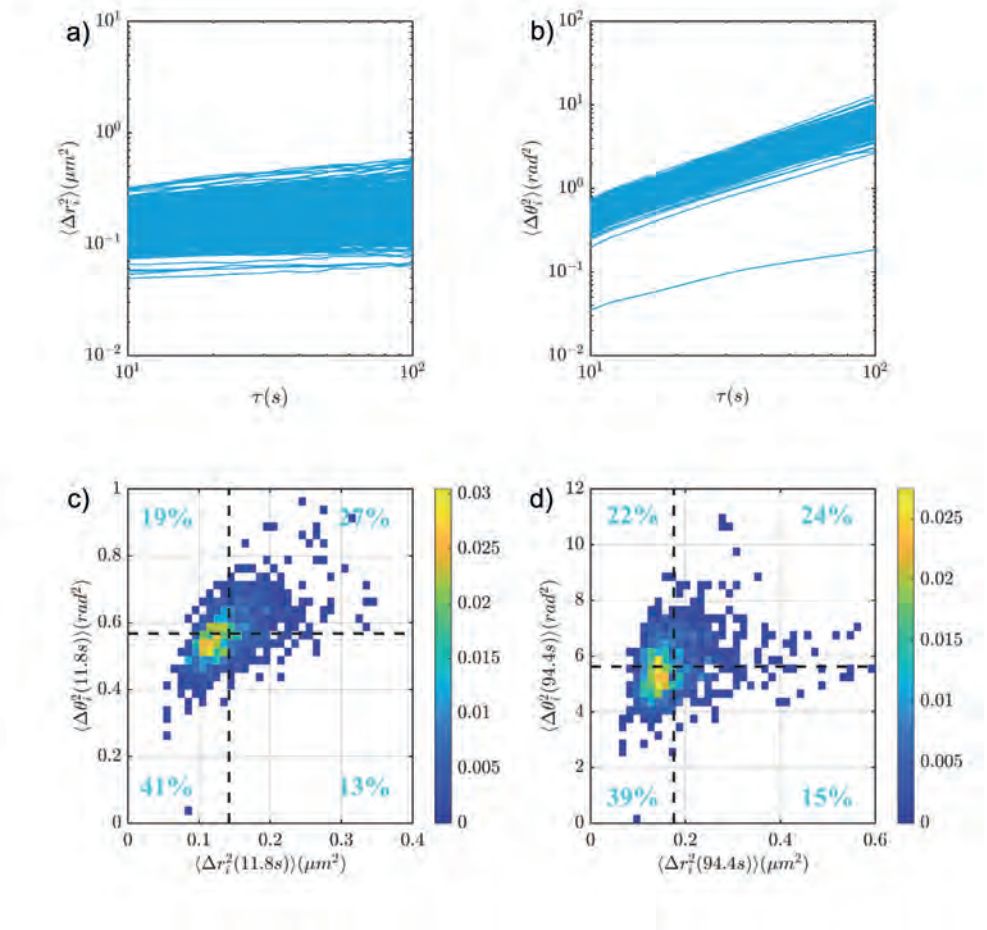

Figure 5.6: Single-particle MSDs for $\phi = 0.54$ b) Single-particle MSADs for $\phi = 0.54$ c) 2D histogram of $\langle \Delta r_i^2(\tau) \rangle$ and $\langle \Delta \theta_i^2(\tau) \rangle$ for $\tau = 11.8s$, ensemble averaged mean is shown in black for both. d) 2D histogram of $\langle \Delta r_i^2(\tau) \rangle$ and $\langle \Delta \theta_i^2(\tau) \rangle$ for $\tau = 94.4s$, ensemble averaged mean is shown in black for both.

homogeneous crystal as several grains are identifiable in each layer. This is also evident from the presence of a small number of anomalously fast particles in the distribution which we attribute this to particles that sit at the boundary between two grains and have a greater degree of mobility [43]. As such the translational dynamics of the system are non-gaussian as the individual particle environments never average out to a continuum. Therefore we see a persistent skew in the plot of $\langle \Delta r_i^2(\tau) \rangle$ and $\langle \Delta \theta_i^2(\tau) \rangle$ at long τ.

5.3.3 Glass

We finally turn to the second sample with a shorter gravitational length, $\xi_g = 0.25\mu m$, which results in an amorphous, glassy sediment as shown in Fig 5.1. We begin by examining the dynamics at an ensemble-averaged level. Fig 5.7a) shows the ensemble averaged MSD for a range of ϕ. At low ϕ the MSD is diffusive, but as ϕ increases and particles begin to experience caging again a transient plateau is observed. Notably, in this sample only $\phi < 0.55$ show a return to diffusive behaviour at long lag times, above this threshold the translational dynamics are arrested over the course of the experiment and extraction of D_T is not possible. Fig 5.7b) shows the accompanying MSAD which, similar to the crystal-fluid sample, remains diffusive at all ϕ investigated over the whole experimental timeframe.

We extract D_T and D_R which is shown in Fig 5.7c) where the data from the crystal-fluid sample is shown in grey. D_T continues to decline steeply at higher ϕ while D_R shows only a small decrease. Furthermore in Fig 5.7d) we show the ratio given in Eq 5.5 which shows further decrease at higher ϕ, showing a stronger decoupling between D_T and D_R. Again we can extract η_T and η_R from D_T and D_R as shown in Fig 5.7d) where this is added to the values from the crystal-fluid sediment to show the behaviour across all phases. We see the values extracted from the glassy sample continue the trend established in the crystal-fluid sample as with increasing ϕ the separation between η_T and η_R increases, as η_R shows only a small increase and η_T increases by several orders of magnitude. This reiterates that as ϕ increases towards the glass transition D_T and D_R decouple as translational and rotational motion is coupled to different η.

Next, we examine the translational and rotational dynamics at the single-particle level. First, we explore the coupling between individual translational and rotational displacements. Fig 5.8a) shows a 2D histogram of the single-particle rotational, Δr_i, and translational displacements, $\Delta\theta_i$, between each frame. Again, a skewed distribution is produced with an abundance of points sitting in the lower left quadrant. However unlike the crystal or the fluid we cannot extract a typical rotational particle trajectory as we identify different types of rotational motion ranging from rotationally free to partially arrested to fully arrested, as shown in Fig 5.8b). These rotationally slow particles arise due to the increased interparticle friction the particles experience in the glass as the particles are in close proximity than in the crystal or fluid [34]. For each type of rotational trajectory we show the correlation between the individual translational and rotational steps in Fig 5.8c). As rotational mobility decreases we see the maxima in

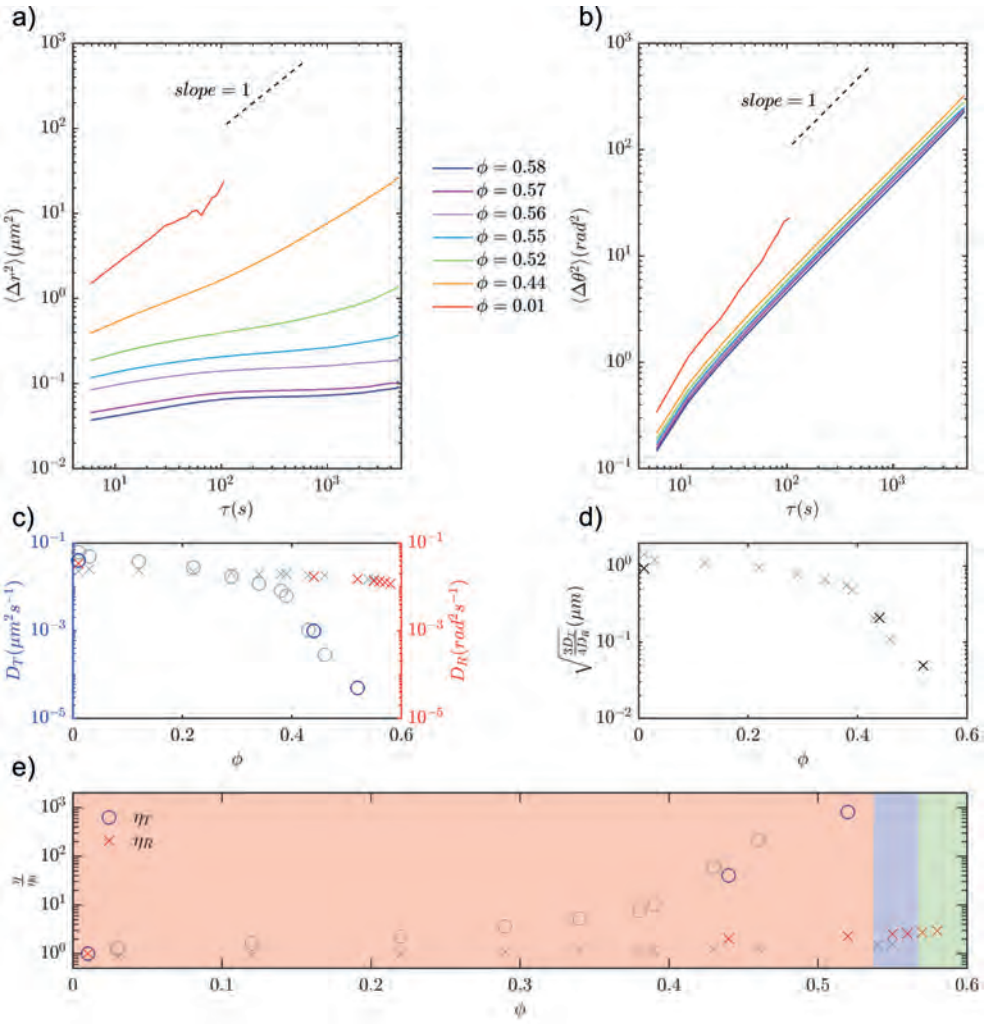

Figure 5.7: a) MSD for a range of ϕ recorded in the sample with $\xi_g = 0.25\mu m$, in the glass and fluid phases and b) corresponding MSAD for the same ϕ c) D_T and D_R as a function of ϕ. Data shown in Fig 5.2 is shown in grey. d). Ratio of $\sqrt{3D_T/4D_R}$ as a function of ϕ. Data shown in Fig 5.2 is shown in grey. e) The viscosities, η_T and η_R, as a function of ϕ. Note that extraction of D_T above 0.52 is not possible as diffusive behaviour is not reached over the course of the experiment. Shading denotes the phase; red is the fluid phase, blue the crystal phase and green the glass phase. Data shown in Fig 5.2 is shown in grey.

the probability sharpen and remain in the lower left corner. Therefore in the glass we continue the trend we establish in the crystal and fluid where small rotational and small translational steps are coupled, but furthermore this trend is continued by particles of different rotational mobility.

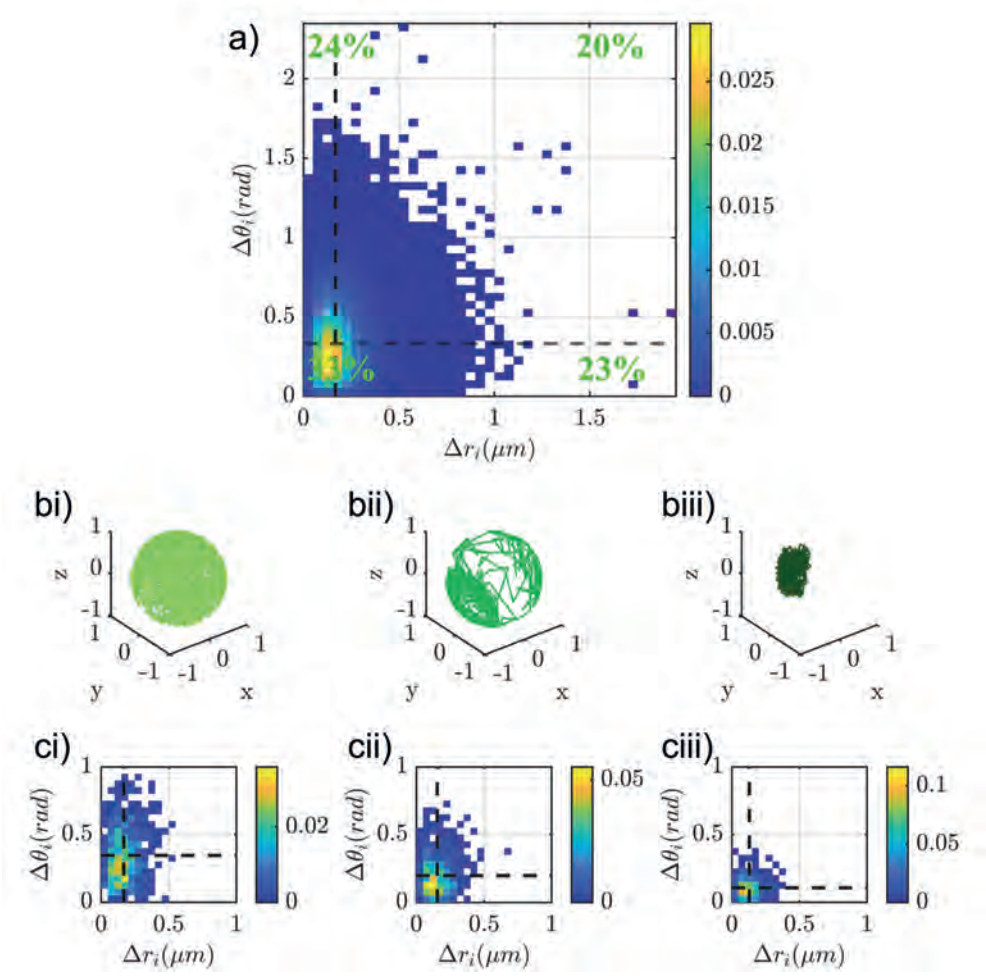

Figure 5.8: a) Single-particle translational displacement between each frame (Δr_i) and single-particle rotational displacement between each frame ($\Delta\theta_i$) for $\phi = 0.58$. Colourbar shows the normalised probability. b) Rotational trajectory projected onto unit sphere for particle characterised as i) rotationally free, ii) partially rotationally arrested and ii) rotationally arrested. b) 2D histogram of Δr_i and $\Delta\theta_i$ for particle characterised as i) rotationally free, ii) partially rotationally arrested and ii) rotationally arrested.

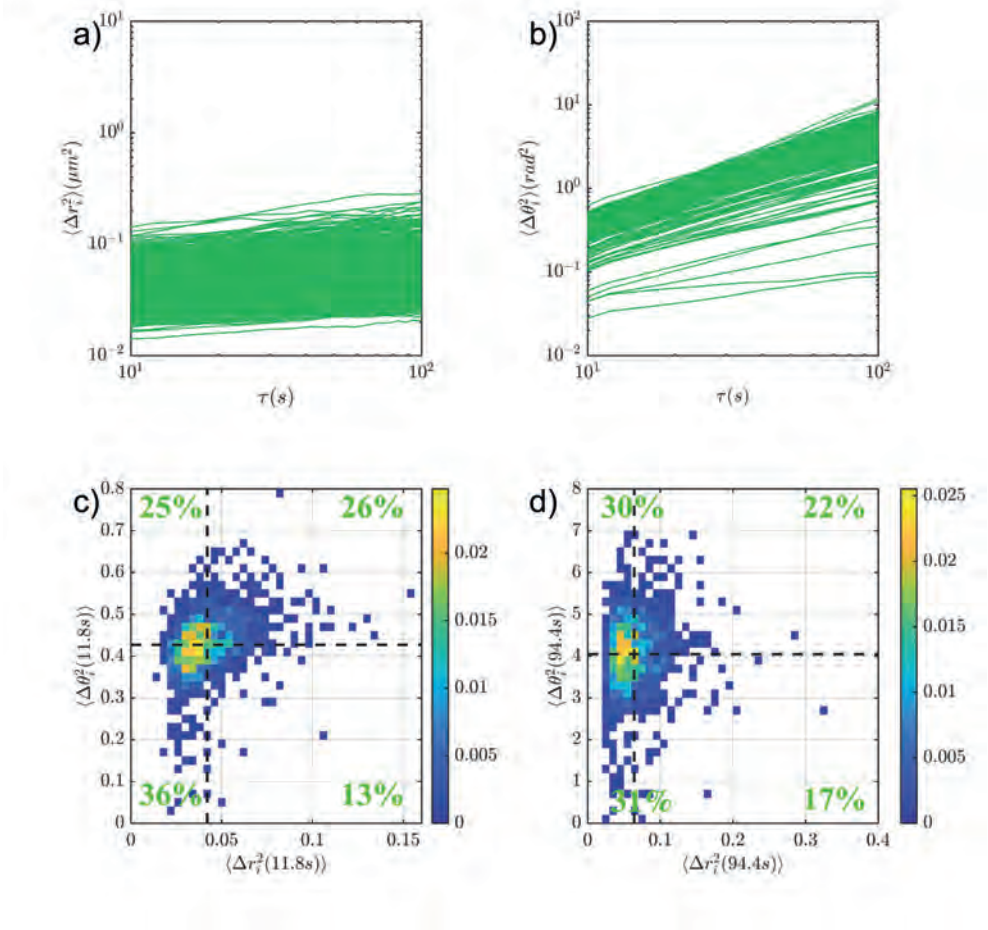

Figure 5.9: Single-particle MSDs for $\phi = 0.58$ b) Single-particle MSADs for $\phi = 0.58$ c) 2D histogram of $\langle \Delta r_i^2(\tau) \rangle$ and $\langle \Delta \theta_i^2(\tau) \rangle$ for $\tau = 11.8s$, ensemble averaged mean is shown in black for both. d) 2D histogram of $\langle \Delta r_i^2(\tau) \rangle$ and $\langle \Delta \theta_i^2(\tau) \rangle$ for $\tau = 94.4s$, ensemble averaged mean is shown in black for both.

We next examine the time-averaged behaviour. Fig 5.9a) and b) show the single-particle MSAD and MSD where more rotationally arrest particles are observable with a MSAD below the bulk of the particles. However, in the histogram of $\langle \Delta r_i^2(\tau) \rangle$ and $\langle \Delta \theta_i^2(\tau) \rangle$ at $\tau = 11.8$, shown in Fig 5.9c), we see a difference in the spread of the data compared to the fluid and crystal phases. Similarly to the previous phases the plot shows a majority of the particles in the lower left quadrant, both rotationally and

translationally slow. However there is a roughly equal population in the upper two quadrants. It is also notable that the distribution is different in shape compared to the same plot for the fluid or the crystal phase. The histogram is notably more extended towards slower rotational dynamics which gives the distribution a less 'linear' and more 'curved' shape. The abundance of points in the lower left hand quadrant demonstrates there is a correlation between the $\langle \Delta r_i^2(\tau) \rangle$ and $\langle \Delta \theta_i^2(\tau) \rangle$ at short τ.

At a longer τ in Fig 5.9c) we see the distribution does not become evenly spread around the four quadrants and the distribution is still notably skewed. We note that both translational and rotational dynamics at heterogenous in this phase. Translational dynamics develop a *fast* subpopulation in the glass phase [18, 19] while we have shown in the previous Chapter that rotational dynamics develop a *slow* subpopulation. The persistent skew in the data at long τ is evident that neither translational or rotational dynamics have become Gaussian at this τ, and therefore for neither can the environment each particle experiences during rotational or translational dynamics be approximated as an average across the population. Although we observed similar behaviour for the crystal here we see the impact of *both* translational and rotational dynamics being non-Gaussian. The impact of the slow rotational subpopulation extends the distribution, at both short and long τ more into the lower left hand quadrant. This changes the shape of the distribution to give it a less 'linear' and more 'curved' shape. Interparticle friction therefore changes the nature of the correlation between single-particle translational and rotational dynamics in the glass phase.

5.3.4 Correlation Coefficient

We further analyse and compare the change in the correlation between $\langle \Delta r_i^2(\tau) \rangle$ and $\langle \Delta \theta_i^2(\tau) \rangle$ across the fluid, crystal and glass phases by calculating the correlation coefficient, C, defined as;

$$C = \frac{Cov(\langle \Delta(r_i^2) \rangle, \langle \Delta(\theta_i^2) \rangle}{\sigma_r \sigma_\theta}, \tag{5.6}$$

where Cov is the covariance between $\langle \Delta(r_i^2) \rangle$ and $\langle \Delta(\theta_i^2) \rangle$ and σ_r and σ_θ are the standard deviation in $\langle \Delta(r_i^2) \rangle$ and $\langle \Delta(\theta_i^2) \rangle$, respectively. As shown in Fig 5.10 a), in the fluid phase as ϕ increases C increase until it reaches a maximum in the crystal phase before decreasing inside the glass. This decrease inside the glass phase is also

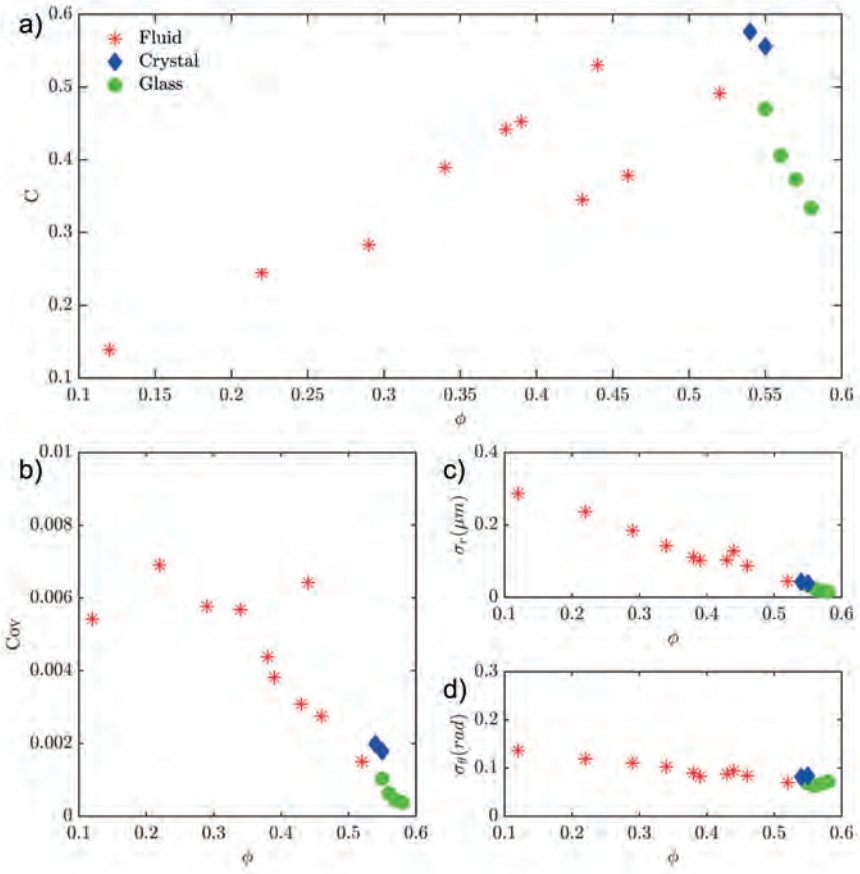

Figure 5.10: a) Correlation coefficient, C, calculated from Eq 5.6 for a range of ϕ spanning the fluid phase (shown in red), the crystalline phase (shown in blue) and the glassy phase (shown in green), at $\tau = 11.8s$. b) Plot of the covariance, Cov as a function of ϕ. c) Plot of the standard deviation in $\langle \Delta(r_i^2) \rangle$, σ_r as a function of ϕ d) Plot of the standard deviation in $\langle \Delta(\theta_i^2) \rangle$, σ_θ as a function of ϕ. Note that below $\phi = 0.12$ there was not sufficient statistics to measure these quantities.

found in C for individual particle displacements approaching ϕ_G [15]. This trend can be explained by examining the contributions to C. Fig 5.10b) shows how Cov changes with ϕ where we observe a steady decrease as ϕ increases. This is expected as the spread of the data decreases as ϕ increases which leads to a decrease in Cov. Fig 5.10c) shows a plot of σ_r and σ_θ against ϕ where a similar decrease with increasing ϕ is also observable.

However, we note that as ϕ increases σ_r decreases more rapidly than σ_θ. In the fluid and crystal phases the decrease in σ_r and σ_θ overcomes the decrease in Cov leading to an increase in C. Upon entering the glass phase although σ_r continues to decrease and σ_θ remains roughly constant, the Cov continues to decrease leading to a decrease in C. We attribute part of the decrease in Cov to the development of the rotationally slow subpopulation which causes a less linear correlation between $\langle\Delta(r_i^2)\rangle$ and $\langle\Delta(\theta_i^2)\rangle$. Therefore upon entering the glass phase the nature of the coupling between translational and rotational dynamics changes due to the impact of interparticle friction.

5.4 Conclusion

In conclusion we have studied the coupling and correlation between translational and rotational dynamics in the colloidal fluid, crystal and glass. We observe that for dense fluids D_T and D_R decouple as ϕ increases as translational and rotational dynamics become coupled at different η, with only translational dynamics experiencing an increase due to the presence of other particles in the sample. We demonstrate that in the fluid, crystal and glass phases only small translational and rotational displacements between each frame are coupled. However the magnitude of the MSD and MSAD at short lag times shows a correlations that disappears at longer lag times once the ensemble averaged dynamics become Gaussian. In the glass phase rotational dynamics become more heterogenous and we can characterise different particle behaviours based on different rotational mobility. Particles of different rotational mobility also display the same coupling of small translational and rotational steps. We also show that the single-particle time averaged behaviour shows a degree of correlation at short times for all phase but the shape of this distribution changes for the glass phase due to the presence of a subpopulation of rotationally slow particles. We quantify these observations using the correlation coefficient, C, which increases with ϕ in the fluid phase to reach a maximum in the crystal before decreasing in the glass phase. We attribute this decrease to the presence of a rotationally slow subpopulation which results in a lower covariance and a large enough σ_θ to cause an overall decrease in C. We demonstrate that although translational and rotational dynamics have been described as decoupled at the ensemble averaged level once the statistics of the whole population are know a clear correlation is observable in the fluid, crystal and glass phase.

5.5 Supplementary information

5.5.1 Materials

3-(trimethoxysilyl)propyl methacrylate (TPM, ≥97%, Sigma Aldrich), ammonium hydroxide solution (28% vol. NH_3 in H_2O, Alfa Aesar), azobisisobutyronitrile (AIBN, BDH, UK), Cyanine3 NHS Ester (Lumiprobe), BDP NHS Ester (Lumiprobe), Chloroform ($CHCl_3$, Fischer Scientific), 3-aminopropyl trimethoxysilane (APS, Sigma Aldrich), 4-aminostryene (4-AS, Sigma Aldrich), acetone (Sigma Aldrich), Sodium Hydroxide (NaOH, Sigma Aldrich), Hydrochloric Acid (HCl, Sigma Aldrich), Pluronic® F-108 (F-108, Sigma Aldrich), trichloroethylene (TCE, ≥99.5%, Sigma Aldrich), 1,2,3,4-tetrahydronaphthalene (TTL, anhydrous, 99%, Sigma Aldrich) and tetrachloroethylene (PERC, 99%, Alfa Aesar) were used as received. A polyisobutylene succinic anhydride stabilizer, OLOA 11000, was provided by Eric Dufresne and Azelis. Double-distilled water was sourced from an PURELABS Chorus 1 ultrapure water unit.

5.5.2 Particle Synthesis

We synthesise OCULI particles by following the synthesis protocol developed Ref. [34]. 3-trimethoxysilylpropyl methacrylate (TPM) oil is hydrolysed under acidic conditions by diluting 2ml TPM in 20ml 0.05mM HCl and stirring for 1 hour. 4ml of hydrolysed TPM (hTPM) was diluted in 21ml 0.5mM HCl before 25ml 0.028% NH_4OH is added which triggers rapid condensation followed by nucleation and growth of monodiperse droplets. These droplets can were labelled with BDP-FL NHS ester (1mg/ml $CHCl_3$ functionalised with APS, [34]) and crosslinked to form hardened TPM microspheres, referred to as the 'eye' of the particles. During cross-linking a spatulaful of AIBN was added to the suspension of droplets before heating to $80°C$ for 3 hours. The particles were washed by repeated centrifugation at 1000g for 10 min and responded to a total volume of 10ml. 2ml of the eye particles were added to a vial of 5ml 0.028% NH_4OH before $150\mu l$ hTPM was added. The resulting solution was tumbled for 30 min. This created a thin layer of liquid TPM on each particle to favour subsequent growth of this layer as opposed to secondary nucleation. The eye solution was then diluted in 20ml 0.028% NH_4OH and stirred while hTPM was dripped into the flask at a rate of $100\mu l/min$. The hydrolysed TPM wets onto the surface of these particles, eventually engulfing the eye inside a droplet. However, due to interface pinning the eye is held at the interface inside the droplet. 5ml of 5% wt F108 was added to the suspension before the droplets were labelled with Cyanine 3 NHS ester (1mg/ml in

acetone functionalised with 4-AS [35]). The particles were then crosslinked using the same procedure described previously. This outer shell is referred to as the 'body' of the OCULI. To add a non-flourescent shell around the particle, first TPM lobes are created on the surface of the particle. The surfactant, F108, added during the synthesis of the body alters the wetting angle of liquid TPM on crosslinked TPM. Therefore, addition of hTPM to the OCULI particles results in well defined lobes. Once these lobes are cross-linked more hydrolysed TPM is used to wet in between them to return the particle to a spherical shape at which point the liquid TPM is again cross-linked. If both the TPM that forms the lobe and the TPM used to wet in between them is left without a floursecent label both components show as a single non-flouresecent shell around the particle.

5.5.3 Confocal Microscopy

Each system was imaged with two-channel 3D confocal laser scanning microscope; Olympus IX73 inverted microscope, 60× Olympus Plan Apochromat oil immersion objective (NA = 1.42). High speed imaging was achieved by Thorlabs confocal 12kHz resonant scanner and an objective-mounted piezoelectric Z-stage (Physik Instrumente). A total image volume of $102.4\times102.4\times50.2\mu m^3$ was recorded in 5.9s (800 frames over 90 minutes). Simultaneous illumination of the sample with laser of wavelength 488nm and 532nm allows near simultaneous imaging of both components of the OCULI particle. To capture the whole density profile, 3D stacks were taken at two different heights within each sample: between 10 to 60 μm and between 50 to 100 μm for the glassy sediment and between 10 to 60 μm and between 60 to 110 μm for the crystal-fluid sample. The data is averaged over 3 independent datasets.

5.5.4 Particle Sizing

The particles are sized from SEM microscopy to give a radius of 1.43 μm and polydispersity of 2.30%. To size particles in solution an ultra dilute suspension of $\phi \approx 0.01$ is prepared in a density matching suspension of tetralin:trichloroethylene:tetrachloroethylene [35]. The translational dynamics are recorded as the MSD given by Eq 4.1 and the translational diffusion coefficient is extracted by fitting this data with $\langle \Delta r^2 \rangle = 6D_T\tau$ (Fig 5.11a)) where,

$$D_T = \frac{k_B T}{6\pi\eta R} \tag{5.7}$$

Using this we extract $D_T = 0.0554 \times 10^{-14} m^2 s^{-1}$ which results in a Brownian time of $\tau_T = 28.9s$. The rotational dynamics are recorded as the MSAD and the autocorrelation function, $C(\tau) = \langle u_t \cdot u_{t+\tau} \rangle$. From both D_R can be extracted from both measures by fitting $\langle \Delta\theta^2 \rangle = 4D_R\tau$ and $C(\tau) = \exp(\frac{\tau}{2D_R})$ respectively (Fig 5.11b) and c)). In both cases D_R is given by,

$$D_R = \frac{k_B T}{8\pi\eta R^3}, \tag{5.8}$$

and the particle size can be extracted using the ratio,

$$R = \sqrt{\frac{3D_T}{4D_R}}. \tag{5.9}$$

We note a small difference in the D_R extracted in from the $C(\tau)$ and MSAD which give values of $0.0172 s^{-1}$ and $0.0161 rad^2 s^{-1}$. This results in a value for R of $1.55\mu m$ using the D_R extracted from $C(\tau)$ and of $1.61\mu m$ using the D_R extracted from the MSAD. Both of these values are larger than the radius recorded from SEM due to the shrinkage of particles in the vacuum in the SEM. A radius of $1.55\mu m$ is used for the calculation of ϕ. We also extract the rotational relaxation time defined as $\tau_R = \frac{1}{2D_R}$ which gives $\tau_R = 29.1s$ and $\tau_R = 31.1s$ from the $C(\tau)$ and MSAD respectively.

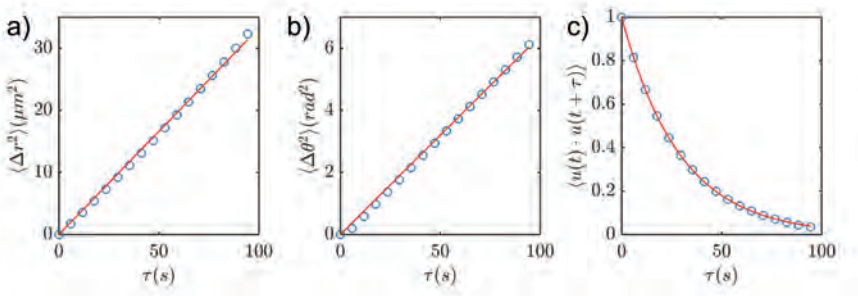

Figure 5.11: a) Plot of MSD against τ for sample of $\phi = 0.01$. b) MSAD against τ for sample of $\phi = 0.01$. c) $C(\tau)$ against τ for sample of $\phi = 0.01$.

5.5.5 Particle Tracking

Location of the particle positions and orientations were extracted using the method outlined in ref [34]. A small number of particles $< 1\%$ fuse together during the synthesis. These are eliminated from our analysis by removing particles with a nearest neighbour distance $< 2.6\mu m$. Furthermore after particle tracking we find a small number of particles are only tracked for 100 frames or less. These particles are neglected from the single-particle analysis to prevent counting particles twice [34].

5.5.6 Rotational Displacement

Rotational displacement was calculated in line with previous studies [44]. First we define the rotational trajectory between each frame as

$$\psi(t_2) = \hat{\omega} \cdot \alpha, \tag{5.10}$$

where $\hat{\omega}$ is the axis of rotation between frames, $(\hat{\omega} = \hat{u}(t_1) \times \hat{u}(t_2))$, and α is the angle of rotation, $(\alpha = \cos^{-1}(\hat{u}(t_1) \cdot \hat{u}(t_2)))$. The sum of these displacement between each frame is evaluated as the integral,

$$\theta(\tau) = \int_1^{t_2} \psi(t) dt. \tag{5.11}$$

The resulting the rotational trajectory, θ, can be used as a direct analogue to the translational trajectory.

5.5.7 Extraction of Diffusion Coefficients

In this experiment only the long-time diffusion coefficients were accessible. The long-time D_T and D_R were extracted from the long-time limit of the MSD and MSAD respectively, only fits with rsquared>0.9 were accepted for analysis.

5.5.8 Acknowledgements

All particle synthesis, imaging and analysis was carried out by R. A. Crothers. We thank B. van der Meer for useful discussions.

5.6 Bibliography

[1] H. Sillescu. Heterogeneity at the glass transition: a review. *J. Non-Cryst. Solids*, 243(2-3):81–108, 1999.

[2] C. A. Angell. Liquid fragility and the glass transition in water and aqueous solutions. *Chem. Rev*, 102(8):2627–2650, 2002.

[3] E. R Weeks. Introduction to the colloidal glass transition. *ACS Macro Lett.*, 6(1):27–34, 2017.

[4] A. Einstein. *Investigations on the Theory of the Brownian Movement*. Courier Corporation, 1956.

[5] P. J. W. Debye. *Polar Molecules*. Dover Publications, 1929.

[6] M. G. Mazza, N. Giovambattista, H. E. Stanley, and F. W. Starr. Connection of translational and rotational dynamical heterogeneities with the breakdown of the stokes-einstein and stokes-einstein-debye relations in water. *Phys. Rev. E*, 76:031203, 2007.

[7] S. K. Kumar, G. Szamel, and J. F. Douglas. Nature of the breakdown in the stokes-einstein relationship in a hard sphere fluid. *J. Chem. Phys.*, 124(21), 2006.

[8] S-H Chong and W. Kob. Coupling and decoupling between translational and rotational dynamics in a supercooled molecular liquid. *Phys. Rev. Lett.*, 102(2):025702, 2009.

[9] M. T. Cicerone and M. D. Ediger. Enhanced translation of probe molecules in supercooled o-terphenyl: Signature of spatially heterogeneous dynamics? *J. Chem. Phys.*, 104(18):7210–7218, 1996.

[10] T. G. Lombardo, P. G. Debenedetti, and F. H. Stillinger. Computational probes of molecular motion in the lewis-wahnström model for ortho-terphenyl. *J. Chem. Phys.*, 125(17), 2006.

[11] I. Chang, F. Fujara, B. Geil, G. Heuberger, T. Mangel, and H. Sillescu.

Translational and rotational molecular motion in supercooled liquids studied by nmr and forced rayleigh scattering. *J. Non-Cryst. Solids*, 172-174:248–255, 1994.

[12] K. V. Edmond, M. T. Elsesser, G. L. Hunter, D. J. Pine, and E. R. Weeks. Decoupling of rotational and translational diffusion in supercooled colloidal fluids. *Proc. Natl. Acad. Sci. U.S.A*, 109:17891–17896, 2012.

[13] S. Vivek and E. R. Weeks. Decoupling of translational and rotational diffusion in quasi-2d colloidal fluids. *J. Chem. Phys.*, 147, 2017.

[14] B. Ilhan, F. Mugele, and M. H.G. Duits. Roughness induced rotational slowdown near the colloidal glass transition. *J. Colloid Interface Sci.*, 607:1709–1716, 2022.

[15] M. Kim, S. M. Anthony, S. C. Bae, and S. Granick. Colloidal rotation near the colloidal glass transition. *J. Chem. Phys.*, 135, 2011.

[16] S. Schütter, J. Roller, A. Kick, J-M. Meijer, and A. Zumbusch. Real-space imaging of translational and rotational dynamics of hard spheres from the fluid to the crystal. *Soft Matter*, 13:8240–8249, 2017.

[17] J. Geiger, N. Grimm, M. Fuchs, and A. Zumbusch. Decoupling of rotation and translation at the colloidal glass transition. *J. Chem. Phys.*, 161(1), 2024.

[18] W. K. Kegel and A. van Blaaderen. Direct observation of dynamical heterogeneities in colloidal hard-sphere suspensions. *Science*, 287(5451):290–293, 2000.

[19] E. R. Weeks, J. C. Crocker, A. C. Levitt, A. Schofield, and D. A .Weitz. Three-dimensional direct imaging of structural relaxation near the colloidal glass transition. *Mol. Biol. Cell*, 128:2847, 2000.

[20] L. Berthier, G. Biroli, J-P. Bouchaud, L. Cipelletti, and W. van Saarloos. *Dynamical heterogeneities in glasses, colloids, and granular media*, volume 150. OUP Oxford, 2011.

[21] L. Chu, K. Xu, R. Graf, Z-C. Yan, J. Li, and Y-F. Yao. Dynamic heterogeneity in homogeneous polymer melts. *Soft matter*, 17(25):6081–6087, 2021.

[22] J. Fan, H. Emamy, A. Chremos, J. F. Douglas, and F. W. Starr. Dynamic heterogeneity and collective motion in star polymer melts. *J. Chem. Phys.*, 152(5), 2020.

[23] W. Zhao, H. Huo, Z-Y. Sun, and Z-Y. Lu. Data-driven analysis of dynamical heterogeneity in polymer melts near surfaces. *Comput. Mater. Sci.*, 235:112811, 2024.

[24] H. B. Yu, W. H. Wang, H. Y. Bai, and K. Samwer. The β-relaxation in metallic glasses. *Natl. Sci. Rev.*, 1(3):429–461, 2014.

[25] W. C. K. Poon. Colloids as big atoms. *Science*, 304(5672):830–831, 2004.

[26] A. L. Thorneywork, J. L. Abbott, D. G. A. L. Aarts, and R P. A. Dullens. Two-dimensional melting of colloidal hard spheres. *Phys. Rev. Lett.*, 118(15):158001, 2017.

[27] Luis G. MacDowell. Surface tension of bulky colloids, capillarity under gravity, and the microscopic origin of the kardar-parisi-zhang equation. *Phys. Rev. E*, 108:L022801, 2023.

[28] K. Schätzel and B. J. Ackerson. Density fluctuations during crystallization of colloids. *Phys. Rev. E*, 48:3766–3777, 1993.

[29] B. O'Malley and I. Snook. Crystal nucleation in the hard sphere system. *Phys. Rev. Lett.*, 90:085702, 2003.

[30] V. W. A. de Villeneuve, R. P. A. Dullens, D. G. A. L. Aarts, E. Groeneveld, J. H. Scherff, W. K. Kegel, and H. N. W. Lekkerkerker. Colloidal hard-sphere crystal growth frustrated by large spherical impurities. *Science*, 309(5738):1231–1233, 2005.

[31] J. D. Hutchinson, F. A. Lavergne, and R. P. A. Dullens. Crystallization and grain growth in impurity-doped colloidal polycrystals. *Phys. Rev. Mater.*, 6(7):075604, 2022.

[32] U. Gasser, E. R. Weeks, A. Schofield, P. N. Pusey, and D. A. Weitz.

Real-space imaging of nucleation and growth in colloidal crystallization. *Science*, 292(5515):258–262, 2001.

[33] Q-Z. Zou, Z-W. Li, Y-L. Zhu, and Z-Y. Sun. Coupling and decoupling between translational and rotational dynamics in supercooled monodisperse soft janus particles. *Soft Matter*, 15(16):3343–3352, 2019.

[34] T. Yanagishima, Y. Liu, H. Tanaka, and R. P.A. Dullens. Particle-level visualization of hydrodynamic and frictional couplings in dense suspensions of spherical colloids. *Phys. Rev. X*, 11, 2021.

[35] R. A Crothers, N. H P Orr, B. van der Meer, R. P. A. Dullens, and T. Yanagishima. Characterization and optimization of fluorescent organosilica colloids for 3d confocal microscopy prepared under "zero-flow" conditions. *Langmuir*, 39(15):5306–5314, 2023.

[36] Y. Liu, T. Yanagishima, A. Curran, K. V. Edmond, S. Sacanna, and R. P.A. Dullens. Colloidal organosilica spheres for three-dimensional confocal microscopy. *Langmuir*, 35, 2019.

[37] N. Fernandez, R. Mani, D. Rinaldi, D. Kadau, M. Mosquet, H. Lombois-Burger, J. Cayer-Barrioz, H. J. Herrmann, N. D Spencer, and L. Isa. Microscopic mechanism for shear thickening of non-brownian suspensions. *Phys. Rev. Lett.*, 111(10):108301, 2013.

[38] A. Singh, C. Ness, R. Seto, J. J. de Pablo, and H. M. Jaeger. Shear thickening and jamming of dense suspensions: the "roll" of friction. *Phys. Rev. Lett.*, 124(24):248005, 2020.

[39] B. M. Guy, M. Hermes, and W. C. K. Poon. Towards a unified description of the rheology of hard-particle suspensions. *Phys. Rev. Lett.*, 115(8):088304, 2015.

[40] D. R Foss and J. F Brady. Brownian dynamics simulation of hard-sphere colloidal dispersions. *J. Rheol.*, 44(3):629–651, 2000.

[41] J. F Brady, A. S Khair, and M.j Swaroop. On the bulk viscosity of suspensions. *J. Fluid Mech.*, 554:109–123, 2006.

[42] B. van der Meer, T. Yanagishima, and R. P. A. Dullens. Attraction-enhanced emergence of friction in colloidal matter. *Phys. Rev. Lett.*, 134:078202, 2025.

[43] T. O. E. Skinner, D. G. A. L. Aarts, and R. P. A. Dullens. Supercooled dynamics of grain boundary particles in two-dimensional colloidal crystals. *J. Chem. Phys.*, 135(12):124711, 2011.

[44] G. L. Hunter, M. T. Edmond, K. V .and Elsesser, and E. R. Weeks. Tracking rotational diffusion of colloidal clusters. *Opt. Express*, 19(18):17189–17202, 2011.

Chapter 6

Revealing the Role of Polydispersity in the Dynamics Across the Colloidal Glass Transition

Polydispersity remains unexploited as a way to control the phase behaviour of colloidal microspheres. This is due to the difficulty of controlling it during particle synthesis. In this chapter we demonstrate how fractional stirring can be used to systematically vary the polydispersity of TPM microspheres from 5-30%, to within an error of 6%. We use this method to develop two particle systems for use with confocal microscopy, both of which allow for the determination of individual particle size from a single CLSM image. First, we create controllably polydisperse (5-10%) OCULI particles which allow for the direct observation of both the translational and rotational dynamics of every particle within the system. Secondly, we demonstrate another particle system that allows the observation of the translational dynamics only but at much larger polydispersities, up to 19%. We utilise both systems to investigate the dynamics across the colloidal glass transition as a function of individual particle size.

6.1 Introduction

Colloidal microspheres have been long used as a model for the phase behaviour of atomic and molecular systems [1]. Their length, (μm), and timescales,(s), combined with the ability to observe different phases by simply altering the concentration, has lead to key insights into particle behaviour at phase transitions such as the direct observation of dynamic heterogeneities at the glass transition [2, 3], as well as direct study of the nucleation and growth of colloidal crystals [4–6]. Recent advances in colloidal synthesis have allowed the exploration of phase behaviour beyond simple microspheres. An exotic variety of colloidal particles now exists which exploit shape, interactions or other physical properties as tools to alter the phase behaviour [7–10]. For instance introducing curvature to a rod-like colloidal particle vastly increases the richness of the phase behaviour [7, 11–16]. Even for simple microspheres adding complex interactions creates a more complex phase diagram [10, 17].

One parameter that is rarely used to tune the phase behaviour of colloidal microspheres is polydispersity. Polydispersity is often treated as a nuisance in colloidal systems, but it can be used as a tool to prevent crystallisation [18–21]. In the study of glasses, this is normally achieved by using binary suspensions to suppress crystallisation [18, 20–23]. However, creating an intrinsically polydisperse system by tuning the polydispersity of a single batch of colloidal particles, described by a single size distribution, is difficult to achieve in most conventional particle syntheses. The most common particle synthesis for colloidal microspheres typically produces particles of polydispersity lower than 6%, the threshold for 3D crystallisation [24]. Very few synthetic paths to truly polydisperse particle systems, that can be described by a single size distribution, exist.

The interest in using polydispersity as a tool to alter the behaviour has two key motivating factors. Firstly, polydisperse suspensions are closer to the particle suspensions found in nature. Mud, clay, and cements are all typically polydisperse particle suspensions. Creating a model particle system for these systems allows a new way to study their dynamics [25, 26]. Secondly, controlled polydispersity allows a controlled transition from the crystal to the glass. The glass transition has long been a focus of scientific interest. However, most experimental studies explore a one-component particle suspension of a single polydispersity or a binary system of a single size ratio [18, 20–23, 27]. Therefore, the influence of polydispersity on the glass transition remains largely unexplored in experimental studies. One experimental study

demonstrates that soft poly(N-isopropylacrylamide) particles can be made polydisperse and utilises this to study the bulk rheological behaviour near the glass transition as a function of polydispersity [28]. However, in recent simulations of polydisperse supercooled liquids the importance of single-particle behaviour as a function of particle size was demonstrated as the structural relaxation was initiated by the cage-breaking behaviour of small particles [19]. This demonstrates the need for an experimental system where the single-particle behaviour is observable in a polydisperse suspension with resolution of individual particle size.

Here, we demonstrate how fractional stirring allows us to control the polydispersity of colloidal microspheres from 5 to 30%. We use this method to develop two particle systems, one which allows direct visualisation of the translational and rotational dynamics of every particle with moderate overall polydispersity, up to 10%, and a second one which allows the observation of the translational dynamics only, but at much higher polydispersities, up to 19%. Crucially, for both of these systems we can extract the individual size of each particle from a single confocal image. Our system opens the door for uncovering the particle-size resolved dynamics in suspensions of a range of polydispersities, thereby shedding new light on the colloidal glass transition.

6.2 Controlling Polydispersity with Fractional Stirring

Our method to produce colloidal particles of controlled polydispersity is outlined in the schematic in Fig 6.1a). First, 3-(trimethoxyysilyl)propyl methacrylate (TPM) is hydrolysed by stirring in an acidic solution. Next, addition of a base triggers a rapid condensation reaction which produces a suspension of monodisperse droplets [29]. These droplets can be grown to a larger size by dripping more acid hydrolysed TPM (hTPM) into the suspension of droplets. If the suspension is stirred during the growth stage the droplets remain monodisperse. However, if the suspension is left to stand without stirring for the during of the growth, the droplets become polydisperse. After the growth stage the droplets are cross-linked to form solid microspheres. Crucially, by using a method of fractional stirring, where the suspension is left to stand without stirring at the start of the growth and then stirred for the remainder, we are able to systematically tune the polydispersity of the particles as shown in the SEM images in Fig 6.1a).

Fig 6.1bi-iv) shows the size distributions of particles of different polydispersities

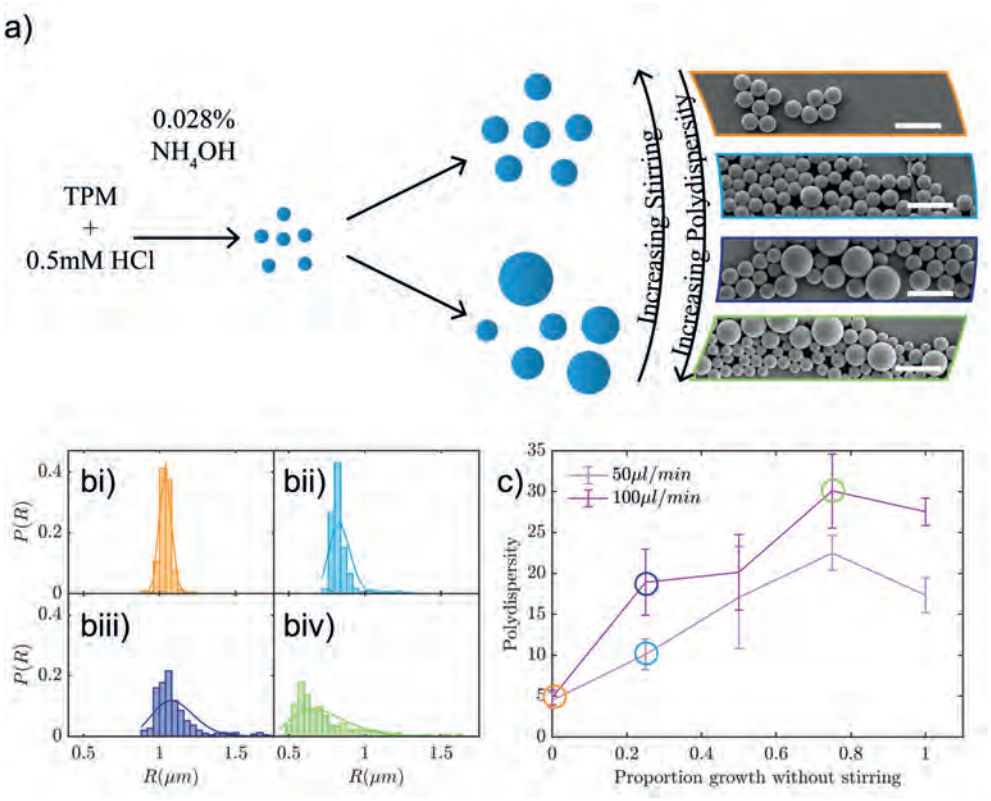

Figure 6.1: a) Schematic showing how intermittent stirring can be used to create TPM microspheres of different polydispersities. Also shown are SEM images of TPM particles prepared using different amounts of intermittent stirring and at different drip rates. Scale bar in each case is $10\mu m$. b) Size distribution of the particles shown in a. The polydispersities are i) 3.6% ,ii) 9% iii) 20% and iv) 31% and each histogram is fitted with an inverse Gaussian distribution. c) Plot of polydispersity against fraction of time stirred during growth for particles grown at two different drip rates.

created using our method of fractional stirring. We define the polydispersity in terms of the particle radius, R, as

$$Polydispersity = \frac{\sigma_R}{\langle R \rangle}, \tag{6.1}$$

where σ_r is the standard deviation of the radius, R, and $\langle R \rangle$ is the mean radius. The size distribution for particles of polydispersity i) 3.6%, ii) 9%, iii) 20% and iv) 31%

are shown, where particles are sized using SEM. We see that as the polydispersity increases the distribution widens and becomes notably skewed towards larger sizes. Each distribution is fitted with an inverse Gaussian to account for the skew to larger sizes at higher polydispersities. Notably our synthesis pathway always produces batches of particles described by a single-modal distribution, the polydispersity increases by widening this distribution.

The continuous increase in polydispersity in this method can be rationalised by considering the impact of stirring during the growth stage. During the period without stirring the particles nearer to the source of the drip experience a higher concentration of hTPM and therefore grow faster to larger sizes. As the particles experience a concentration gradient during this time we see a continuous distribution of sizes described by a single modal distribution. When the suspension is stirred the droplets experience a more homogeneous concentration of hTPM and therefore grow at an equal rate. The ratio of the time spent in these two states can therefore be used to tune the polydispersity while maintaining a single distribution in particle sizes.

A second parameter, the drip rate of hTPM into the suspension during the growth, can also be used to further tune the polydispersity. If the solution is left to stand at a higher drip rate a larger concentration gradient is established and therefore the droplets become more polydisperse. Note that, over the same timeframe, if the suspension is stirred at a higher drip rate the particles simply grow to a larger overall size.

The dependance of the resulting polydispersity on the overall fraction of time without stirring, for two different drip rates, is shown in Fig 6.1d). As the fraction of the growth carried out without stirring increases polydispersity increases, although this increase is lower for the lower drip rate. The mean polydispersity for each point is calculated over three batches of particles and the corresponding error bars show the standard deviation between batches. The error bars are slightly larger for batches carried out without any stirring however the variation never increases beyond 6%. Therefore this method creates polydisperse batches of TPM microspheres in a *controlled* and *repeatable* way.

We have thus established how fractional stirring during droplet growth can be used to create controllably polydisperse particles. TPM particles can be easily refractive index and density matched for use with confocal microscopy [30]. Therefore, we combine

our method of fractional stirring to create two particle systems which allow for the direct observation of the dynamics of polydisperse colloidal particles in 3D using confocal microscopy.

6.3 Translational and Rotational Dynamics as a Function of Particle Size at Moderate Polydispersity

The recently developed 'Off-Centre Under Laser Illumination' (OCULI) particle uniquely allows for the observation of the translational and rotational dynamics of every particle [31]. The OCULI particle consists of a monodisperse TPM microsphere embedded off-centre within a larger TPM microsphere. Attaching a different fluorescent dye to the inner sphere, referred to as the eye, and outer microsphere, referred to as the body, allows imaging of both components. Simultaneous imaging but independent tracking of the body and the eye allows us to track both the translational and rotational dynamics of every particle [31]. By adapting the original synthesis, given in ref [31], to include fractional stirring we can control the polydispersity of OCULI particles. Additionally this particle system allows us to extract the particle size at the single particle level. We use this system to shed light into the translational and rotational dynamics across the colloidal glass transition, resolved as a function of particle size.

6.3.1 Synthesis

A schematic of the synthesis of polydisperse OCULI particles is shown in Fig 6.2a). A small amount of hTPM is added to a suspensions of TPM microspheres. This pre-wetting creates a thin liquid layer of TPM on each particle which favours the growth of this layer as opposed to nucleation of secondary particles during the growth stage, as shown in Fig 6.2a). The thin liquid layer is grown by dripping hTPM into the suspension where again the polydispersity can be tuned by fractional stirring to produce monodisperse or polydisperse particles. As shown in Fig 6.2bi) fractional stirring allows production of OCULI particles of polydispersity 5%, 13% and 16%. To ensure each OCULI particle has a body component that is large enough to be located during particle tracking after a period of fractional stirring all batches undergo a growth stage with stirring. This limits the polydispersities achievable for the OCULI particle system to below 20%.

We can further add a non-fluorescent shell to the particle to facilitate tracking at

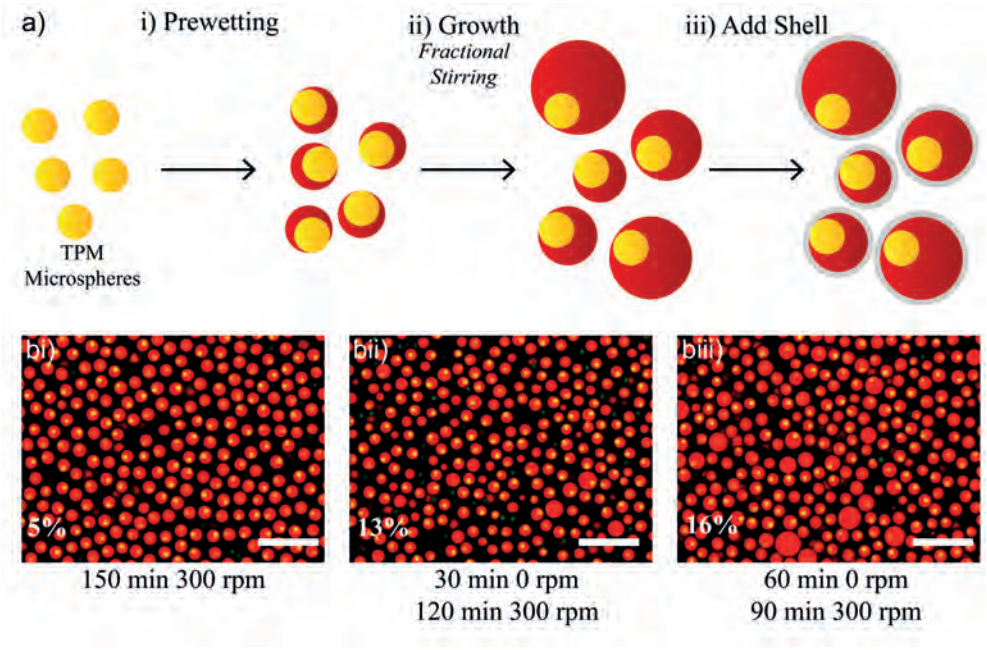

Figure 6.2: a) Schematic of synthesis of polydisperse OCULI particles. b) Confocal images of OCULI particles of different polydispersities created by fractional stirring. Scale bar in all cases is 10μm.

high volume fraction. A non-fluorescent shell was added to the batch of OCULI particles of polydispersity 16% using the procedure described by Liu et al [30]. In short, small TPM lobes were grown around each particle which were cross-linked and left without a fluorescent label. Subsequent addition of hydrolysed TPM restored the particle to a spherical shape by wetting in between the lobes. After cross-linking this created a non-fluorescent shell around each OCULI particle. We note the polydispersity drops to 10% after the addition of the shell. We attributed this to the loss of a small number of very large particles during the process, see Supplementary Information (SI) 6.6.4.

6.3.2 Determination of Particle Size

The ability to resolve particle-size at the single particle level is particularly insightful for a polydisperse population. Typically, for a batch of particles the mean radius and overall polydispersity is measured using SEM. However recent attention has turned to finding methods of extracting in-situ particle size for each individual particle either from their dynamics [31, 32], by image processing [33] or from nearest neighbour distances [34].

Here we demonstrate how our polydisperse OCULI system allows us to determine the size of each individual particle using three different methods.

First, we can extract the particle size from the translational and rotational dynamics at the single-particle level at low ϕ. For a spherical particle the translational diffusion coefficient, D_T, and rotational diffusion coefficient, D_R, are defined as, [35, 36]:

$$D_T = \frac{k_B T}{6\pi\eta R}, \quad \text{and} \quad D_R = \frac{k_B T}{8\pi\eta R^3}, \tag{6.2}$$

where η is the solvent viscosity and R is the particle radius. Therefore, for a particle system where both D_T and D_R can be extracted, R, can be determined as,

$$R_D = \sqrt{\frac{3D_T}{4D_R}}. \tag{6.3}$$

Provided enough statistics can be gathered Eq 6.3 can be used to give an in-situ measure for the size of each individual particle. To demonstrate this we prepare a particle suspension of OCULI particles with a non-fluorescent shell and a polydispersity of 10%, at volume fraction, $\phi = 0.01$. The particles are simultaneously density and refractive index matched in tetralin, trichloroethylene and tetrachloroethylene [29]. This suspension is sealed in a capillary and left to equilibrate overnight. For each particle we calculate both the mean-squared displacement (MSD), $\langle \Delta r^2 \rangle$, and the mean-squared angular displacement (MSAD), $\langle \Delta\theta^2 \rangle$. Rotational displacement was calculated using the method outline in ref [37]. The single particle D_T and D_R are extracted by fitting $\langle \Delta r^2 \rangle = 6D_T\tau$ and $\langle \Delta\theta^2 \rangle = 4D_R\tau$, as shown in Fig 6.3 bi) and bii). Only fits to the MSD and MSAD with an R-squared values ≥ 0.99 are used to extract D_T and D_R. We define the radius extracted from the translational and rotational dynamics using Eq 6.3 as R_D and Fig 6.3 biii) shows the resulting distribution of R_D as well as the size distribution measured from SEM, R_{SEM}. The ensemble averaged mean of R_D is notably larger than the mean of R_{SEM} due to shrinkage of particles in the vacuum of the SEM. Additionally, the match in the shape of the distribution is also quite poor as the distribution of R_D is notably wider than the distribution of R_{SEM}. This can be attributed to the difficulty in fitting single-particle MSDs and MSAD which are notably noisier than an ensemble averaged quantity. There are several limitations to

determining the particle size using this method. First, only a dilute sample can be used to determine R_D as both translational and rotational dynamics must be diffusive. Furthermore, this method require a trajectory of at least 50 frames to gain a reasonable estimate for R_D.

The second method to extract individual particle size relies on the geometry of the OCULI particle. As demonstrated in Fig 6.3ci-iii) for each particle we track the eye and the body using 3D particle tracking routines. The distance between the two, R_{B2E}, is equal to the radius of the particle, R, if we include two corrections: the radius of the eye, R_E, and the thickness of the non-fluorescent shell, Δ_S,

$$R = R_{B2E} + R_E + \Delta_S. \tag{6.4}$$

Note that both R_E and Δ_S are measured using SEM. Fig 6.3civ) shows a plot of the corrected R against the distribution of R_{SEM}. The two distributions line up well in both the peak and overall shape. The advantage of this method is only a single confocal image is needed to extract the particle size while a whole trajectory is required for R_D.

The third method to extract particle size of each individual particle in our system can be done using only one component of our particle, the body. To track polydisperse particles we adapt conventional particle tracking routines to account for a large distribution in size, details of this procedure is given in SI 6.6.8. During particle tracking the fluorescence signal from the body is fitted with a Gaussian to refine the location of the particle centre. The width of this Gaussian, R_σ, can also be shown (SI 6.6.9) to correlate with particle size as

$$R = mR_\sigma + C. \tag{6.5}$$

Where both m and C are constants that depend on the imaging conditions as well as the corrections for the non-fluorescent shell. Using Eq 6.5, we find m and C can be defined from:

$$\sigma_R^2 = m^2\sigma_\sigma^2 \qquad \langle R\rangle = m\langle R_\sigma\rangle + C. \tag{6.6}$$

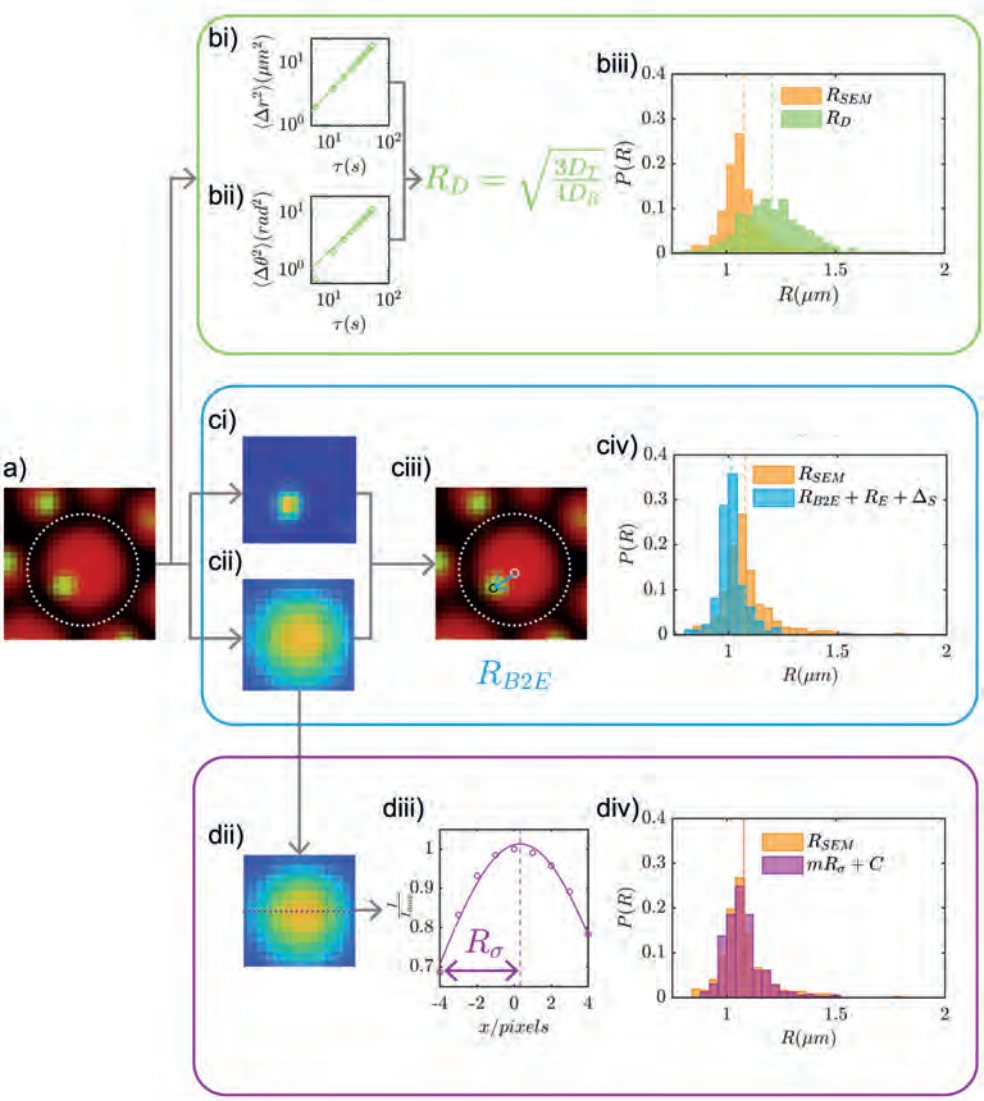

Figure 6.3: a) Confocal image of OCULI particle. bi) Example single particle MSD. bii) Example single particle MSAD. biii) Size distribution of particle diameter extracted from SEM imaging, R_{SEM}, and R_D. ci) Eye channel after bandpass filtering. cii) Body channel after bandpass filtering. ciii) Confocal image showing R_{B2E}. civ) Size distribution of R_{SEM} and R_{B2E}. dii) Body channel after bandpass where dashed line indicates the range over which the intensity profile is fit to extract R_σ. diii) Example fit of intensity profile across particle, solid line is given by Gaussian fit. div) Size distribution of R_{SEM} and R_σ.

A full explanation of how we reach the relations given above is provided in SI 6.6.9). The distribution of the corrected R_σ is shown in Fig 6.3 dii) which again agrees well with the size distribution from SEM imaging.

The particle sizes extracted using R_{B2E} and R_σ better match the distribution from R_{SEM} than the distribution from R_D, therefore these methods are used in this work to obtain individual particle sizes. Notably these methods also allow each particle to be sized from a single frame of a confocal image. Furthermore as R_σ has no dependence on the eye of the OCULI particle this method can be extended into TPM microspheres without an eye to yield individual sizes, as demonstrated in a second particle system. We note that the true radius of the particle cannot be determined from R_{SEM} as the particles shrink due to the vacuum. We estimate this shrinkage, using a method outlined in SI 6.6.10, as 92% of the diameter measured in solution. Therefore, values from R_{B2E} and R_σ are first mapped onto R_{SEM} before being rescaled to account for shrinkage to better estimate the true radius.

6.3.3 Correlation of Translational and Rotational Dynamics with Particle Size in Colloidal Glasses

We have demonstrated a particle system where both the translational and rotational dynamics of every particle can be resolved as a function of size for each individual particle. It has already been established in simulations that particle size plays a key role in the relaxation of translational dynamics in supercooled suspensions [19], however the rotational dynamics have yet to be explored. Observation of rotational dynamics as a function of particle size becomes even more insightful in a jammed system where friction begins to play a key role [38]. To demonstrate this we examine the rotational and translational dynamics as a function of particle size in a sedimentation-diffusion equilibrium of core-shell OCULI particles of polydispersity 10%. The particles are refractive index matched in TTL:TCE 42:58 (w/w) at an initial $\phi = 0.3$. This suspension is sealed in a capillary and allowed to sediment overnight to establish a sedimentation diffusion equilibrium. Fig 6.4a) shows a 3D reconstruction of the resulting sedimentation-diffusion equilibrium while Fig 6.4b) shows the density profile as a function of height. We note the maximum packing fraction reached in our sample, $\phi = 0.66$, is higher than typically reached in a monodisperse system, which is consistent with the fact that polydisperse particles pack more efficiently to achieve higher ϕ, [27, 39, 40]. Confocal images at various heights are shown in Fig 6.4ci-iii)

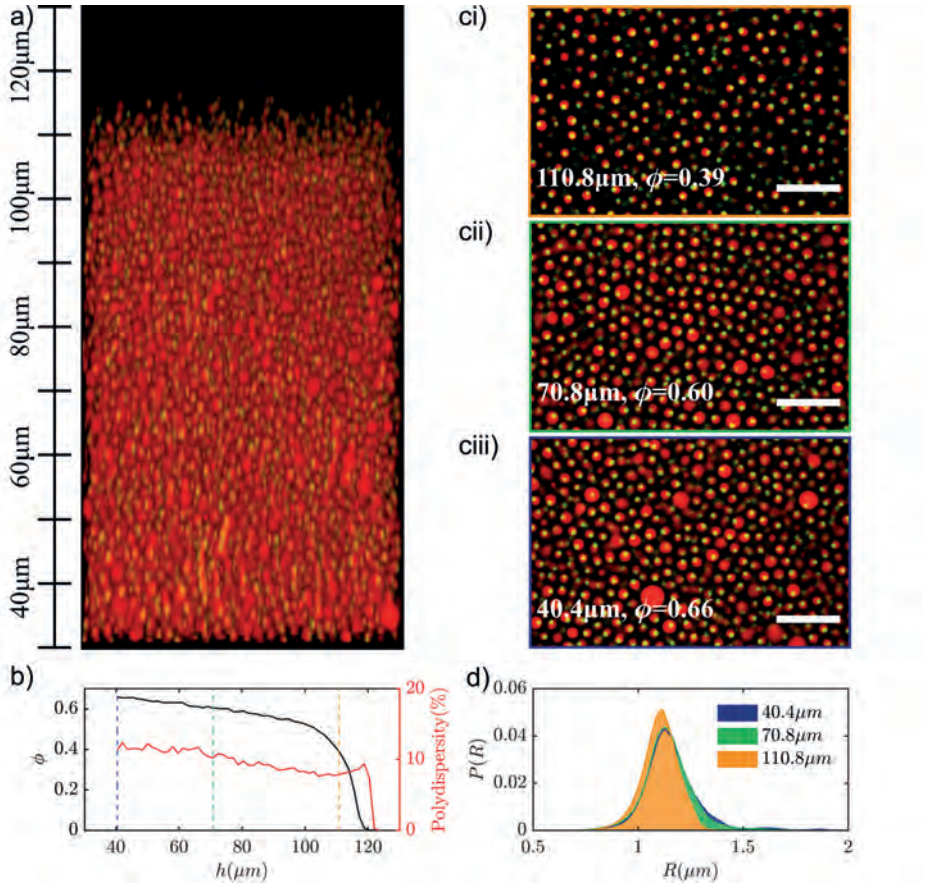

Figure 6.4: a) 3D reconstruction of sedimentation diffusion equilibrium of OCULI particles of 10%. b) ϕ as function of height throughout sediment where ϕ has been calculated from a radical voronoi tessellation. The same profile for polydispersity is also shown. ci)-iii) Confocal images at different heights within sample, scale bar in all cases is $10\mu m$. d) Size distribution recorded at different heights.

where we can observe larger particles being less abundant higher up in the sample due to fractionation. We quantify this in Fig 6.4d) which shows the size distribution at various heights within the sample. As height increases we see the tail of the size distribution towards larger sizes decreases, and the polydispersity also decreases although it remains above 5%.

Next, we characterise the translational and rotational dynamics by the MSD and MSAD as shown in Fig 6.5 a) and b) respectively. In Fig 6.5a), as height decreases,

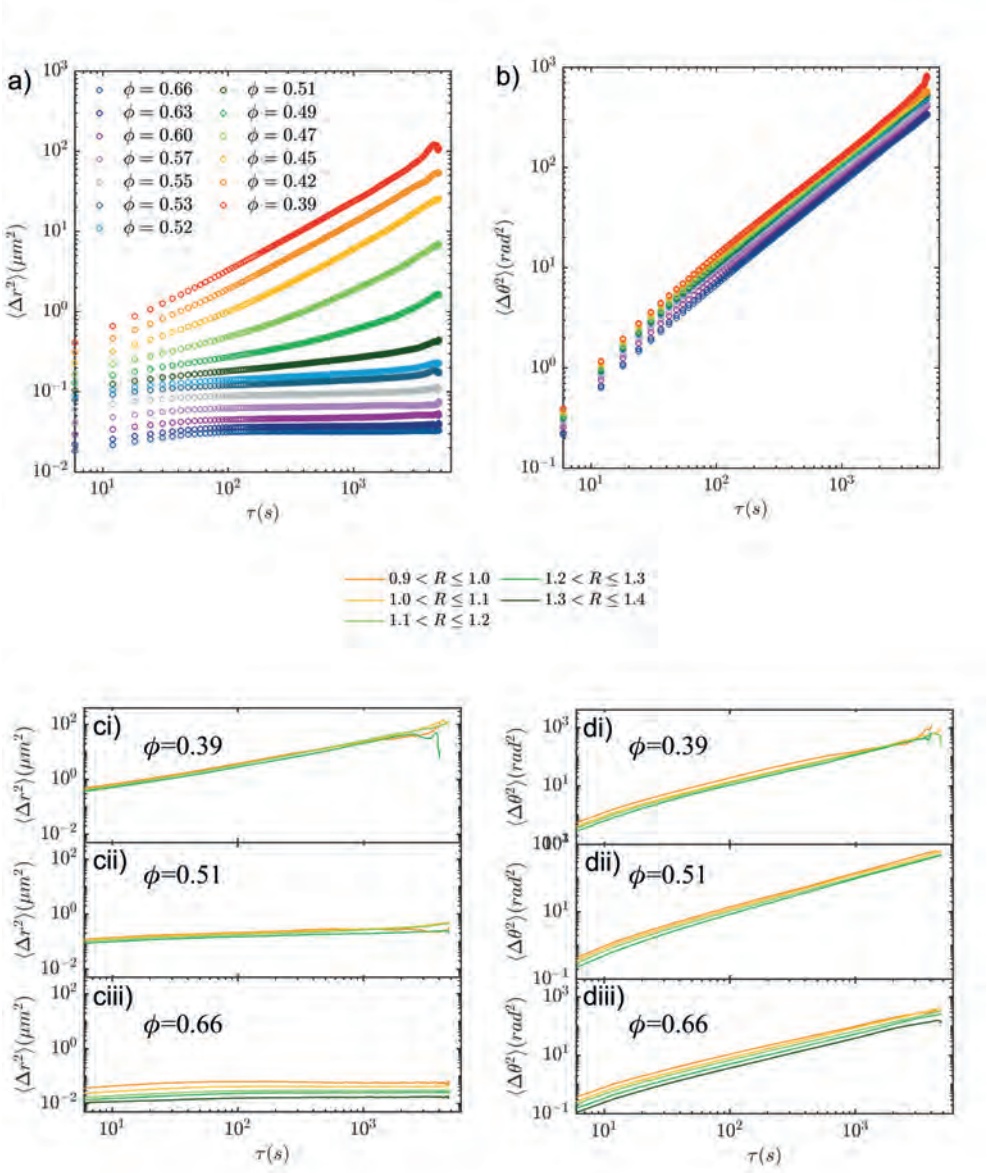

Figure 6.5: a) MSD recorded at different ϕ within the sample. b) MSAD recorded at different heights within the sample. c) MSD resolved at different particle sizes at i) $\phi = 0.39$, ii) $\phi = 0.51$, iii) $\phi = 0.66$. d) MSAD resolved at different particle sizes at i) $\phi = 0.39$, ii) $\phi = 0.51$, iii) $\phi = 0.66$.

and ϕ increases, we can observe the onset of a plateau in the MSD reminiscent of the dynamics becoming quenched at a height of $85.2\mu m$ at $\phi = 0.57$. We take this to be the glass transition within the sediment. Strikingly, the rotational dynamics remain diffusive at all times and for all ϕ with no visible plateau, only a moderate slow down at higher ϕ is observable. Next, and uniquely, we now probe the translational and rotational dynamics across the glass transition as a function of the particle size. For translational dynamics this is shown in Fig 6.5c i-iv). High up in the sample at 110.8 μm, $\phi = 0.39$, the dynamics are diffusive across all different particle sizes, As we descend lower to in the sample we begin to see a separation in the dynamics of different sized particles. We note that due to fractionation the distribution of particles sizes changes with height, as observed in Fig 6.4d). At a height of 102.8 μm, $\phi = 0.51$, the dynamics of the larger particles begin to plateau due to the onset of caging while the smaller particles are much more mobile. Small particles show a notably higher MSD at longer times indicative of a return to diffusive behaviour while larger particles remain more arrested over the whole experimental timeframe. Therefore, the onset of plateau in the MSD at the glass transition occurs at different ϕ for particles of different sizes. This is consistent with computational studies of supercooled polydisperse suspensions [19]. Small particles are less well caged by larger particles and are thus able to cage break at higher ϕ which accounts for the more diffusive MSD at long time. Notably, this size dependence continues into the glass at height 40.4 μm, $\phi = 0.66$, as shown in Fig 6.5 . Though the dynamics of all particles sizes are arrested over the whole experimental timeframe the plateau value of the MSD shows a clear decrease with increasing particle size. Therefore even deep in the glass phase small particles appear to rattle more than large particles.

Fig 6.5di-iii) shows the rotational dynamics at different ϕ resolved for different particle sizes. Similarly to the ensemble averaged dynamics seen in Fig 6.5b) the dynamics at different ϕ for different particle sizes are always diffusive but show separation due to the particle size. This can be explained by considering that D_R is coupled to R^{-3} so a strong dependence on particle size can be expected.

We further examine the degree of coupling of rotational dynamics to particle size by extracting the rotational diffusion coefficient defined in Eq 6.2. The MSAD for $\phi = 0.66$, $\phi = 0.51$, $\phi = 0.39$ for particles of different sizes, shown in Fig 6.5d) are fitted as $\langle \Delta\theta^2 \rangle = 4D_R\tau$ to extract D_R as a function of size at different ϕ. This is shown in Fig 6.6a) which shows how D_R varies as a function of R for selected ϕ. For all ϕ we see

a relatively good fit with AR^{-3} however at higher ϕ we see the pre-factor A decrease due to the increase in viscosity at higher ϕ.

The strong correlation between dynamics and particle size in the glassy region of our sample raises questions on the spatial distribution of the more mobile and less mobile particles in terms of both translational and rotational dynamics. It is well established that upon entering the glass the translational dynamics become heterogeneous with the development of a subpopulation of more mobile particles, which are clustered together [2, 3, 18, 41, 42]. However, experimental studies rarely address the individual particle size distribution in these clusters. One study of binary systems suggests the more mobile subpopulation is dominated by the small species [18], but the size distribution of the most mobile and least mobile particles has not been fully explored for polydisperse suspensions. Therefore we examine the spatial characteristics and particle size distribution of the slowest and fastest particles in the glass for both translational and rotational dynamics.

To examine the characteristics of the particles in the glass we include only particles with an average height below 80 μm, where the ensemble averaged translational dynamics are arrested and $\phi > 0.58$. Furthermore, we define the fast and slow sub-populations as the slowest and fastest 10% in terms of both translational and

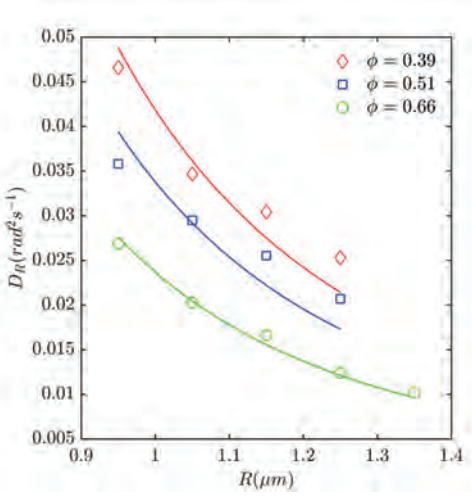

Figure 6.6: a) D_R as a function of R for $\phi = 0.66$, $\phi = 0.51$, $\phi = 0.39$. Trendline of type AR^{-3} is shown for all series.

rotational dynamics. Fig 6.7a) shows a 3D reconstruction of the 10% slowest and 10% fastest particles determined from the translational dynamics. A notable separation of the two sub-populations with height is observable with the fast particles being located at the top of the glass and the slow particles located at the bottom. This can be explained by considering the lower proportion of the sediment experiences a higher gravitational load from the particles above so the particles at the bottom are more confined due to this pressure. Fig 6.7b) shows the same reconstruction from rotational dynamics where a much weaker separation of the two sub-populations in z is observable.

We now examine the size distribution that makes up each sub-population. This is shown in Fig 6.7ci) for translational dynamics and 6.7ii) for rotational dynamics. In both distributions a clear separation is observable with small particles belonging to the fast subpopulation and larger particles belonging to the slow subpopulation. However this separation is more notable for rotational dynamics. This reiterates the trend found in Fig 6.6 where D_R exhibits a strong coupling to R even at high ϕ. For a dilute fluid phase D_R exhibits a stronger coupling to R than D_T, as shown in Eq 6.2, which is shown in Fig 6.7 to extend into the glass.

We next characterise the spatial characteristics of the fast and slow subpopulations by examining the clusters formed in each case. This is shown in Fig 6.7di) for translational dynamics and ii) for rotational dynamics. We see in Fig 6.7di) the translationally slow and fast subpopulations have very similar cluster size distributions. Most of each sub-population exists in small clusters of ≤ 10 but for both fast and slow particles some much larger clusters are formed. In contrast the rotational fast and slow subpopulations both have a much larger probability to exist in smaller clusters, as seen in Fig 6.7dii). Therefore the rotationally fast and slow particles are generally more isolated than the translationally fast and slow particles. This can be rationalised by considering the rotational subpopulations are more evenly distributed throughout the sample in z, leading to a smaller degree of clustering.

We can draw two conclusions about the fast and slow sub-populations for both translational and rotational dynamics in the glass. Firstly, translational dynamics are more governed by the particles' z position within the sample while the rotational dynamics are more strongly coupled to the particle size. Secondly, translationally fast and slow particles display a greater degree of clustering compared to the rotational equivalent.

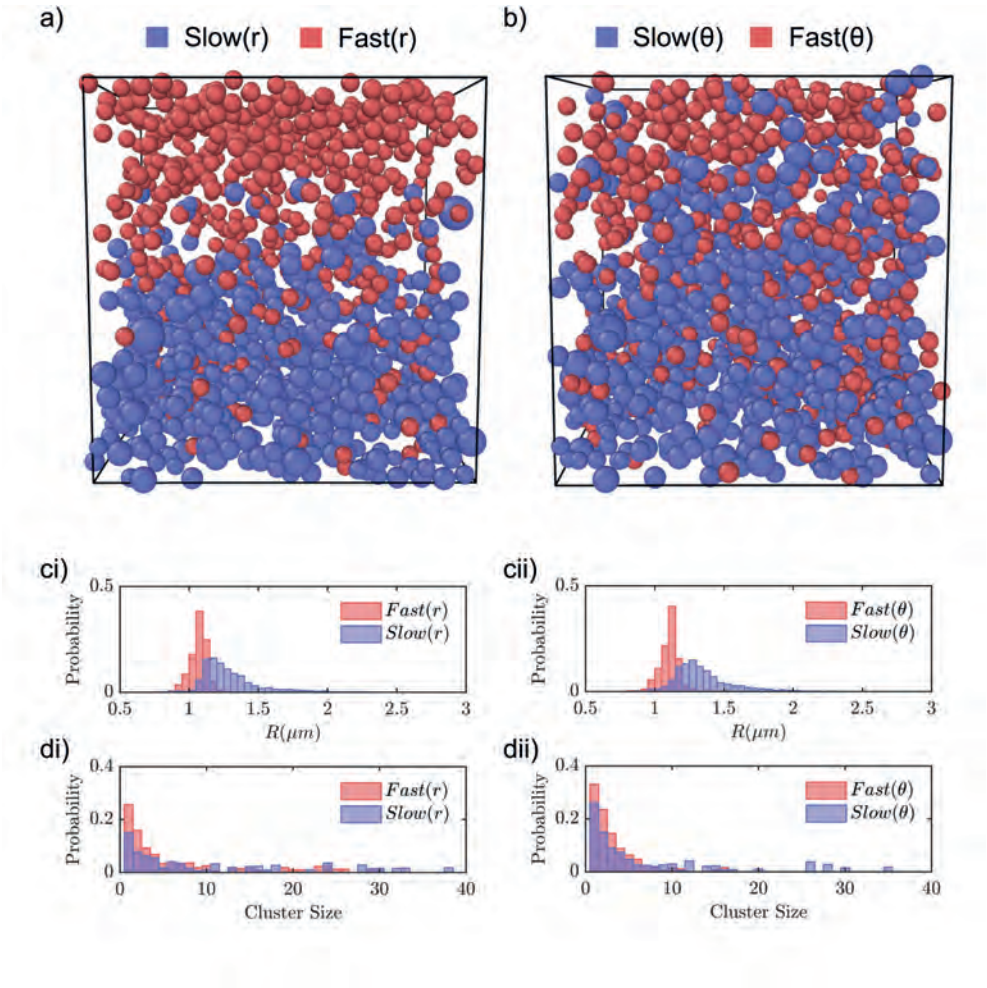

Figure 6.7: a) 3D reconstruction of 10% fastest particles in both rotational and translational dynamics. b) 3D reconstruction of 10% slowest particles in both rotational and translational dynamics. c) Histogram of radius of particle belonging to i) 10% translationally fastest and slowest ii) 10% rotationally fastest and slowest. d) Cluster size distribution of i) 10% translationally fastest and slowest ii) 10% rotationally fastest and slowest.

The limitation of the OCULI particles is the ability to only examine moderate polydispersities. In order to track the body of the OCULI particle the suspension must undergo period of growth with stirring which prevents achieving the higher polydispersities shown in Fig 6.1. However, we have also demonstrated that the particle

size can be extracted from the body of the particle only. Therefore we create a second particle system, without an eye, that allows for the direct observation of the translational dynamics only but at much higher polydispersities.

6.4 Highly Polydisperse TPM Microspheres for Confocal Microscopy

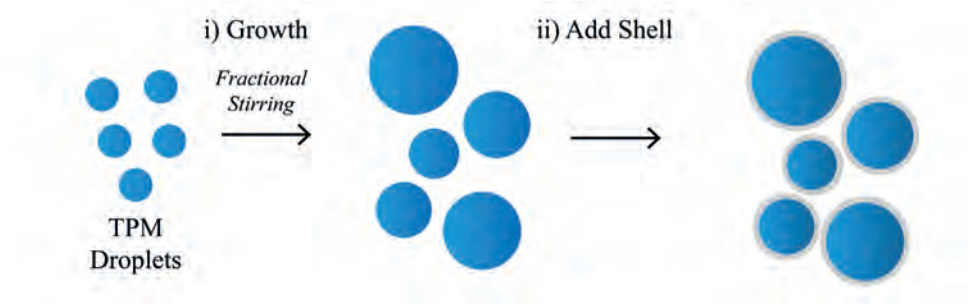

Figure 6.8: Schematic of the synthesis of polydisperse TPM Microspheres with a non-fluorescent shell for confocal microscopy.

The method to create polydisperse TPM microspheres, without an eye, follows the procedure outlined previously in Fig 6.1. Here TPM droplets are first nucleated and grown with fractional stirring to produce different polydispersities. Before cross-linking a fluorescent dye is incorporated into the droplet using a method outlined in ref [29], and in this way fluorescently labelled microspheres were synthesised with polydispersity of 4%, 9%, 20% and 31%. Finally, a non-fluorescent shell was added to enable tracking at high volume fraction [30]. This procedure is shown in the schematic in Fig 6.8. We note that again the polydispersity drops upon the addition of the non-fluorescent shell for all batches to give the final polydispersities 3%, 8%, 14% and 19%. The higher drop in polydispersity for the more polydisperse batches suggests that during the addition of the non-fluorescent shell a small number of large particles are lost. These the large particles in the tail end of the distribution can skew the polydispersity by a large amount; their loss leads to a relatively large decrease in polydispersity despite a small overall change in the distribution, as seen in SI 6.6.4

We have already established that the size of a fluorescent particle can be extracted from a single confocal image by following the procedure to extract R_σ outlined in Section 6.3.2. Using this method we can resolve the size of each individual particle, as well as

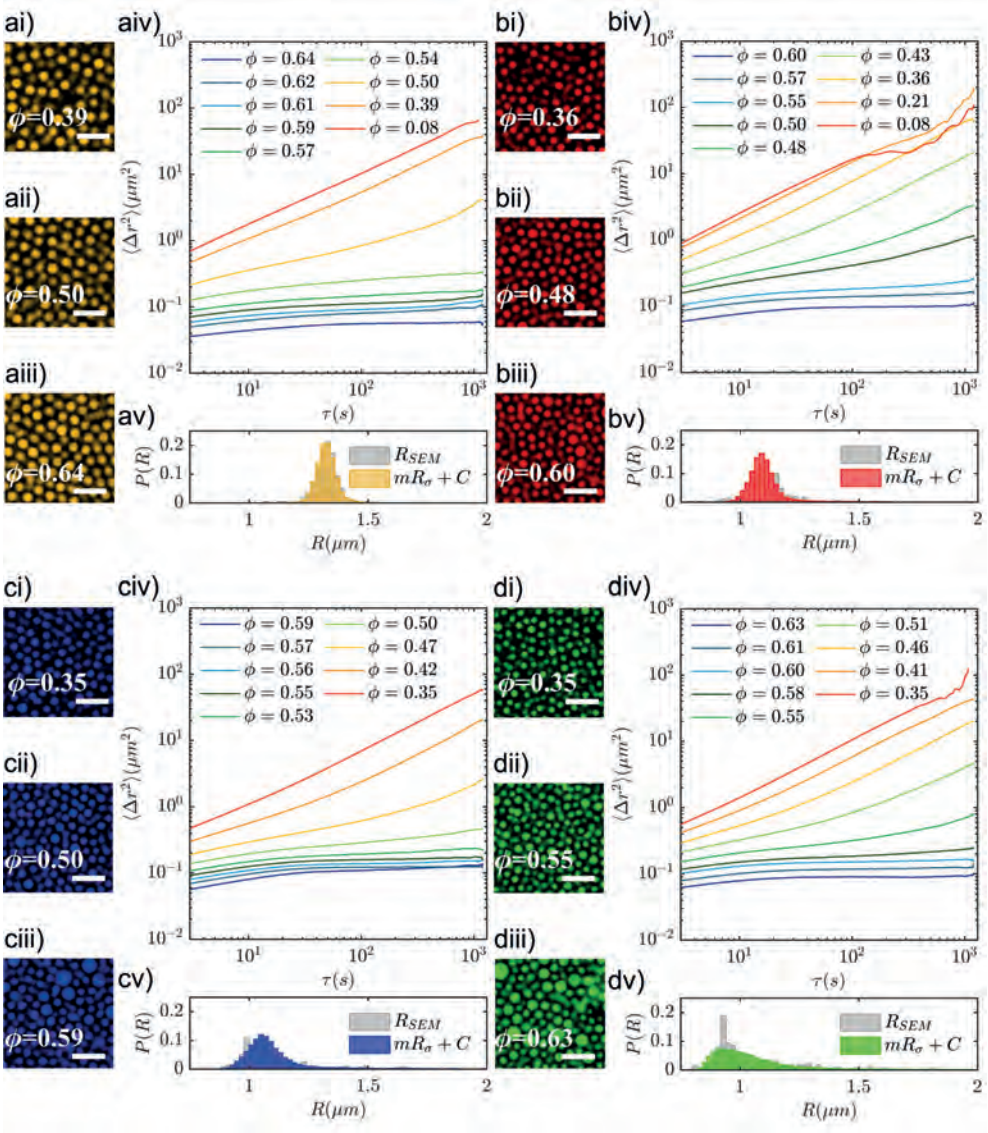

Figure 6.9: For particle suspensions of overall polydispersity a) 3%, b) 8%, c) 14% and d) 19% we show; i) MSD of different ϕ recorded at different heights within the sample, ii) Size distribution calculated from R_σ and the size distribution from R_{SEM}, iii-v) Confocal snapshots at various heights within the sample, scale bar is equal to 10μm.

tracking the translational dynamics, at higher polydispersities than the polydisperse OCULI particle system. Using this particle system we can now re-examine the size correlations in the translational dynamics across the glass transition as a function of polydispersity up to 19%.

All four batches of particles are refractive index matched in TLL and TCE (42:58 w/w). Again a sedimentation-diffusion equilibrium was established by sealing each suspension at initial volume fraction $\phi = 0.3$ in a capillary and leaving overnight to equilibrate. The resulting sedimentation-diffusion equilibriums are examined in Fig 6.9 where for each the MSD at various ϕ, recorded at different heights, are shown in Fig 6.9 a-div). We observe that for all samples, the MSD is diffusive at low ϕ but, as ϕ increases the MSD begins to plateau due to caging. Once this plateau is constant over the experimental timeframe we define the sample as glassy. The extracted R_σ and measured R_{SEM} for each batch are shown, with good agreement between the two distributions for all samples. Also shown are confocal snapshots at similar ϕ but different overall polydispersity where, again a degree of fractionation is observable for the more polydisperse batches.

We next re-examine the dynamics at the glass transition as a function of the particle size. This is shown in Fig 6.10 where the MSD, resolved for different particle sizes, are shown for similar ϕ at different overall polydispersity. Notably, due to fractionation the range of particle sizes decreases as ϕ decreases. For the monodisperse sample we see that particles of all sizes have similar behaviour at all ϕ shown. For the three polydisperse samples at low ϕ, the dynamics of all particles are diffusive, regardless of particle size. However, for a polydispersity of 8% at $\phi = 0.50$ the larger particles are more localised while the smaller particles are still able to undergo cage-breaking. For the sample of polydispersity 8% at $\phi = 0.50$ the particles of between 1.3μm and 1.4μm are more mobile than in the sample of polydispersity 14% at $\phi = 0.50$. Clearly particles experience caging differently depending on the size profile and polydispersity of neighbouring particles. Notably, at the highest ϕ shown for each sample see a clear increase in the spread of the dynamics with size. At an overall polydispersity of 19% at $\phi = 0.63$ small particles have a much higher MSD than large particles. Comparing the data from the highest ϕ achieved in each sample we see the spread of the MSDs increase with increasing polydispersity. Therefore as glass increases in polydispersity the small particles are more prone to rattle.

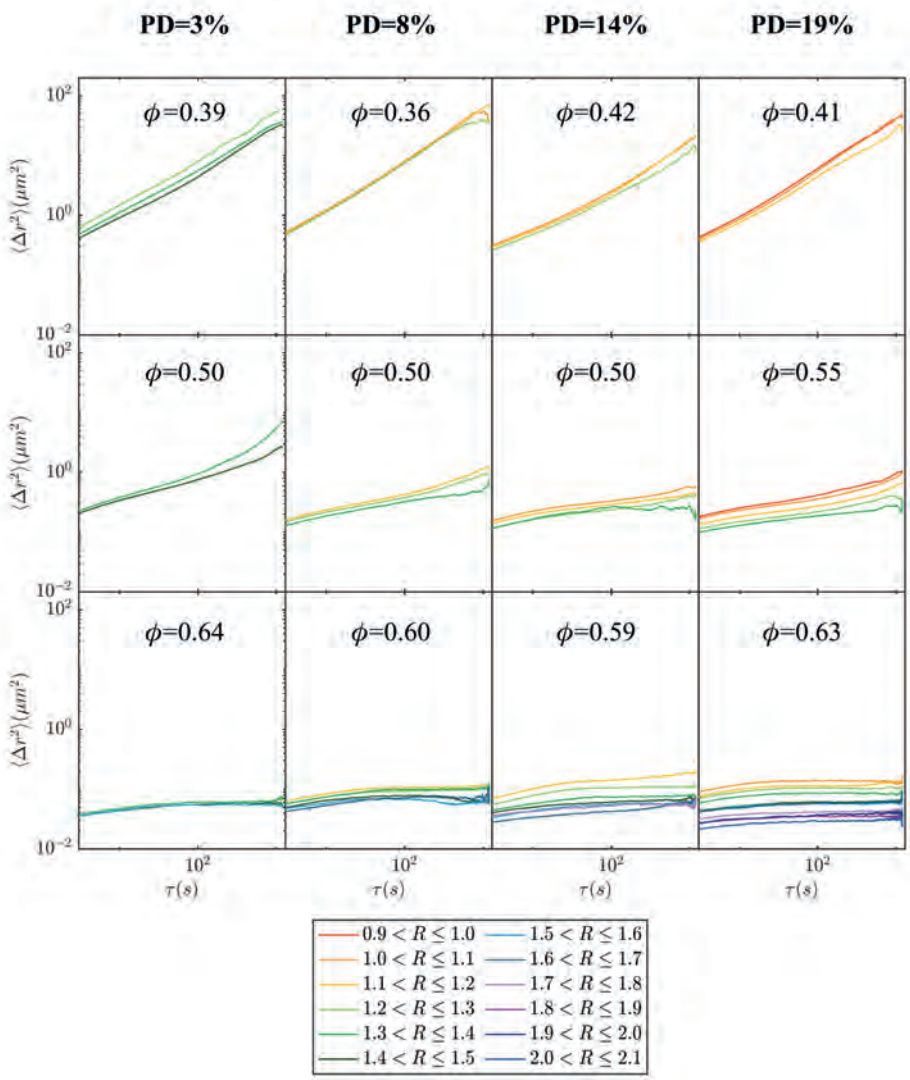

Figure 6.10: MSD resolved as a function of particle size for similar ϕ recorded from suspensions of different overall polydispersity.

We probe this further by defining the glass region of each system as the point where the dynamics are arrested over the course of the experiment in order to examine how the clustering of the translational fast and slow particles changes with polydispersity. Again, we define the translational fast and slow subpopulations as the slowest and fastest 10%. For each sample a 3D reconstruction of the fast and slow particles are shown in Fig

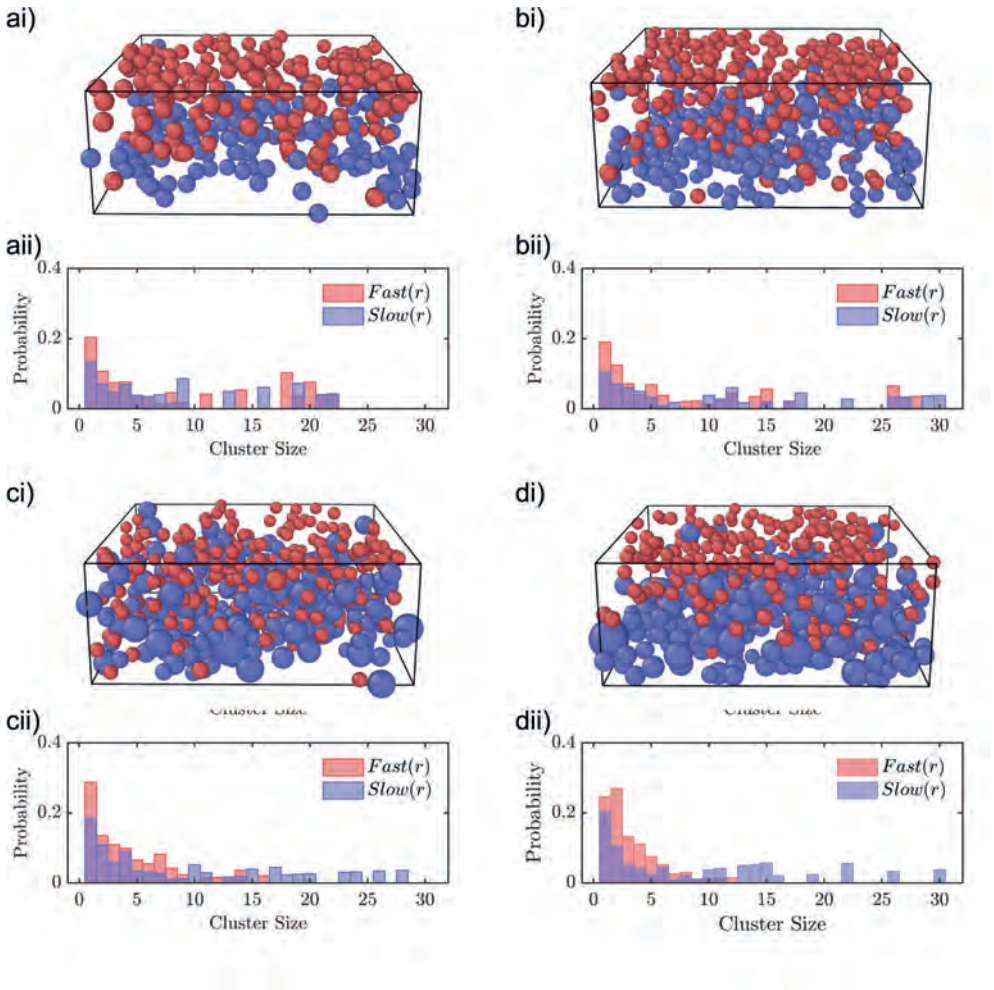

Figure 6.11: i) 3D reconstruction of 10% translationally fast and 10% translationally slow particles and ii) histogram of cluster sizes formed by the same subpopulations for a) ϕ=0.64 polydispersity=3%, b) ϕ=0.60 polydispersity=8%, c) ϕ=0.59 polydispersity=14%, c) ϕ=0.63 polydispersity=19%.

6.11a-di), where the in-situ particle size has been resolved from R_σ. As polydispersity increases we see a the fast subpopulation again become dominated by small particles and the slow subpopulation become increasing made up of larger particles. However the main differences are more apparent if we examine the cluster size distribution for each sample, shown in Fig 6.11 a-dii). As polydispersity increases we see the probability for a particle to be in a cluster of size 1, isolated from the rest of the subpopulation,

increases for both fast and slow particles. Therefore we see that particles of similar sizes in a polydisperse packing are generally not situated beside each other. The smallest and largest particles, which make up the fast and slow subpopulations respectively, are generally more isolated from each other in a more polydisperse packing. In a monodisperse system we can observe clusters of fast particles of sizes up to 20 particles, this has been previously observed as string-like motion in glassy samples. However in a highly polydisperse system the fast particles are more isolated and cluster sizes are much smaller, more akin to single-particles or small groups rattling within cages. This transition from string-like to rattling clusters of mobile particles has not been observed as it is only with our system that polydispersity can be smoothly altered to reveal this transition.

6.5 Conclusion

In conclusion we have shown how fractional stirring can be used to control the polydispersity of TPM microspheres. We used this method to develop two particle systems. Firstly, a particle system which allows examination of the rotational and translational dynamics of every particle within a system as a function of individual particle size at moderate polydispersities. We used this system to demonstrate that translational and rotational dynamics are both coupled to particle size, both at the glass transition and in the glass phase. Furthermore we demonstrate the translational dynamics are more coupled to particle height within the sample while rotational dynamics are more coupled to particle size. We then demonstrated a second particle system which allows the observation of the translational dynamics only, albeit at much higher polydispersities. We show that dynamics at the glass transition depend on the overall aspect ratio in the sample. Furthermore, by identifying the subpopulation of the translationally most and least mobile an interesting crossover in spatial characteristics of the mobile subpopulation is observed with increasing polydispersity. We have demonstrated not only that polydispersity can be used to alter the phase behaviour of colloidal microspheres but having control over it key as the overall polydispersity controls the dynamics of the system.

6.6 Supplementary Information

6.6.1 Materials

3-(trimethoxysilyl)propyl methacrylate (TPM, ≥97%, Sigma Aldrich), ammonium hydroxide solution (28% vol. NH_3 in H_2O, Alfa Aesar), azobisisobutyronitrile (AIBN, BDH, UK), Cyanine3 NHS Ester (Lumiprobe), Chloroform ($CHCl_3$, Fischer Scientific), Pluronic® F-108 (F-108, Sigma Aldrich), 3-aminopropyl trimethoxysilane (APS, Sigma Aldrich), acetone (Sigma Aldrich), trichloroethylene (TCE, ≥99.5%, Sigma Aldrich), 1,2,3,4-tetrahydronaphthalene (TTL, anhydrous, 99%, Sigma Aldrich) and tetrachloroethylene (PERC, 99%, Alfa Aesar) were used as received. A polyisobutylene succinic anhydride stabilizer, OLOA 11000, was provided by Eric Dufresne and Azelis. Double-distilled water was sourced from an PURELABS Chorus 1 ultrapure water unit.

6.6.2 Synthesis of Polydisperse Microspheres

To synthesise polydisperse TPM microspheres the procedure is adapted from ref [29]. First TPM is hydrolysed by diluting 2ml TPM in 20ml 0.05mM HCl and stirring for 1 hour. 2ml of the product is diluted again with 10.5ml HCl and stirred for 10 minutes before 12.5ml 0.028% NH4OH is added. The suspension is left to stand for 1 hour during which monodisperse droplets nucleate. TPM, that has been hydrolysed under the same conditions described previously, is then dripped into the suspension at a rate of $50\mu l/min$ or $100\mu l/min$ for 60 min. To tune the polydispersity the suspension is either left to stand without stirring or stirred at 300rpm. The particles are then cross-linked by adding a spatulalful of AIBN to the suspension and heating to $80°C$ for 3 hours. If the particle are to be used for confocal microscopy then are labelled with Cyanine3-NHS Ester before crosslinking using the method described in ref [29].

6.6.3 Synthesis of Polydisperse OCULI Particles

To create polydisperse OCULI particles the procedure is adapted from ref [31]. TPM microsphere of diameter 640nm, labelled with BDP-NHS Ester, are prewet hydrolysed TPM by adding 5ml 0.028% NH4OH, 2ml TPM microspheres (10% v/v) and 2ml hydrolysed TPM to a glass vial and tumbling for 30 minutes. The solution is then diluted in 0.028% NH4OH before a hydrolysed TPM is dripped into the flask using the same method described previously to tune the polydispersity. The droplets are labelled with Cyanine3-NHS Ester before crosslinking using the method described in ref [29].

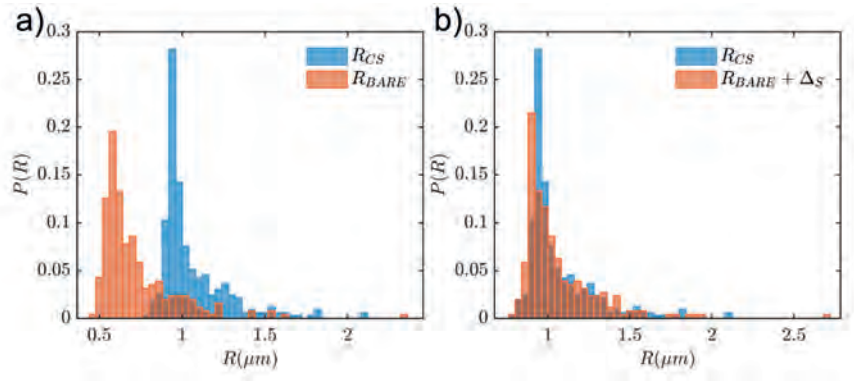

Figure 6.12: a) Particle size distributions of particles without, R_{BARE}, and with, R_{CS}, non-fluorescent shell. b) Particle size distributions of particles without, R_{BARE}, shifted by the shell thickness Δ_S, and with, R_{CS}, non-fluorescent shell.

6.6.4 Effect of Non-Fluorescent Shell

The addition of a non-fluorescent shell allows particles to be more accurately tracking at high ϕ but is accompanied by a relatively large drop in polydispersity. Shown in Fig 6.12a) is the particle size distribution, measured from SEM for a batch for particles before, R_{BARE}, and after the addition of a non-fluorescent shell, R_{CS}. Notably the two distributions share a similar shape centred around different means. This is further demonstrated in Fig 6.12b) where the distribution for R_{BARE} is shifted by Δ_S which we determine as the difference between the mean values of R_{BARE} and R_{CS}. The two distributions line up well in terms of shape, however, the polydispersity drops from 31% to 19%. We have previously characterised the shape of the distribution as an inverse Gaussian with a notable tail towards larger sizes. This drop in polydispersity is caused by the loss of a few large particles, during the synthesis, which drastically decreases σ, leading to a large drop in polydispersity despite the shape of the overall distribution remaining the same.

6.6.5 SEM Microscopy

All particles were sized using a Quanta3D FEG Scanning Electron Microscope. Prior to imaging the particles were coated with 10nm of gold using a Quorem Q150TS Plus coater. At least 100 particles were sized from each batch to measure the polydispersity.

6.6.6 Confocal Microscopy

The imaging set up used in this work comprised of a two-channel 3D confocal laser scanning microscope; Olympus IX73 inverted microscope, 60× Olympus Plan Apochromat oil immersion objective (NA = 1.42). High speed imaging was achieved by Thorlabs confocal 12kHz resonant scanner and an objective-mounted piezoelectric Z-stage (Physik Instrumente). Simultaneous illumination of the sample with laser of wavelength 488nm and 532nm allows near simultaneous imaging of both components of the OCULI particle. For the data analysed in Fig 6.3 a volume of 51.2×51.2×51.2 was recorded in 3 seconds (800 frames). The sample was imaged three times at two different heights to image a range of particle sizes. For the data analysed in Fig 6.4, 6.5 and 6.6 three volumes of 51.2×51.2×100.2 μm^3 was recorded in 6 seconds (800 frames). For the data analysed in Fig 6.9, 6.10 and 6.11 a volume of 51.2×51.2×51.2 μm^3 was recorded in 3 seconds (400 frames).

6.6.7 Cluster Analysis

When a cluster analysis is used in this work the nearest neighbour distance is set as the first minimum in the $g(r)$. To prevent counting particles twice only particles tracked for >100 frames are included in the analysis.

6.6.8 Tracking of Polydisperse Particles

Our method of tracking polydisperse particles follows the procedure established by Crocker and Grier [43]. The local maxima within a 3D image are first located then the intensity around each maxima is fitted with a Gaussian in the x, y and z dimensions to locate the centre to sub pixel accuracy. The range over which this fit is carried out is typically set as uniform for all particles and the width of each Gaussian is used as a measure of the size of each feature, allowing noise to be eliminated after tracking. To track polydisperse particles with a large variety of sizes setting the range for the Gaussian fit posses a problem as too large a region for small particles leads to fitting over multiple particles while too small for large particles leads to pixel biasing. Therefore we employ an adaptive mask: a small initial mask size is set of 2 pixels in +ve and -ve direction, this mask size is increased in each direction until the intensity at the maximum extent of the range has decreased by 80% of it's original value. This threshold is set to prevent fitting over multiple particles. The intensity is then fitted over this expanded range to find the particle centre. An average of the width in the x and y direction is

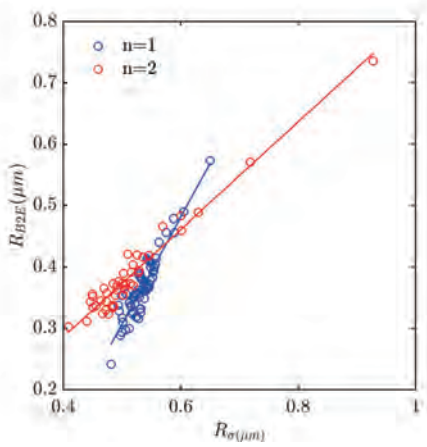

Figure 6.13: R_{B2E} against R_σ for the same data set tracked after bandpass filtering with gaussian blur of width 1 and 2.

recorded due to poor resolution in z-direction.

6.6.9 Extraction of Particle Size from Tracking Algorithms

After tracking each OCULI particle we have access to both the width of the intensity profile from the fit described above, R_σ, and the body to eye distance, R_{B2E}. Shown in Fig 6.13 is a plot of R_σ against R_{B2E} for a suspension of OCULI particles of polydispersity 10% after processing through two different bandpass filters of with a gaussian blur of width 1 and 2. As the width of the gaussian blur changes the linear relation between R_{B2E} and R_σ changes but values for the offset and gradient change.

As shown in Fig 6.13, we use a linear mapping between R_{B2E} and R_σ, as,

$$R_{B2E} = mR_\sigma + c \tag{6.7}$$

As we have previously established R_{B2E}, in Eq 6.4, can be mapped onto the true particle radius given the equation,

$$R = R_{B2E} + R_E + \Delta_S. \tag{6.8}$$

Substituting in for R_{B2E} using Eq 6.7 we come to the expression,

$$R = mR_\sigma + c + R_E + \Delta_S. \tag{6.9}$$

For the same batch of particle, R_E and Δ_S are constants we rewrite as,

$$R = mR_\sigma + C \qquad \text{where} \qquad C = c + R_E + \Delta_S. \tag{6.10}$$

As we have mapped R directly onto R_σ we develop the following method to determine m and C from the two distributions only, without first requiring R_{B2E}. From Eq 6.10 we can formulate the following relation for the mean values of R and R_σ,

$$\langle R \rangle = \langle mR_\sigma + C \rangle \tag{6.11}$$

$$\langle R \rangle = m\langle R_\sigma \rangle + C. \tag{6.12}$$

Furthermore we can relate the two variances by,

$$\begin{aligned}
\sigma_R^2 &= \langle (R - \langle R \rangle)^2 \rangle \\
&= \langle (mR_\sigma + C - \langle R \rangle)^2 \rangle \\
&= m^2 \left\langle \left(R_\sigma - \frac{\langle R \rangle - C}{m} \right)^2 \right\rangle \\
&= m^2 \left\langle \left(R_\sigma - \langle R_\sigma \rangle \right)^2 \right\rangle \\
&= m^2 \sigma_{R_\sigma}^2
\end{aligned} \tag{6.13}$$

Therefore the constant m can be found from the ratio of the variances and the constant C from Eq. 6.12.

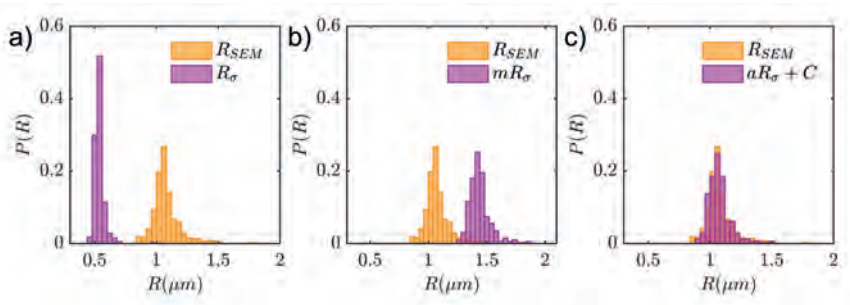

Figure 6.14: a) Size distribution of R_{SEM} and R_σ. b) Size distribution of R_{SEM} and mR_σ. c) Size distribution of R_{SEM} and $mR_\sigma + C$.

6.6.10 Accounting for Shrinking due to Vacuum in SEM

We estimate the shrinking due to the presence of the vacuum during SEM imaging by examining the ensemble averaged dynamics of a suspension of OCULI particles density matched in TCE:TLL:PERC and extracting the radius using the method established for R_D. When compared to the mean radius determined from SEM this gives a shrinkage of 92%. This value is used to determine more accurate volume fractions.

6.6.11 Definition of Fast and Slow Subpopulation

To find the slow and fast sub-populations we calculate the MSD and MSAD at $\tau = 5.9$ for each particle. The slow subpopulation is defined as the slowest 10% using this metric and the fast subpopulation as the fastest 10%.

6.6.12 Rotational Displacement

Rotational displacement was calculated in line with previous studies [37]. First we define the rotational trajectory between each frame as

$$\psi(t_2) = \hat{\omega} \cdot \alpha, \tag{6.14}$$

where $\hat{\omega}$ is the axis of rotation between frames, ($\hat{\omega} = \hat{u}(t_1) \times \hat{u}(t_2)$), and α is the angle of rotation, ($\alpha = \cos^{-1}(\hat{u}(t_1) \cdot \hat{u}(t_2))$). The sum of these displacement between each frame is evaluated as the integral,

$$\theta(\tau) = \int_1^{t_2} \psi(t)dt. \tag{6.15}$$

The resulting the rotational trajectory, θ, can be used as a direct analogue to the translational trajectory.

We note it is more difficult to link the eye to the body for polydisperse particles due to the range of particle sizes. To not have this difficulty affect our rotational particle trajectories, we only include trajectories where the eye and body coordinates are found for 90% of the total trajectory. This corresponds to including nearly 90% of the total number of particles in our analysis.

6.6.13 Acknowledgements

All particle synthesis, confocal imaging and analysis was carried out by R. A. Crothers while SEM imaging was carried out by E. Simons and R. A. Crothers. We thank M. Reijneveld for useful discussions.

6.7 Bibliography

[1] W. C. K. Poon. Colloids as big atoms. *Science*, 304(5672):830–831, 2004.

[2] W. K. Kegel and A. van Blaaderen. Direct observation of dynamical heterogeneities in colloidal hard-sphere suspensions. *Science*, 287(5451):290–293, 2000.

[3] E. R. Weeks, J. C. Crocker, A. C. Levitt, A. Schofield, and D. A. Weitz. Three-dimensional direct imaging of structural relaxation near the colloidal glass transition. *Science*, 287(5453):627–631, 2000.

[4] U. Gasser, E. R Weeks, A. Schofield, P. N. Pusey, and D. A. Weitz. Real-space imaging of nucleation and growth in colloidal crystallization. *Science*, 292(5515):258–262, 2001.

[5] H. Yoshida, J. Yamanaka, T.i Koga, T. Koga, N. Ise, and T. Hashimoto. Transitions between ordered and disordered phases and their coexistence in dilute ionic colloidal dispersions. *Langmuir*, 15(8):2684–2702, 1999.

[6] M. S. Elliot, S. B. Haddon, and W. C. K. Poon. Direct observation of pre-critical nuclei in a metastable hard-sphere fluid. *J. Phys: Condens. Matter*, 13(23):L553, 2001.

[7] A. Kuijk, A. van Blaaderen, and A. Imhof. Synthesis of monodisperse, rodlike silica colloids with tunable aspect ratio. *J. Am. Chem. Soc.*, 133(8):2346–2349, 2011.

[8] T. Hueckel, G. M. Hocky, and S. Sacanna. Total synthesis of colloidal matter. *Nat. Rev. Mater.*, 6(11):1053–1069, 2021.

[9] M. Kamp, S. Sacanna, and R. P. A. Dullens. Spearheading a new era in complex colloid synthesis with tpm and other silanes. *Nat. Rev. Chem.*, 8(6):433–453, 2024.

[10] E. Bianchi and C. N. Blaak, R.and Likos. Patchy colloids: state of the art and perspectives. *Phys. Chem. Chem. Phys.*, 13(14):6397–6410, 2011.

[11] P. J. Collings. *Liquid crystals: nature's delicate phase of matter*. Princeton University Press, 2002.

[12] D. Andrienko. Introduction to liquid crystals. *J. Mol. Liq.*, 267:520–541, 2018.

[13] C. Fernández-Rico, T. Yanagishima, A. Curran, D. G. A. L. Aarts, and R. P. A. Dullens. Synthesis of colloidal su-8 polymer rods using sonication. *Adv. Mater.*, 31(17):1807514, 2019.

[14] A. Kuijk, D. V. Byelov, A. V. Petukhov, A. van Blaaderen, and A. Imhof. Phase behavior of colloidal silica rods. *Faraday Discuss.*, 159(1):181–199, 2012.

[15] C. Fernández-Rico, M. Chiappini, T. Yanagishima, H. de Sousa, D. G. A. L. Aarts, M. Dijkstra, and R. P. A. Dullens. Shaping colloidal bananas to reveal biaxial, splay-bend nematic, and smectic phases. *Science*, 369(6506):950–955, 2020.

[16] R. Kotni, A. Grau-Carbonell, M. Chiappini, M. Dijkstra, and A. van Blaaderen. Splay-bend nematic phases of bent colloidal silica rods induced by polydispersity. *Nat. Commun.*, 13(1):7264, 2022.

[17] P. I. C. Teixeira and J. M. Tavares. Phase behaviour of pure and mixed patchy colloids — theory and simulation. *Curr. Opin. Colloid Interface Sci.*, 30:16–24, 2017.

[18] T. Narumi, S. V. Franklin, K. W. Desmond, M. Tokuyama, and E. R. Weeks. Spatial and temporal dynamical heterogeneities approaching the binary colloidal glass transition. *Soft Matter*, 7(4):1472–1482, 2011.

[19] I. Pihlajamaa, C. C. L. Laudicina, and L. M. C. Janssen. Influence of polydispersity on the relaxation mechanisms of glassy liquids. *Phys. Rev. Res.*, 5(3):033120, 2023.

[20] P. Bartlett, R. H. Ottewill, and P. N. Pusey. Freezing of binary mixtures of colloidal hard spheres. *J. of Chem. Phys.*, 93(2):1299–1312, 1990.

[21] J. M. Lynch, G. C. Cianci, and E. R. Weeks. Dynamics and structure of an aging binary colloidal glass. *Phys. Rev. E*, 78:031410, 2008.

[22] T. Sentjabrskaja, E. Babaliari, J. Hendricks, M. Laurati, G. Petekidis, and S. U. Egelhaaf. Yielding of binary colloidal glasses. *Soft Matter*, 9(17):4524–4533, 2013.

[23] S. R. Williams and W. van Megen. Motions in binary mixtures of hard colloidal spheres: Melting of the glass. *Phys. Rev. E*, 64(4):041502, 2001.

[24] P. G. Bolhuis and D. A. Kofke. Monte carlo study of freezing of polydisperse hard spheres. *Phys. Rev. E*, 54:634–643, 1996.

[25] E. Masoero, E. Del Gado, R. J.-M. Pellenq, F.-J. Ulm, and S. Yip. Nanostructure and nanomechanics of cement: Polydisperse colloidal packing. *Phys. Rev. Lett.*, 109:155503, 2012.

[26] A. J. Ebrahimi, D.and Whittle and R. J.-M. Pellenq. Effect of polydispersity of clay platelets on the aggregation and mechanical properties of clay at the mesoscale. *Clays Clay Miner.*, 64(4):425–437, 2016.

[27] D. Heckendorf, K. J. Mutch, S. U. Egelhaaf, and M. Laurati. Size-dependent localization in polydisperse colloidal glasses. *Phys. Rev. Lett.*, 119(4):048003, 2017.

[28] S. K. Behera, D. Saha, P. Gadige, and R. Bandyopadhyay. Effects of polydispersity on the glass transition dynamics of aqueous suspensions of soft spherical colloidal particles. *Phys. Rev. Mater.*, 1(5):055603, 2017.

[29] R. A. Crothers, N. H. P. Orr, B. van der Meer, R. P. A. Dullens, and T. Yanagishima. Characterization and optimization of fluorescent organosilica colloids for 3d confocal microscopy prepared under "zero-flow" conditions. *Langmuir*, 39(15):5306–5314, 2023.

[30] Y. Liu, T. Yanagishima, Arran Curran, K. V Edmond, S. Sacanna, and R. P. A. Dullens. Colloidal organosilica spheres for three-dimensional confocal microscopy. *Langmuir*, 35(24):7962–7969, 2019.

[31] T. Yanagishima, Y. Liu, H. Tanaka, and R. P. A. Dullens. Particle-level visualization of hydrodynamic and frictional couplings in dense suspensions of spherical colloids. *Phys. Rev. X*, 11(2):021056, 2021.

[32] S. Schütter, J. Roller, A. Kick, J-M. Meijer, and A. Zumbusch. Real-space imaging of translational and rotational dynamics of hard spheres from the fluid to the crystal. *Soft Matter*, 13(44):8240–8249, 2017.

[33] M. Leocmach and H. Tanaka. A novel particle tracking method with individual particle size measurement and its application to ordering in glassy hard sphere colloids. *Soft Matter*, 9(5):1447–1457, 2013.

[34] R. Kurita, D. B. Ruffner, and E. R. Weeks. Measuring the size of individual particles from three-dimensional imaging experiments. *Nat. Comm.*, 3(1):1127, 2012.

[35] A. Einstein. *Investigations on the Theory of the Brownian Movement*. Courier Corporation, 1956.

[36] P. J. W. Debye. *Polar Molecules*. Dover Publications, 1929.

[37] G. L. Hunter, K. V. Edmond, M. T. Elsesser, and E. R. Weeks. Tracking rotational diffusion of colloidal clusters. *Opt. Express*, 19(18):17189–17202, 2011.

[38] C-P. Hsu, S. N. Ramakrishna, M. Zanini, N. D. Spencer, and L. Isa. Roughness-dependent tribology effects on discontinuous shear thickening. *Proc. Natl. Acad. Sci. U.S.A.*, 115(20):5117–5122, 2018.

[39] W. Schaertl and H. Sillescu. Brownian dynamics of polydisperse colloidal hard spheres: Equilibrium structures and random close packings. *J. Stat. Phys.*, 77:1007–1025, 1994.

[40] Kenneth W.. Desmond and E. R. Weeks. Influence of particle size distribution on random close packing of spheres. *Phys. Rev. E*, 90:022204, 2014.

[41] R. E. Courtland and E. R. Weeks. Direct visualization of ageing in colloidal glasses. *J. Phys. Condens. Matter*, 15(1):S359, 2002.

[42] E. R Weeks, J. C. Crocker, and D. A. Weitz. Short-and long-range correlated motion observed in colloidal glasses and liquids. *J. Phys. Condens. Matter*, 19(20):205131, 2007.

[43] J. C Crocker and D. G Grier. Methods of digital video microscopy for colloidal studies. *J. Colloid Interface Sci.*, 179(1):298–310, 1996.

Chapter 7

Summary and Outlook

7.1 Summary

This thesis address the rotational dynamics of colloidal particles in fluid crystal and glass phase. A general introduction to the rotational dynamics of colloidal particles as well as the experimental techniques used to study them experimental is provided in **Chapter 1**.

In **Chapter 2** we describe the colloidal model system which provides a particle system that exhibits the same phase behaviour as atoms and molecules albeit at length and timescales that can be directly observed on an optical microscope. A full derivation is provided for the typical length and timescales of colloidal system in terms of both rotational and translational dynamics. We also provide detail on the experimental methods used in this thesis namely the mechanism for particle synthesis and principles behind confocal microscopy.

In **Chapter 3** we optimise the 3-trimethoxysilyl propyl methacrylate (TPM) particle system for confocal microscopy by optimising several key features. First, we revisit a previous developed 'zero-flow' synthesis for TPM particles that allows more control over particle sizes than methods that utilise stirring. We then show how uniform distribution of a fluorescent dye across a batch of TPM droplets can be achieved using organic solvents. Finally we demonstrate how independent control of refractive index

and density match between particle and solvent can be achieved using a ternary solvent mixture of tetralin, trichloroethylene and tetrachloroethylene.

One of the most glaring unanswered questions about rotational dynamics in colloidal systems is whether they remain Gaussian in dense suspensions. In **Chapter 4** we address question by utilising the recently developed 'OCULI' particle, which allows for direct observation of both rotational and translational dynamics of *every* particle. Using the solvent system developed in Chapter 3 we create a sedimentation-diffusion equilibria of OCULI particles in a poorly density matched system with a short gravitational length. This results in a sediment with a rapid decay in density at the top of the sample and a dense amorphous phase at the bottom of the sample. We directly observe that both translational *and* rotational dynamics become heterogeneous in a dense suspension, but in opposite ways. Translational dynamics develop a *fast* subpopulation while rotational dynamics develop a *slow* subpopulation. This rotationally slow particles are found to exist in small but extended clusters where the degree of rotational arrest can be traced back to a compression of the coordination shell in the direction of gravity.

We next address another key question about rotational and translational dynamics in colloidal systems; the coupling between this. We investigate this in **Chapter 5** where we image two sedimentation-diffusion equilibrium of OCULI particles, one that exhibits a fluid and crystal phase and another that exists in a dense amorphous phase. First, we examine the coupling of the ensemble averaged diffusion coefficients in the dense fluid phase. We find that D_T and D_R decouple with increasing ϕ as D_T decreases by several orders of magnitude while D_R only undergoes a small decrease. We attribute this to the translational dynamics being restricted by the other particles in the population and therefore experiencing a greater increase in η while rotational dynamics are mainly governed by the η of the solvent. However, we find a correlation in both the individual rotational and translational displacements and the time averaged dynamics, at short lag times that is lost at longer lag times once the translational dynamics of the system become Gaussian. The correlation in the time averaged behaviour increases as ϕ increases from the fluid to the crystal but appears to drop in the glass phase. We suggest that the correlation in the glass changes due to the impact of interparticle friction. These observations are quantified using the correlation coefficient.

Finally in **Chapter 6** we present a synthesis which allows for control of the polydispersity of TPM particles using fractional stirring. This technique allows for

control of the polydispersity of TPM particles from 5-30% within an error or 5%. Two particles systems, developed using this technique, are demonstrated. First we demonstrate controllably polydisperse OCULI particles from which we can extract the individual particle size. Using this particle system we directly observe the translational and rotational dynamics of every particle as a function of size across the glass transition. We find that size correlations are found in both rotational and translational dynamics both in the fluid and within the glass. Furthermore we find that fast and slow particles in terms of rotational and translational dynamics display different clustering behaviour. We then demonstrate a second particle system where only the translational dynamics can be observed but again individual particle size can once again be extracted. However, this second particle system allows for creation of particles at much higher polydispersities. Using this particle system we observe that the size correlation of particle dynamics increases with increasing polydispersity across the glass transition.

7.2 Outlook

The author hopes you have taken one key message from this work: new outlook gives new insight into old problems. In the majority of this thesis we have re-examined old problems such as the rotational dynamics of dense colloidal suspensions or the coupling between translational and rotational dynamics with a new outlook due to the access to the dynamics of *every* particle. This has shone new light into these problems demonstrating the usefulness of the OCULI system as a way to visualise the rotational dynamics of every particle. However what has yet to be fully exploited is the potential of the OCULI to visualise the interparticle friction experienced by every particle [1, 2].

The OCULI system would therefore be a useful model system for study of the phenomena where interparticle friction is thought to play a key role, namely in the rheological behaviour of colloidal suspensions. Consider a colloidal suspension subject to an increasing shear rate, γ, Initially the measured viscosity is directly proportional to γ. However, as γ increases the viscosity increases rapidly and the proportional relationship is lost [3]. This behaviour is known as shear thickening and thought to be the results of interparticle friction between colloidal particles [4]. Combining the OCULI particle system, which allows direct visualisation of interparticle friction at the single-particle level, and rheo-confocal which allows for simultaneous shearing and 3D imaging of a system [5–7], would allows new insight into this phenomena. This would create a system that allows measurement of the macroscopic rheological behaviour with

simultaneous access to the dynamics at the single-particle level. This would not only allow the confirmation of the role of interparticle friction in shear thickening by also the direct observation of how these frictional contacts appear, as extended networks or smaller clusters.

Furthermore particle shapes that allow for more contact points between particles have been shown to shear thicken at lower volume fraction [8]. This suggests that control of particle shape yields control over the bulk rheological properties of a material. The easiest way to alter particle contacts in the simplest colloidal suspension, spheres, is by changing polydispersity. Polydispersity is rarely examined in colloidal suspensions due to the difficulty of creating, controllably polydisperse suspensions. So most experimental studies to date rely on binary or multimodal suspensions created by mixing multiple mono-disperse populations [9–12]. In **Chapter 6** we demonstrated a powerful synthesis that allows creation of a single truly polydisperse population of OCULI particles of controlled polydispersity from 5 to 10% from which the individual particle size can be extracted. Control of polydispersity could therefore yield control of the bulk rheological properties, yet with the OCULI system we would retain resolution of the behaviour at the single-particle level to directly observe the reason for any change. Many other synthesis techniques to alter particle shape can be applied to the OCULI particle while still having access to the rotational dynamics and therefore the degree of friction at the single-particle level [13, 14]. Lock and key colloids [14], particles of complementary shape, have garnered much experimental interest at the single-particle level but the macroscopic properties have yet to be explored. By creating OCULI particles of complementary shape and using synthesis techniques to control the degree of interlocking, we can aim to tune the onset of shear thickening as well as the recovery behaviour to create colloidal suspensions of custom mechanical properties.

Beyond the rheological phenomena the OCULI particle system could be used to shed light onto the role of interparticle friction in one of the biggest subjects of interest for the soft matter community: the glass transition. In a pioneering study in microgravity colloidal particles of $\phi > 0.60$ are shown to crystallise instead of forming a glass [15]. The crystals formed at high ϕ remain intact when brought back to earth but do not reform if the crystal is melted under shear. This has long been attributed to the mechanical load on the particles while on earth trapping them in the glass phase, once in microgravity this barrier is removed and the crystal is formed. However, we have shown in **Chapter 4** that the degree of rotational arrest and thus the amount of friction

experienced by a particle can be correlated to a compression in the direction of gravity of the coordination shell. This suggests that the mechanical load on a sample increases the amount of friction the particles experience and it may be this that traps the particles in the glass. However, finding a way to put this particle system in microgravity, or an environment that mimics it, may prove an experimental challenge.

To return to the opening line of this work, rotational dynamics have been shown to tell a much more complex story than previous experiments have suggested. Yet perhaps not quite as complex as trying to explain Northern Ireland.

7.3 Bibliography

[1] T. Yanagishima, Y. Liu, H. Tanaka, and R. P. A. Dullens. Particle-level visualization of hydrodynamic and frictional couplings in dense suspensions of spherical colloids. *Phys. Rev. X*, 11:021056, 2021.

[2] B. van der Meer, T. Yanagishima, and R. P. A. Dullens. Attraction-enhanced emergence of friction in colloidal matter. *Phys. Rev. Lett.*, 134(7):078202, 2025.

[3] A. Fernandez-Nieves and A. M. Puertas. *Fluids, Colloids and Soft Materials: An Introduction to Soft Matter Physics*. John Wiley & Sons, 2016.

[4] J. R. Royer, D. L. Blair, and S. D. Hudson. Rheological signature of frictional interactions in shear thickening suspensions. *Phys. Rev. Lett.*, 116:188301, 2016.

[5] P. Ballesta, N. Koumakis, R. Besseling, W. C. K. Poon, and G. Petekidis. Slip of gels in colloid–polymer mixtures under shear. *Soft Matter*, 9(12):3237–3245, 2013.

[6] M. Das and G. Petekidis. Shear induced tuning and memory effects in colloidal gels of rods and spheres. *J. Chem. Phys.*, 157(23):234902, 2022.

[7] Y. L. Wu, D. Derks, A. van Blaaderen, and A. Imhof. Melting and crystallization of colloidal hard-sphere suspensions under shear. *Proc. Natl. Acad. Sci. U.S.A.*, 106(26):10564–10569, 2009.

[8] M. Mahmoudian, F. Goharpey, M. Behzadnasab, and Z. Daneshfar. Shear thickening and hysteresis in dense suspensions: The effect of particle shape. *J. Rheol.*, 68(3):479–490, 2024.

[9] T. Narumi, S. V. Franklin, K. W. Desmond, M. Tokuyama, and E. R. Weeks. Spatial and temporal dynamical heterogeneities approaching the binary colloidal glass transition. *Soft Matter*, 7(4):1472–1482, 2011.

[10] T. Sentjabrskaja, E. Babaliari, J. Hendricks, M. Laurati, G. Petekidis, and S. U. Egelhaaf. Yielding of binary colloidal glasses. *Soft Matter*, 9(17):4524–4533, 2013.

[11] S. R. Williams and W. van Megen. Motions in binary mixtures of hard colloidal

spheres: Melting of the glass. *Phys. Rev. E*, 64(4):041502, 2001.

[12] Ri. Kurita and E. R. Weeks. Glass transition of two-dimensional binary soft-disk mixtures with large size ratios. *Phys. Rev. E*, 82:041402, 2010.

[13] M. Kamp, S. Sacanna, and R. P. A. Dullens. Spearheading a new era in complex colloid synthesis with tpm and other silanes. *Nat. Rev. Chem.*, 8(6):433–453, 2024.

[14] S. Sacanna, W. T. M. Irvine, P. M. Chaikin, and D. J. Pine. Lock and key colloids. *Nature*, 464(7288):575–578, 2010.

[15] J. Zhu, M. Li, R. Rogers, W. Meyer, W. B. Russel, and P. M. Chaikin. Crystallization of hard-sphere colloids in microgravity. *Nature*, 387:883, 1997.

Samenvatting

In dit proefschrift bestuderen we de rotatie dynamica van colloïdale deeltjes, die zich in een colloïdale vloeistof, vaste stof of glas bevinden. We doen dit door gebruik te maken van zogenaamde 'OCULI' – 'Off-Centre Under Laser Illumination' deeltjes. Deze deeltjes bestaan uit een klein, fluorescent deeltje (het 'oog') dat off-centre is ingebouwd in een groter deeltje (het 'lichaam') dat weer gelabeled is met een andere fluorescente kleurstof. Van deze deeltjes kunnen we zowel de positie als de orientatie bepalen, waardoor we dus de translatie en rotatie dynamica van elk individueel deeltje kunnen bepalen.

Hoofdstuk 1 geeft een algemene inleiding over colloïden, een deeltjes systeem dat hetzelfde fasegedrag vertoont als atomen en moleculen, maar waarvan de lengte- en tijdschalen zo groot zijn dat ze direct met een optische microscoop waargenomen kunnen worden. Ook introduceren we een kort overzicht van het onderzoek dat is gedaan aan rotatie dynamica van colloïden met behulp van microscopie en formuleren we het doel van het onderzoek dat beschreven is in dit proefschrift.

In **Hoofdstuk 2** beschrijven we de eigenschappen van colloïdale systemen, die ervoor zorgen dat het goede model systemen zijn voor het fasegedrag van atomaire en moleculaire systemen. Vervolgens beschrijven we de typische tijdschalen van translatie en rotatie dynamica van colloïdale deeltjes, alsook hun interacties en fasegedrag. Ten slotte introduceren we ook de experimentele technieken die gebruikt zijn in de proefschrift zoals colloïd-synthese, confocale microscopie en beeld analyse technieken.

In **Hoofdstuk 3** optimaliseren we de eigenschappen van colloïdale
3-trimethoxysilylpropyl methacrylaat (TPM) deeltjes voor het gebruik in confocale

microscopie. Allereerst ontwikkelen we een zogenaamde 'zero-flow' methode voor de synthese van TPM deeltjes, waarmee we een betere controle over de deeltjesgrootte hebben dan bestaande methoden (gebaseerd op roeren). Vervolgens laten we zien hoe de deeltjes op een homogene manier fluorescent gelabeld kunnen worden met behulp van organische oplosmiddelen. Ten slotte introduceren we een ternair oplosmiddel-mengsel van tetraline, trichloorethyleen en tetrachloorethyleen, waarmee we onafhankelijk zowel het verschil in brekingsindex als in de massa-dichtheid tussen het oplosmiddel en de TPM deeltjes kunnen controleren.

Een belangrijk openstaand vraagstuk over de rotatie dynamica in colloïdale systemen is of deze Gaussisch blijft als de concentratie van de colloïdale suspensie toeneemt. In **Hoofdstuk 4** beantwoorden we deze vraag door gebruik te maken van onze recent ontwikkelde 'OCULI'-deeltjes, waarmee we direct zowel de rotatie als translatie dynamica kunnen bepalen. Met behulp van het ternaire oplosmiddel uit hoofdstuk 3 creëren we een sedimentatie-diffusie evenwicht van OCULI-deeltjes, waarbij er een groot verschil is tussen de massa-dichtheid van de deeltjes en het oplosmiddel. Dit resulteert in een geconcentreerd, amorf en glasachtig sediment op de bodem en een snelle afname van de concentratie aan de bovenkant van het sediment. We zien dat zowel de translatie als rotatie dynamica heterogeen (niet Gaussisch) zijn, maar op een tegengestelde manier: bij translatie ontwikkelt zich een subpopulatie van snelle deeltjes, terwijl bij rotaties deze subpopulatie bestaat uit de langzame deeltjes. Deze langzaam roterende deeltjes vormen kleine (qua aantal deeltjes) maar uitgerekte clusters, waarbij de mate van onderdrukking van rotatie te herleiden is tot de compressie van naburige deeltjes in de richting van de zwaartekracht.

In **Hoofdstuk 5** bestuderen we vervolgens de koppeling tussen rotatie en translatie dynamica. Hiervoor creëren we twee verschillende sedimentatie-diffusie evenwichten: één met een kristal op de bodem en een vloeistof erboven, en één met een dichte, amorfe fase op de bodem en een vloeistof erboven. Eerst onderzoeken we de koppeling tussen de translatie en rotatie diffusiecoëfficiënten waarbij ze gemiddeld zijn over het hele ensemble van deeltjes. We zien dat ze ontkoppelen naarmate de deeltjes concentratie hoger wordt, waarbij de translatie diffusiecoëfficiënt met enkele ordes van grootte afneemt terwijl de rotatie diffusiecoëfficiënt nauwelijks afneemt. Dit kan verklaard worden doordat de translatie dynamica van deeltjes sterk wordt beperkt door de aanwezigheid van omringende deeltjes, waardoor effectief de viscositeit sterk toeneemt, terwijl de rotatie dynamica vooral bepaald wordt door de viscositeit van het oplosmiddel. Als

we echter de correlatie tussen translatie en rotatie dynamica voor individuele deeltjes bekijken, vinden we wel degelijk een koppeling op korte tijdschalen in zowel het kristal als de glasachtige fase, waarbij de correlatie in de glasfase beïnvloed wordt door frictie tussen de deeltjes. De correlatie verdwijnt op langere tijdschalen wanneer de translatie dynamica weer Gaussisch wordt.

In **Hoofdstuk 6** beschrijven we ten slotte de ontwikkeling van een methode om colloïdale TPM deeltjes te maken waarvan de polydispersiteit systematisch kan worden gevarieerd tussen de 5% en 30% met een foutmarge van 6% door middel van 'fractioneel roeren'. Met deze techniek hebben we twee verschillende deeltjessystemen gemaakt waarbij we de grootte van de individuele deeltjes direct uit confocale microscopie opnames kunnen bepalen. Ten eerste hebben we polydisperse (5-10%) OCULI deeltjes ontwikkeld, waarvan we dus zowel de translatie als rotatie diffusie van elk deeltje kunnen bepalen. Met dit systeem hebben we de dynamica in een glas-vormend systeem bestudeerd als een functie van de deeltjesgrootte, waarbij we vinden dat de translatie en rotatie diffusie beide zijn gecorreleerd met de deeltjes grootte, zowel in de vloeistof als in de glas fase. Ten tweede hebben we systeem van TPM deeltjes gemaakt waarvan alleen de translatie diffusie bestudeerd kan worden, maar wel bij een polydispersiteit van maximaal 19%. Met dit systeem laten we zien dat de koppeling tussen de translatie dynamica en de grootte van de deeltjes sterk toeneemt met toenemende polydispersiteit.

Research Data Management

The work presented in this thesis has been carried out in accordance with the research data management policy of the Institute of Molecules and Materials of Radboud University. All data present in this work is stored on servers maintained by CNCZ of Radboud University.

List of Publications

- R. A. Crothers, et al. (2023). **Characterization and Optimization of Fluorescent Organosilica Colloids for 3D Confocal Microscopy Prepared Under "Zero-Flow" Conditions**. Langmuir **39** , 5306

- R. A. Crothers, et al. **Direct Observation of Heterogeneous Rotational Dynamics in Dense Colloidal Suspensions** *(in preparation).*

- R. A. Crothers, et al. **On the Coupling of Translational and Rotational Dynamics in the Colloidal Fluid, Crystal and Glass** *(in preparation).*

- R. A. Crothers, et al. **Revealing the Role of Polydispersity in the Dynamics Across the Colloidal Glass Transition** *(in preparation).*

Acknowledgements

I would like to thank all those who have supported me during my PhD. First and foremost of those is Roel who has been a wonderful supervisor. I feel I can genuinely say I have enjoyed my PhD due to his expertise and enthusiasm for Soft Matter Science and have learnt a lot under his tutelage. I would also like to thank him for his patience in dealing with a PhD student who is prone to panic, his patience and kindness have really been an encouragement to keep going. I also have appreciated the support from all the members of the Dullens group, both from Oxford and those who have joined in the Netherlands. I have had the chance to work with some very talented people including Taiki and Berend, who helped me get started and put up with a lot of very stupid questions, and also Arran, who put up with my insistence that the group confocal doesn't like me. I would also like to thank Marieke for her chemical expertise and frequent walks in the parks to get my head showered. My family have also put up with a lot of stress, and talk about colloids over the years. Specifically, I would like to thank my parents for the constant encouragement to believe in myself as well as the amusing phone calls to ask me, 'Is this a colloid?'. I would also like to thank my brother and sister-in-law, Tim and Hannah, for their advice and support over the past few years as well as my niece and nephew, Eliza and Reuben, who remind me what is really important. I would also like to thank my Church for the community and support they have provided over the years as well as my old flatmates who still support me from overseas.

Curriculum Vitae

Ruth Anne Crothers was born in Northern Ireland on 26th June 1998. In 2016 she secured a place at University College, Oxford to study Chemistry where in her final year she discovered the weird and wonderful world of Soft Matter, a lecture course she thought was incredibly weird but also incredibly fun. In her final year she carried out the Part II project with the Krishnan group entitiled 'Studying the Role of Molecular Water in Interparticle Interactions in Solution'. She graduated with a 1st Class Honours in 2020 and continued her education with a DPhil under the supervision of Prof. Roel. P. A. Dullens. Unbeknownst to her this DPhil would begin in the UK but finish in the Netherlands after packing up, moving and rebuilding a lab. The work presented in this thesis are the results of her research from both institutions, although she claims the set up and structure of the Chemistry lab of the Department of Physics and Chemistry of Soft Matter as an additional achievement.

Figure 7.1: Supervised by the health and safety officer for our department

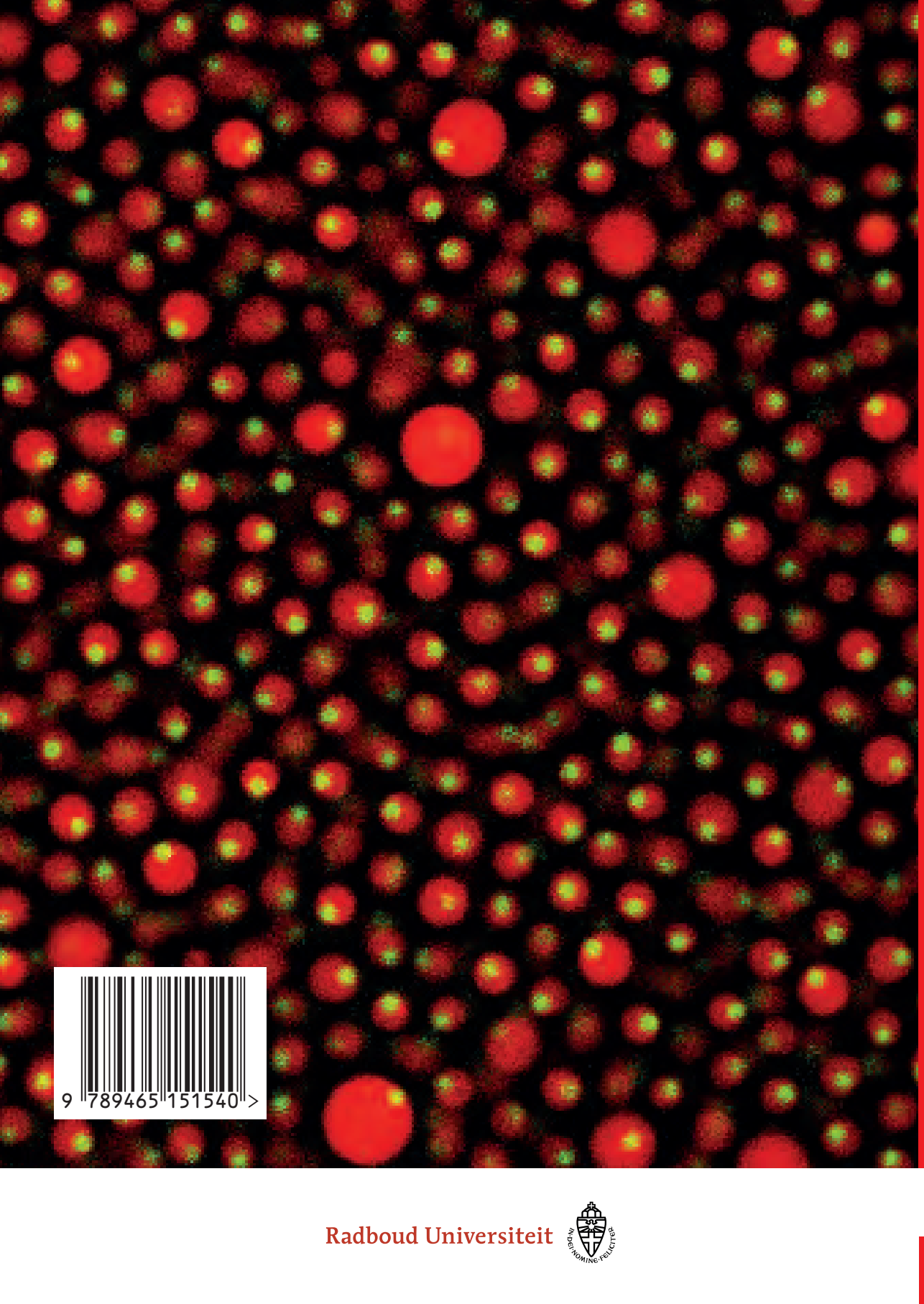

9 789465 151540

Radboud Universiteit

IN DEI NOMINE FELICITER